Fakultät für Mathematik, Informatik und Naturwissenschaften | RWTH AACHEN UNIVERSITY

Metal-Organic Vapor Phase Epitaxy and Characterization of Phase-Change Alloys in the Ge-Sb-Te Material System

Von der Fakultät für Mathematik, Informatik und Naturwissenschaften der RWTH Aachen University zur Erlangung des akademischen Grades eines Doktors der Naturwissenschaften genehmigte Dissertation

vorgelegt von

Albert Ratajczak, M.Sc.Eng.

aus

Leszno, Polen

Berichter*:* *Prof. Dr. Detlev Grützmacher*

Prof. Dr. Markus Morgenstern

Prof. Dr. Matthias Wuttig

Tag der mündlichen Prüfung*:* *2020-05-25*

Metal-Organic Vapor Phase Epitaxy and Characterization of Phase-Change Alloys in the Ge-Sb-Te Material System

Von der Fakultät für Mathematik, Informatik und Naturwissenschaften der RWTH Aachen University zur Erlangung des akademischen Grades eines Doktors der Naturwissenschaften genehmigte Dissertation

vorgelegt von

Albert Ratajczak, M.Sc.Eng.

aus Leszno, Polen

Berichter: Prof. Dr. Detlev Grützmacher

Prof. Dr. Markus Morgenstern

Prof. Dr. Matthias Wuttig

Tag der mündlichen Prüfung: 2020-05-25

Diese Dissertation ist auf den Internetseiten der Universitätsbibliothek verfügbar.

To my lovely Sanja,
for her smile and support.

Declaration of originality

I hereby declare that I have created this work completely on my own. Any part of this thesis has not previously been submitted for a degree or any other qualification, except it has been clearly stated.

I certify that this thesis has entirely been written by me. I have acknowledged all major sources of assistance, any help that I have received in my research work and in the preparation of this thesis. Where I have quoted from the work of others or myself, I have marked citations accordingly.

Jülich, June 2, 2020

Abstract

This thesis focuses on the metal-organic vapor phase epitaxy (MOVPE) of phase-change materials (PCMs) based on the Ge-Sb-Te (GST) material system, and their structural, compositional, and electrical characterization with advanced experimental methods. The materials are considered as promising candidates for the next generation of phase-change random-access memory (PRAM). In their stable hexagonal phase, GST alloys exhibit a number of structural similarities to so-called interfacial phase-change memory (iPCM) – $GeTe/Sb_2Te_3$ superlattice characterized by unique field-induced switching. Therefore, it is believed that also GST alloys could possess such unique switching properties.

The optimized deposition conditions for layers of hexagonal $Ge_1Sb_2Te_4$ on Si(111) substrate are established. The growth proceeds in the kinetic-controlled regime. The composition of the material exhibits sensitivity to the growth temperature. The value of the total gas flow (TGF) in the reactor during epitaxy strongly affects the deposited layer morphology and crystallinity. A suppression of one rotational twin domain is observed with an increase of the TGF value in the reactor during deposition. A numerical model is proposed and employed to explain the observed effect.

The growth of the materials was also explored with respect to the deposition of iPCM superlattices via MOVPE. Sb_2Te_3 layers on the Si(111) substrate were deposited. The VI/V precursors partial pressure ratio of 6 is found to be optimal for the epitaxy of Sb_2Te_3 layers. Other growth parameters do not differ from those applied for the deposition of $Ge_1Sb_2Te_4$. The suppression of rotational twin domain is observed in the Sb_2Te_3 samples too.

Experiments on deposition the of GeTe reveal the preference of the material towards three-dimensional islands growth. Moreover, the growth of GeTe crystals requires an overpressure of the Te precursor compared to the Ge precursor. Low VI/IV ratio leads to deposition of a Te-doped Ge layer with a root mean square (RMS) roughness below 4 nm. The grown Ge layer is fully relaxed with an incorporation of Te in the material at the level of 3-8‰. MOVPE of GeTe layers, however, remains a challenge.

The experimental results of this thesis give essential information on the MOVPE growth kinetics of the alloys from the GST material system. The findings are relevant for the future developments of PRAMs and understanding of the physics behind the iPCM switching. The optimized growth conditions set a solid base for further research in the field.

Kurzfassung

Diese Arbeit befasst sich mit der metallorganische Gasfphasenepitaxie (MOVPE) von Phasenwechselmaterialien (PCMs) des Ge-Sb-Te (GST) Materialsystems und deren strukturelle, kompositionelle und elektrische Charakterisierung mit hochmodernen experimentellen Methoden. Die Materialien gelten als vielversprechende Kandidaten für die nächste Generation von Phasenwechsel- Direktzugriffsspeichern (PRAM). In ihrer stabilen hexagonalen Phase weisen GST-Legierungen eine Reihe von strukturellen Ähnlichkeiten mit dem sogenannten Grenzflächen-Phasenwechselspeichern (iPCM) – $GeTe/Sb_2Te_3$-Übergitter auf, das sich durch eine einzigartige feldinduzierte Schaltung auszeichnet. Daher wird angenommen, dass auch GST-Legierungen diese einzigartigen Schalteigenschaften aufweisen könnten.

Die optimierten Abscheidungsbedingungen für Schichten aus hexagonalem $Ge_1Sb_2Te_4$ auf Si(111)-Substrat sind wohlbekannt. Das Wachstum verläuft im kinetisch kontrollierten Bereich. Die Zusammensetzung des Materials weist eine Empfindlichkeit gegenüber der Wachstumstemperatur auf. Der Wert des Gesamtflusses des Gase (TGF) im Reaktor während der Epitaxie beeinflusst die Morphologie und Kristallinität der abgeschiedenen Schicht. Die Unterdrückung einer Rotationsdomäne wird bei einer Erhöhung des TGF-Wertes im Reaktor während der Deposition beobachtet. Diesbezüglich werde ein numerisches Modell entwickelt und verwendet, um den beobachteten Effekt zu erklären.

Das Wachstum der Materialien wurde auch in Richtung der Abscheidung von iPCM-Übergittern durch das MOVPE-Verfahren untersucht. Hierfür wurden Sb_2Te_3-Schichten auf dem Si(111)-Substrat abgeschieden. Das Partialdruckverhältnis der VI/V-Vorläufer von 6 erweist sich als optimal für die Epitaxie von Sb_2Te_3-Schichten. Andere Wachstumsparameter unterscheiden sich nicht von denen, die für die Abscheidung von $Ge_1Sb_2Te_4$ verwendet werden. Die Ausbildung von der rotationssymmetrischen Doppeldomäne wird auch in den Sb_2Te_3-Proben unterdrückt.

Experimente zur Deposition von GeTe zeigen die Präferenz des Materials in dreidimensionaler Inseln zu wachsen. Darüber hinaus erfordert das Wachstum von GeTe-Kristallen einen Überdruck des Te-Prekursors im Vergleich zum Ge-Prekursors. Ein niedriges VI/IV-Verhältnis führt zur Abscheidung einer Te-dotierten Ge-Schicht, eine glatte Oberfläche mit einem durchschnittlichen RMS-Wert unter 4 nm aufwachsen ist. Die gewachsene Ge-Schicht ist völlig relaxiert und beinhaltet einen Te-Anteil von 3-8‰. Das MOVPE-

Wachstum von GeTe-Schichten stellt sich weiterhin als schwierig dar.

Die zusammengestellten Ergebnisse geben wesentliche Informationen über die MOVPE-Wachstumskinetik der Legierungen aus dem GST-Material-System. Das gewonnene Wissen ist relevant für die zukünftige Entwicklung von PRAMs und das Verständnis der Physik der Schaltvorgänge der iPCMs. Optimierte Wachstumsbedingungen bilden eine solide Grundlage für die weitere Forschung in diesem Gebiet.

Contents

List of Abbreviations

AFM	atomic force microscopy
ALD	atomic layer deposition
APT	atome probe tomography
BD	Blu-ray disk
CD	compact disk
CMOS	complementary metal–oxide–semiconductor
DVD	digital versatile disk
DETe	diethyltelluride
DI	deionized
EDX	energy dispersive X-ray spectroscopy
FWHM	full width at half maximum
GST	Ge-Sb-Te
HAADF	high-angle annular dark-field
iPCM	interfacial phase-change memory
MBE	molecular beam epitaxy
MFC	mass flow controller
MO	metal-organic
MOVPE	metal-organic vapor phase epitaxy
PC	pressure controller
PCM	phase-change material
PRAM	phase-change random-access memory

RAM	random-access memory
RBS	Rutherford backscattering spectrometry
RMS	root mean square
RSM	reciprocal space map
SEM	scanning electron microscopy
SIMS	secondary-ion mass spectrometry
STEM	scanning transmission electron microscopy
TESb	triethylantimony
TGF	total gas flow
TMIn	trimethylindium
vdW	van der Waals
XRD	X-ray diffraction

List of Figures

List of Tables

Chapter 1

Introduction

1.1 Motivation and aim of the thesis

From the very beginning of the human species existence, people tend to store and share information. The ways of storing knowledge and information were evolving with the time and reflecting the advance in technology development – starting from primitive painting in caves, hieroglyphs in Egypt, later development of writing and alphabets, the invention of printing, and finally design and development of computer technologies. We live in the age when thanks to the access to the Internet and advanced technologies, the amount of data created per unit time is higher than ever before. The number of data bytes generated every day is estimated at the level of 10^{18}, including text, photos, videos, etc. (state for 2018) [1]. This rate is not expected to slow down, but rather accelerate! We are facing a challenge, how to store this amount of information in an energetically efficient, safe, and spatially compact way.

In the last century, one of the most successful technologies applied for data storage were optical disks, such as compact disks (CDs) and digital versatile disks (DVDs) [2]. Optical disk technology utilizes the contrast in the optical properties of amorphous and crystalline state of a phase-change material (PCM) to save and read an information. The Ge-Sb-Te (GST) ternary alloys are a relevant group of the PCM materials. Except of the change in the optical characteristics upon phase transition, the resistivity of the GST compounds in the amorphous and crystalline state also varies. Therefore, the GST alloys from the pseudo-binary GeTe-Sb_2Te_3 line are considered as a promising candidate for the next generation of non-volatile random-access memory (RAM).

Lately, an energy-efficient phase switching has been observed in GeTe/Sb_2Te_3 superlattices – so-called interfacial phase-change memory (iPCM) [3]. It is believed, that the phase transition in iPCMs does not involve melting-crystallization process and is rather field-induced. Also, deposition of GST compounds in the stable hexagonal phase by means of metal-organic vapor phase epitaxy (MOVPE) has been reported recently [4, 5]. Except being the same material system, hexagonal GST and iPCMs exhibit numbers of struc-

tural similarities. It is expected that hexagonal GST could also be characterized by the field-induced switching. Due to possibility of growth via MOVPE and similarities to the iPCM superlattice, hexagonal GST is an attractive material for technological applications and fundamental research aiming to understand and explain unknown physics behind the field-induced switching.

This thesis focuses on the optimization of MOVPE growth conditions for GST alloys towards the repeatable and controllable deposition of a fully coalesced and uniform thin films of material on the Si(111) substrate. Grown samples are characterized extensively with respect to the growth conditions. The task of the successful growth optimization is challenging, since the GST material system and the chemical precursors utilized for epitaxy are very sensitive to the conditions in the reactor during deposition. Also, the growth parameters for Sb_2Te_3 and GeTe are searched in the purpose of preparation for research on a possibility for deposition of an iPCM structure by MOVPE.

1.2 Outline of the thesis

The thesis is divided into three bigger chapters entitled *Phase-change materials*, *Methods*, and *Results and discussion*. The chapters consist of sections focused on a specific problem. Below, detailed scope of the thesis is given:

Chapter 2, *Phase-change materials*, gives a detailed overview on the state of the art for PCMs. From unique properties of the GST alloys, through phase switching, memory cell operation and applications, to mysterious transition in the iPCM structures – the knowledge reported in the literature is reviewed.

Chapter 3, *Methods*, describes experimental methods used in this work and the basics of their working principles. It is split into two sections:

1. *Metal-organic vapor phase epitaxy* – explains the basics of MOVPE, including the Grove model and influence of various parameters on the growth. Also, it introduces MOVPE 1119 – the system used for this work, and discusses possible reactions in the reactor with respect to utilized precursors.
2. *Characterization methods* – gives an overview of the characterization methods involved in the examination of deposited samples.

Chapter 4, *Results and discussion*, presents experimental results obtained in the frame of the work done for this thesis. The chapter is composed of the following sections:

1. *Growth of Ge-Sb-Te alloys* – the influence of the conditions in the reactor on deposition of GST is discussed here with respect to Si substrate pre-annealing atmosphere, value of total gas flow (TGF) in the reactor, and growth temperature. The optimized growth parameters for the deposition of fully coalesced $Ge_1Sb_2Te_4$ layers are reported.

2. *Modeling of Ge-Sb-Te twin domains* – this section focuses on numerical calculations which explain observed in chalcogenides suppression of one rotational twin domain with a reduction of the growth rate. The explanation for the difference found between films grown via MOVPE and molecular beam epitaxy (MBE) is also proposed.
3. *Growth of Sb_2Te_3* – describes optimal deposition conditions for uniform and coalesced Sb_2Te_3 layers. The growth is optimized with respect to VI/V partial pressure ratio, substrate temperature and pretreatment.
4. *Growth of GeTe and Ge* – discusses the challenge of GeTe deposition and presents highly crystalline Te-doped Ge layers. The influence of Sb, growth temperature, TGF value, and VI/VI partial pressure ratio on the epitaxy of GeTe is reported.
5. *Electrical characterization* – displays and explains electrical properties of $Ge_1Sb_2Te_4$ and Sb_2Te_3 layers measured with the Hall effect in the temperature range of 10-300 K. Also, the room temperature characteristics of Te-doped Ge are presented.

Chapter 5, *Conclusion and outlook*, is the final chapter summarizing the whole thesis and underlining the takeaways. In the end, selected preliminary results of the further work are presented, and the author's perspective for the future of MOVPE-grown GST is shared.

Chapter 2

Phase-change materials

PCMs are characterized by unique properties, which make them suitable for applications in data storage devices. A material has to meet few requirements, to be considered as a proper candidate for a phase-change memory. First, and the most essential, it has to be capable to reversible switch between amorphous and crystalline state, with measurable contrast between these two states in optical, if applicable for rewritable optical storage, or electrical properties, if applicable for non-volatile electronic storage. Second, the transition from the amorphous to the crystalline phase, and backward, should be quick, in nanoseconds range, and possible to induce with a short laser or voltage pulse. Third, to make a good memory, the material needs to exhibit long-term thermal stability in the amorphous state. The device should be able to store information for a period of at least over a dozen of years, or even several decades, at room temperature. Moreover, it should also show chemical stability on environmental conditions, e.g., resistance on water. Finally, the memory should be rewritable, so used material has to preserve its chemical composition and properties over a large number of reversible switching cycles, more than 10^5 [6].

2.1 Ge-Sb-Te alloys

Ge-Sb-Te (GST) alloys exhibit the above described unique properties and form a large fraction of known PCMs. They are commonly represented in the ternary phase diagram for Ge, Sb, and Te, depicted in Fig. 2.1. In the diagram, the alloys can be divided into three groups [6, 7]. Two smaller groups are Ge-doped Sb, marked in Fig. 2.1 with blue semicircle labeled as Ge_xSb_{1-x} ($x \approx 0.15$) [8], and doped Sb_2Te, marked with green semicircle. Sb_2Te, often doped with Ag, In and Ge, was successfully applied for rewritable optical storage disks [9–11]. Third, bigger group, is a family of materials along the pseudo-binary GeTe-Sb_2Te_3 line, drawn in red in Fig. 2.1. The last class of the materials is the main object of interest in this thesis.

The GeTe-Sb_2Te_3 pseudo-binary line includes, among others, alloys with following compositions: $Ge_1Sb_4Te_7$, $Ge_1Sb_2Te_4$, $Ge_2Sb_2Te_5$, and $Ge_3Sb_2Te_6$. All of the listed materials

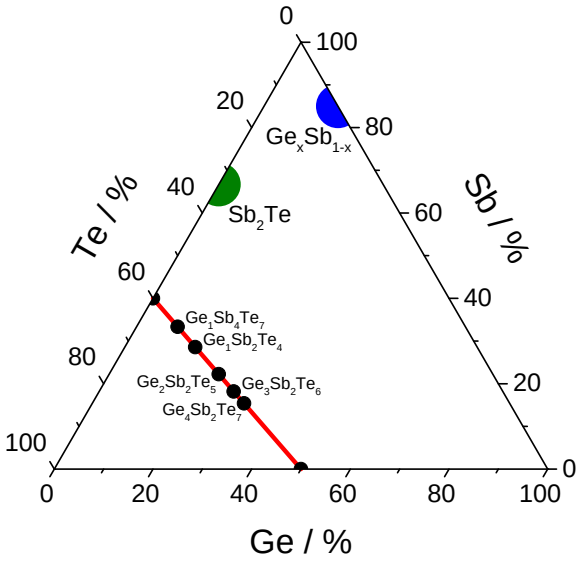

Figure 2.1: Ternary phase diagram for GST alloys. Three groups of materials can be distinguish: the GeTe–Sb_2Te_3 pseudo-binary line, doped Sb_2Te and doped Sb, marked with red, green and blue color, respectively.

can crystallize in metastable rock-salt structure with a high number of randomly located vacancies on cation lattice site, which is occupied with Ge and Sb atoms, while anion lattice site is fully occupied with Te atoms [7, 12–15]. Although the rock-salt structures of GST compounds are metastable and the materials tend to rearrange to a more stable structure upon prolongated heating, the rock-salt form often appears in crystallization process due to rapid cooling. The vacancies in metastable structures of GST alloys seem to have a crucial impact on the properties of the materials. Many of covalently bonded semiconductors (e.g., Si, GaAs, GaN) have on average four valence electrons per atom. Therefore, sp^3-hybridization is favorable and the atoms arrange in a tetrahedral configuration. However, this is not the case for GST alloys. Due to the electron configuration of Ge, Sb, and Te atoms (presented in Tab. 2.1), the GST materials crystallized in the rock-salt structure have on average more than four valence electrons per atom site, including vacancies in the count of atoms. Therefore, bonding by the *p*-electrons is more favorable and atoms prefer an octahedral arrangement [7, 16].

Table 2.1: Electron configuration of Ge, Sb, and Te atoms.

Element	Electron configuration	Valence electrons
Ge	[Ar] $3d^{10}$ $4s^2$ $4p^2$	4
Sb	[Kr] $4d^{10}$ $5s^2$ $5p^3$	5
Te	[Kr] $4d^{10}$ $5s^2$ $5p^4$	6

Table 2.2: Percentage of vacancies on cation lattice site in metastable rock-salt structure for chosen GST materials, together with the average number N_{sp} of valence electrons per atom (including vacancies in the count).

Material	**Vacancies**	$\boldsymbol{N_{sp}}$
$Ge_1Sb_4Te_7$	29%	4.71
$Ge_1Sb_2Te_4$	25%	4.75
$Ge_2Sb_2Te_5$	20%	4.80
$Ge_3Sb_2Te_6$	17%	4.83

Tab. 2.2 lists percentage of unoccupied cation lattice sites (vacancies) and the average number of valence electrons per atom (N_{sp}) in metastable rock-salt structure for some of GST materials. In all cases N_{sp} is greater than four, but at the same time smaller than five. Thus, in crystals bonded covalently by the p-electrons, the average number of electrons per bond is lower than two. It would mean that some of the bonds stay unsaturated. Hence, the concept of resonant bonding is proposed, which describes such a state of crystal as a superposition of equivalent saturated bonds [17]. It has been shown that Te-based ternary alloys tend to crystallize in rock-salt structure, if their N_{sp} is greater than 4.1 [16].

It is believed that the unique properties of GST alloys are a consequence of the material ability to form resonant bonding. A characteristic feature of the resonant bonding is delocalization of electrons, which leads to an increase of electric polarizability in the system. Subsequently, this affects the material relative permittivity ϵ_r, since the values are connected with Clausius-Mossotti relation [18]

$$\frac{\epsilon_r - 1}{\epsilon_r + 2} = \sum_i \frac{N_i \alpha_i}{3\epsilon_0} \tag{2.1}$$

where the index i refers to contributions of different types of atoms composing the material, N denotes number density, α – electric polarizability, and ϵ_0 – vacuum permittivity. Therefore, the resonant bonding model explains the change of refractive index between amorphous and rock-salt phase of GST compounds. Moreover, crystalline GST materials are characterized by lower band gap [19–24], comparing to their amorphous analogs. The transmittance of amorphous state is higher and the high-frequency limit of the dielectric constant ϵ_∞ noticeably lower than the value for the rock-salt state. The electrical properties also differ significantly, the crystalline materials are more conductive [25, 26]. All in all, GST alloys exhibit measurable contrast in optical and electrical properties of the amorphous and the crystalline rock-salt structure.

Lencer et al. [7] have classified a wide set of materials, composed of elements from group IV, V, and VI, according to the degree of ionicity and the tendency towards hybridization

(covalency). As the result, they created a map of PCMs based on the nature of the bonding in the system. As they noticed, PCMs are *found in the area of small ionicity and a limited degree of hybridization.*

GST alloys are often deposited in amorphous or rock-salt phase by sputtering or via MBE [15, 22, 27–29]. The state of deposited material depends mainly on the temperature of the substrate during the deposition process. The amorphous material can be later annealed to its metastable or stable phase, or crystallized with a laser pulse. So far, the discussion in this subsection focused on the amorphous and metastable rack-salt GST. However, in recent years, there is a growing interest in the stable hexagonal structure of GST compounds, due to its structural similarities to so-called iPCM superlattices, which exhibit energetically efficient field-induced switching [3] (the topic is discussed extensively in the next section 2.4). The main similarities between hexagonal GST alloys and the iPCM structure are: (1) alternating cation-anion layers of Ge, Sb and, Te atoms, (2) Te-Te bilayers with van der Waals (vdW) gap between them, and (3) structural anisotropy. Therefore, it is believed that GST alloys could show similar behavior and also undergo field-induced switching. The GST materials from the GeTe-Sb_2Te_3 pseudo-binary line, in their stable form, have been grown via MOVPE [4, 5]. The hexagonal crystal structure is obtained since the growth temperatures is higher than the material crystallization point in the stable structure. The deposited materials tend to grow in stable phase with intermixed Ge/Sb layers [13, 30, 31], while in sputtered or MBE-grown iPCMs the cation layers are ordered and occupied either by Ge or Sb. One should remember about this differences. The unit cells of the stable structures for selected materials along the GeTe-Sb_2Te_3 pseudo-binary line are depicted in Fig. 2.2, together with the statistical composition of Ge/Sb layers. The lattice parameters are given in Tab. 2.3.

Table 2.3: Hexagonal lattice parameters for chosen materials along the pseudo-binary GeTe-Sb_2Te_3 line [33].

Material	**Space group**	***a*** **/ Å**	***c*** **/ Å**
Sb_2Te_3	$R\bar{3}m$	4.26	30.45
$Ge_1Sb_4Te_7$	$P\bar{3}m1$	4.25	23.86
$Ge_1Sb_2Te_4$	$R\bar{3}m$	4.24	41.12
$Ge_2Sb_2Te_5$	$P\bar{3}m1$	4.22	17.23
$Ge_3Sb_2Te_6$	$R\bar{3}m$	4.21	62.24
GeTe	R3m	4.13	10.66

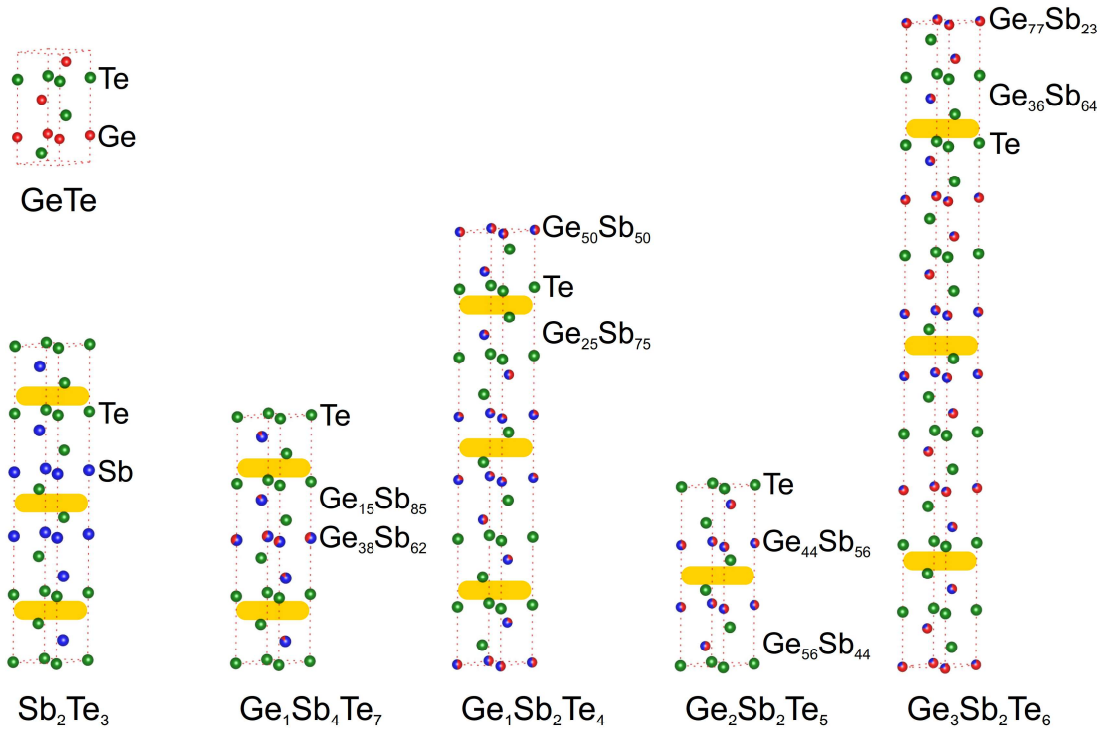

Figure 2.2: Unit cells of selected materials from the pseudo-binary GeTe-Sb_2Te_3 line, together with the statistical composition of Ge/Sb layers. Yellow marks point the placement of vdW gaps. Models from *Inorganic Crystal Structure Database* [32].

2.2 Phase switching and memory cell operation

Phase switching in PCMs occurs upon delivering an energy impulse to the system, which heats up the material above the crystallization or melting point, dependently on the direction of the transition. The phenomena was originally investigated and reported by Ovshinsky [34] in 1960s. The energy can be pass to the system in a form of a laser pulse, in case of optical disks, or as an electrical current impulse, for application in an electronic memories. The phase switching is described here in the context of electronic memory device operation, which utilizes contrast between the resistivity of a PCM amorphous and metastable rock-salt state. The description is based on this published in the paper by Wong et al. [35]. The operation principles are analogous in the case of switching with a laser pulse.

Fig. 2.3 (b) presents conventional architecture of a single phase-change memory cell – a PCM placed between the top and the bottom electrode [35, 36]. For the consideration, let us assume that the material is in the low-resistive metastable crystalline state, which will be shortly called as SET. Accordingly, the high-resistive amorphous phase will be called RESET. The SET and RESET phases are schematically shown in Fig. 2.3 (a). In order to switch to the RESET state, first the material is melted by applying a high

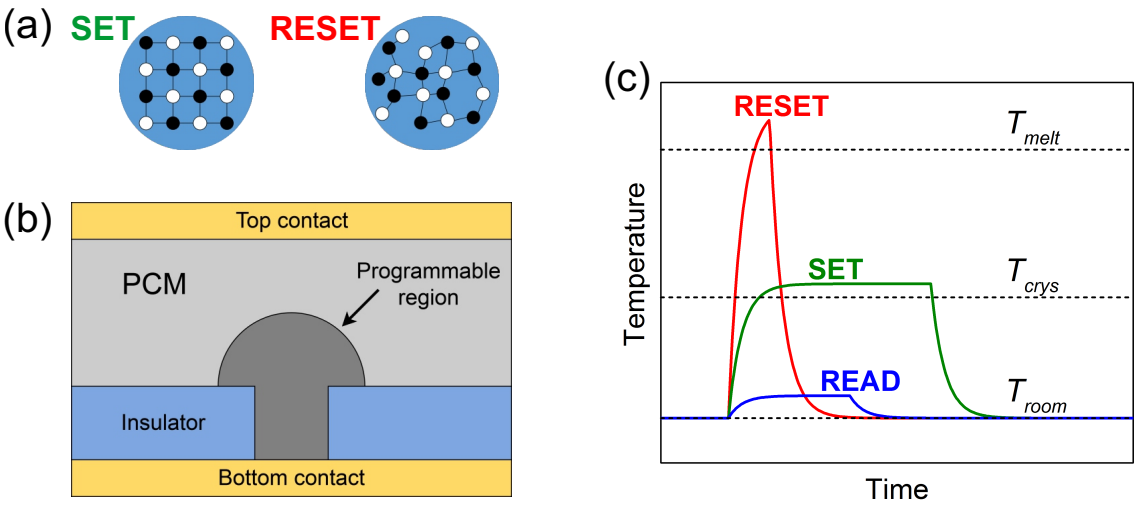

Figure 2.3: Operation principles of an electronic PCM memory cell: (a) schematic representation of crystalline SET and amorphous RESET state; (b) conventional architecture of a single memory cell; and (c) change of PCM temperature while switching to RESET or SET state and while reading the state. Horizontal dashed lines mark room temperature (T_{room}), PCM crystallization temperature (T_{crys}) and PCM melting point (T_{melt}). Based on Wong et al. [35].

electrical current impulse for a short time, and next quenched rapidly. This procedure leaves an amorphized region in the PCM between the top and the bottom electrode, which effectively influences the material resistivity. To switch the memory cell back to the SET state, the temperature of the material is raised above its crystallization temperature by applying a medium electrical current for the time sufficiently long for crystallization. The RESET and SET impulses are illustrated in Fig. 2.3 (c) as a change of the material temperature. To make an applicable device, it has to be possible to read the state of the cell without disruption of its phase. This is realized by passing through the cell a current small enough not to switch the material.

Examples of current-voltage dependences for crystalline and amorphous states of a PCM are plotted in Fig. 2.4. The transition from the high-resistive to the low-resistive state starts at the threshold switching voltage V_{th}, a negative differential resistance is observed at this region [35, 36]. Below the electronic threshold the resistance of amorphous state is too high and limits the current, so Joule heating is not able to generate enough power to crystallize the material. The effect of threshold switching lowers the resistance and allows the crystallization. For short voltage pulses the process is reversible, but for pulses longer than the crystallization time the material switches to the low-resistive state. Switching to the SET state (crystallization) is the slowest process involved in the operation of a PCM based memory, therefore it is the limiting factor for the operation speed. Typically, the SET programming time is in the range of 100-200 ns [35, 37, 38]. The energy consumption is mostly determined by the RESET programming since the switching, in this case, requires a generation of power high enough to melt the material.

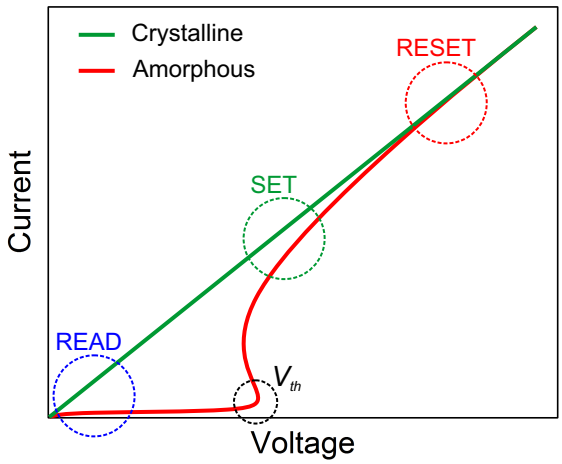

Figure 2.4: Current-voltage characteristic for a PCM. The low-resistive crystalline state shows linear dependence, while the high-resistive amorphous phase is characterized by a breakpoint at the threshold voltage V_{th}. Blue, green and red circles mark regions of the state reading, switching to the SET, and switching to the RESET, respectively. Based on [6, 35].

Conventional phase-change memories use the transition between amorphous and metastable rock-salt structure, as described above. However, as already mentioned, GST alloys can form stable hexagonal crystal structure upon annealing at a temperature above the crystallization point in the stable-phase. The transition from the metastable to the stable structure is explained as the diffusion of Ge and Sb atoms in a way that randomly distributed in the metastable crystal structure vacancies order in layers. Subsequently, the vacancies layers collapse and form a vdW gaps in the stable crystal phase [13, 39], presented in Fig. 2.2. The materials in the hexagonal phase are in general more conductive than their amorphous and metastable rock-salt equivalents, and their high-frequency dielectric constant is larger [25]. Annealed to temperatures higher than 275 °C and crystallized in the stable hexagonal phase $Ge_1Sb_2Te_4$ shows metallic behavior with $d\rho/dT > 0$, where ρ stays for resistivity, and T for temperature. Other GST materials, $Ge_1Sb_4Te_7$, $Ge_2Sb_2Te_5$, and $Ge_3Sb_2Te_6$ also show metallic character upon annealing [26]. The band gaps of the hexagonal GST compounds are rather small, with general tendency to increase while the Sb content in the alloy decreases [19, 21–23, 40].

2.3 Applications and technological relevance

Over the years now, PCMs have been successively utilized in optical storage disks technology. In optical disks, information is stored as an amorphous mark in crystalline material and read by measuring the contrast in optical properties of amorphous and crystalline phase. The information is recorded, read, and erased with a laser beam pulses. Three generations of optical disks have been developed [6]. Data recording density has been increased by shortening the wavelength of the used laser and by introducing disks with

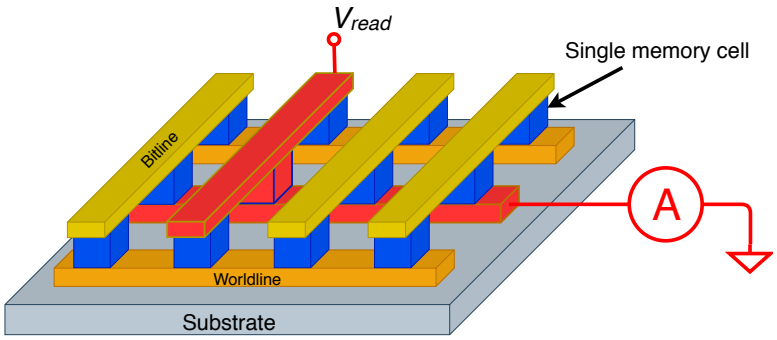

Figure 2.5: A simplified model of PRAM array. Memory cells are addressed with corresponding worldlines and bitlines. In the picture, red color schematically shows reading the state of one memory cell.

the dual-layer design. In the first-generation CDs the wavelength of 780 nm is used, the second-generation DVDs utilize lasers emitting at 650 nm, and in the third-generation Blu-ray disk (BD) the wavelength of 405 nm is involved [6, 41]. The storage density can be doubled in dual-layer design, resulting in s storage capacity of 50 GB. Shifting used radiation towards shorter wavelength with development of subsequent optical disk generation, forced to change the composition of used materials. While $Ge_2Sb_2Te_5$ is suitable for operation in red and infrared spectral range (the first and the second generation), the contrast between its optical properties of the crystalline and amorphous phase is lower in blue spectral range (the third generation). The contrast for radiation around 405 nm is pronounced in compounds with higher Ge content, e.g., $Ge_8Sb_2Te_{11}$, therefore such materials are used in BD [6].

Recently, there is a lot of interest in electronic non-volatile phase-change random-access memory (PRAM) which operation is based on phase transition and change of electrical conductivity between the crystalline and amorphous state of a material (the process described in previous subsection 2.2). PRAMs are often realized in the form of a matrix [37, 38, 42–44], depicted in Fig. 2.5. Memory cells in the matrix are addressed with so-called worldlines and bitlines. By applying the proper voltage to the lines corresponding to a cell, the state of the cell can be switched or read. The design is compatible with the complementary metal–oxide–semiconductor (CMOS) technology.

PCM memories were already introduced to the open market. In 2015, 3D XPoint memory technology was announced as a result of a collaboration between Intel and Micron Technology. The storage devices are available under brand names Optane and QuantX [45].

2.4 Interfacial phase-change memories

$GeTe/Sb_2Te_3$ superlattices, known as iPCMs, are proposed as an attractive candidate for the next generation of non-volatile RAM. Energy efficient and rapid switching of iPCMs have been reported by Simpson et al. [3]. The transition of a iPCM structure to the SET

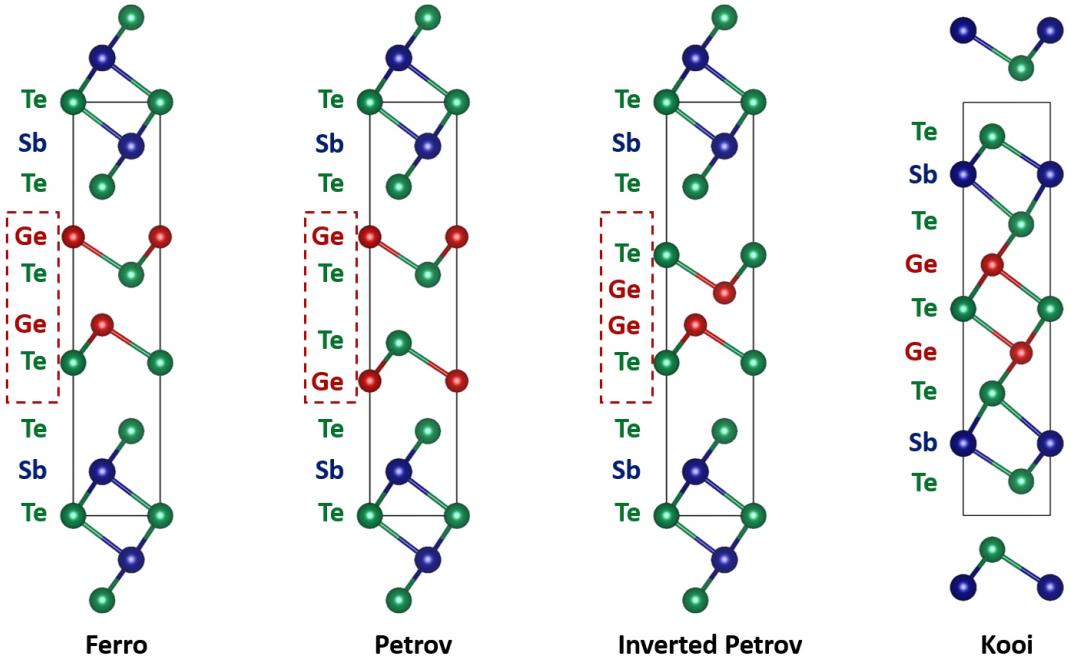

Figure 2.6: Models of iPCM superlattices considered in the literature. The first three models (Ferro, Petrov and Inverted Petrov) are distinguished by the sequence of Ge and Te atoms in GeTe layer, while the last one (Kooi) corresponds to $Ge_2Sb_2Te_5$ alloy with ordered Ge and Sb layers.

state was possible in the time of 25 ns, compared to 100 ns for GST alloy. Additionally, iPCMs showed higher endurance than conventional GST memories, $\sim 10^9$ SET-RESET cycles recorded for iPCM versus $\sim 10^6$ for GST. These enhanced properties seem to be a consequence of the unique iPCM switching mechanism. In contrast to conventional PRAM, the transition between the high- and low-resistive phase of iPCM does not involve melting/crystallization process – the structure remains crystalline in both states. It is believed that the phase change of iPCMs is field-induced, however the mechanism and physics of the field-induced switching remains the object of discussion [46–49].

Typically, $GeTe/Sb_2Te_3$ superlattices for iPCMs are sputtered [3, 47] or grown via MBE [49, 50]. Although structures with different $GeTe/Sb_2Te_3$ stacking have been produced [47, 50], iPCMs are usually modeled as $(GeTe)_2/(Sb_2Te_3)_1$ superlattice [46, 48] – two GeTe layers alternating with one Sb_2Te_3 layer. In this simple three monolayers model, the composition of the structure corresponds to $Ge_2Sb_2Te_5$ alloy, which is characterized by small unit cell (comparing to other GST alloys, see Fig. 2.2). Various arrangements of atoms in the iPCM unit cell are shown in Fig. 2.6. The main difference between the models of the iPCM superlattices presented in the picture is the sequence of Ge and Te atoms in GeTe layer. In so-called Ferro structure, two monolayers of GeTe in its ferroelectric phase are sandwiched between Sb_2Te_3 blocks, forming Te-Ge-Te-Ge sequence. Petrov structure is characterized by Ge-Te-Te-Ge sequence, and consequently Inverted Petrov by Te-Ge-Ge-Te. The last one, Kooi structure, corresponds to the hexagonal phase of $Ge_2Sb_2Te_5$

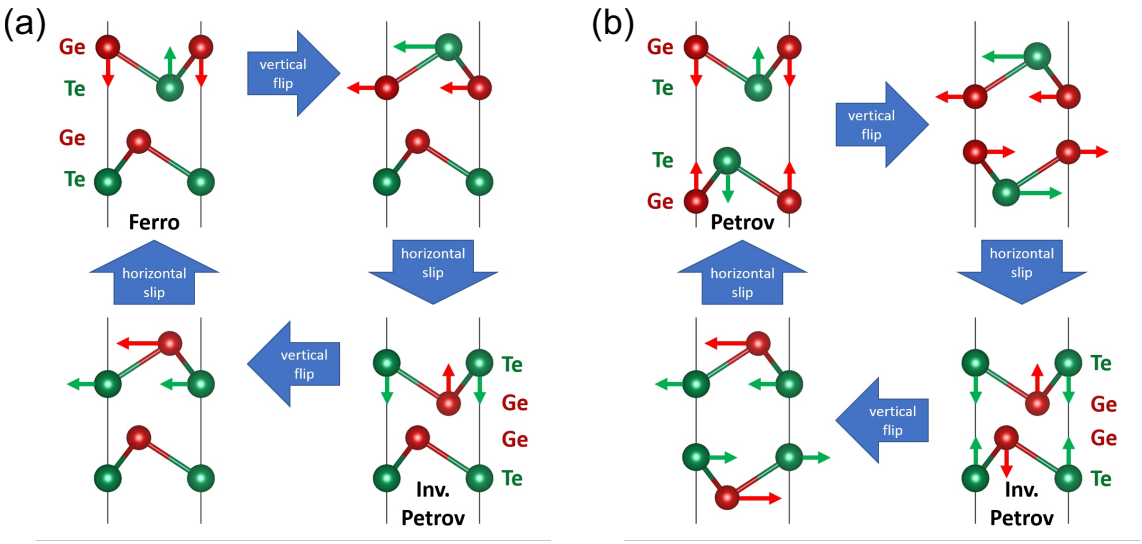

Figure 2.7: Two considered mechanism of iPCM switching: (a) transition between Ferro and Inverted Petrov structure proposed by Tominaga et al. [46]; and (b) transition between Petrov and Inverted Petrov structure proposed by Ohyanagi et al. [47].

with Ge and Sb atoms ordered in cation layers [51].

A lot of effort has been put to investigate the stability of iPCM structures and to find the switching mechanism using experiments and *ab initio* calculations. It has been found that the Kooi structure is the stable one at 0 K, but for temperatures higher than $\sim$ 150 K the Ferro phase is energetically favorable [46, 48]. The Inverted Petrov structure is a high-resistive state of iPCM, while Ferro and Petrov configurations exhibit low resistance [47, 52]. In the high-resistive structure Ge atoms are situated in tetrahedrally coordinated sites, while for both of low-resistive configurations Ge atoms occupy octahedrally coordinated sites. This is in analogy to octahedral arrangement of atoms in resonantly bonded metastable rock-salt structure of GST alloys. Therefore, the iPCM phase-switching can be described as a transition between the listed structures. It has been proposed that the switching occurs on the GeTe-Sb_2Te_3 interface and mainly involves motions of Ge atoms. Two models of the field-induced switching are essentially considered and discussed in the literature, one proposed by Tominaga et al. [46] and another one by Ohyanagi et al. [47]. Both models can describe the iPCM SET-RESET switching as two-step process consisting of a vertical flip of Ge and Te layers (umbrella flip) followed by lateral motion of GeTe blocs to energetically more stable arrangement [48].

The models are schematically depicted in Fig. 2.7. In the model of Tomianaga et al., image (a), one GeTe monolayer flips vertically and then slides in the lateral direction to ensure the transition between high-resistive Inverted Petrov and low-resistive Ferro structure [46, 48, 53]. However, Ohyanagi et al. [47] reported that the Ferro configuration is the stable ground state of iPCM superlattice. They proposed that the switching occurs between Inverted Petrov and Petrov structure. The model by Ohyanagi et al. requires vertical flip

and lateral movements of two GeTe monolayers [47, 48, 54], as shown schematically in Fig. 2.7 (b).

Recent experimental studies question the models proposed by Tominaga et al. and Ohyanagi et al. The model of iPCM superlattice consisting of thin rhombohedral GST layers sandwiched between Sb_2Te_3 blocks has been reported [49, 50]. GST layers are observed in iPCM structure, since GeTe and Sb_2Te_3 exhibit strong intermixing tendency. The switching mechanism based on the amorphous-crystalline transition of such thin GST blocks captured between crystalline Sb_2Te_3 layers is also suggested. This approach is in contradiction with previously introduced models, assuming crystalline-crystalline transition. Moreover, at the same time, it has been shown that prolongated annealing of iPCM structure at the temperature of 400 °C leads to formation of stable GST phase with mixed Ge/Sb layers [49, 50]. This observation is especially important regarding the production and applications of iPCMs in data storage devices.

Summarizing, the switching mechanism of iPCM superlattices stays an open question. It is not clear how the phase-change of iPCM structures proceeds. Experiments are inconsistent with proposed theoretical models and expected crystalline-crystalline phase transition is debated. Therefore, observed unique properties of iPCMs and the physics behind the field-induced switching remain mysterious and require further research and revision.

Chapter 3

Methods

3.1 Metal-organic vapor phase epitaxy

This thesis focuses on deposition of GST alloys via MOVPE. In this section, the basic principles of MOVPE are described and discussed in detail. In the first half, the Grove model is introduced and the influence of conditions in the reactor on the growth is described extensively. The second half focuses on the MOVPE reactor employed for the work – MOVPE 1119. Also, possible reactions in the system are discussed with respect to used precursors.

3.1.1 Basics of MOVPE

MOVPE, also known as organometallic vapor phase epitaxy (OMVPE) or metal-organic chemical vapor deposition (MOCVD), is a chemical deposition method widely used in the industry. The method utilizes metal-organic (MO) precursors for deposition of crystalline materials, as the name suggests. Generally speaking, MO compound is a chemical compound containing a direct bond between a metal and a carbon atom of an organic molecule. However, in MOVPE technology also other chemicals are used, such as metal-alkoxides, metal-alkylamides or metal-hydrides [55]. A MOVPE process is schematically illustrated in Fig. 3.1. The growth of a materials proceeds by chemical reactions of the precursors at high temperature, in non-equilibrium thermodynamic conditions. The process is influenced by partial pressure of the precursors and their decomposition (reaction) rate. The rate depends on the growth temperature and the precursors residence time in the reactor. The residence time changes with the gas velocity, which is proportional to the TGF value. The gas velocity also influences the thickness of the boundary layer at the substrate/gas-phase interface. The boundary layer affects the diffusion of reactants towards the sample surface. Further, one has to remember about the effect of the total pressure in the reactor and parasitic deposition of materials on the reactor walls. The last can cause memory effects, e.g., catalytic reactions, or warming effect by reducing the glass transparency and back-reflection of the heater radiation. The overall deposition process via MOVPE is com-

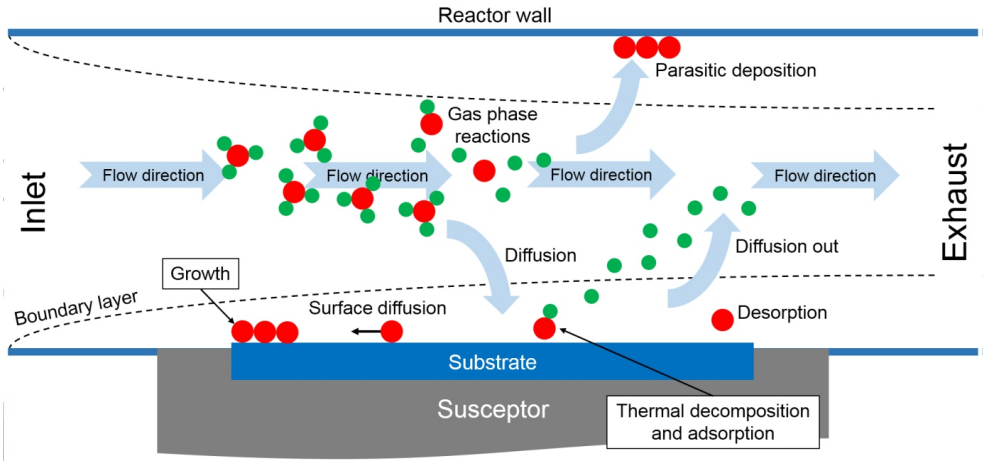

Figure 3.1: Schematic illustration of processes in MOVPE reactor.

plex, and chemical reactions in the reactor are hard to describe. Therefore, it is difficult to model and predict the result of an experiment. Below, the basic concepts of MOVPE are introduced and the effects of various parameters on the growth process are discussed.

Grove model

The Grove model is a simple model initially developed to describe thermal oxidation of silicon [56]. The concept was successively adopted for description of epitaxy via chemical vapor deposition methods [57, 58]. Fig. 3.2 presents the main concept of the Grove model. The number concentration of a reactant in the gas phase equals C_g and changes on the surface of the substrate to C_s. The flux of the reactant towards the surface can then be described as

$$F_1 = h_g(C_g - C_s), \tag{3.1}$$

where h_g is the gas-phase mass transfer coefficient. The flux of the reactant contributing to the epitaxial growth depends on the surface reaction rate constant k_s[1]. Assuming the first order reaction, F_2 can be expressed as

$$F_2 = k_s C_s. \tag{3.2}$$

If the system is in steady state, then $F_1 = F_2 = F$ and

$$C_s = \frac{h_g C_g}{h_g + k_s}. \tag{3.3}$$

The flux is defined as the number of atoms flowing through the unit area in a given time. Therefore, dividing the flux by the number of the atoms incorporated in the unit volume of deposited layer, the growth rate of the epitaxial film can be calculated. Substituting

[1]Note that k_s is a surface reaction rate constant with the unit of $\mathrm{m{\cdot}s^{-1}}$.

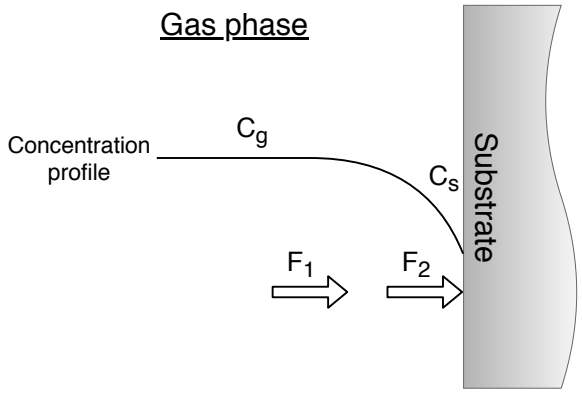

Figure 3.2: Schematic representation of the Grove model.

the Eq. 3.3 into the Eq. 3.2, one gets the expression for the growth rate

$$r = \frac{F}{N} = \frac{h_g k_s}{h_g + k_s} \cdot \frac{C_g}{N}, \tag{3.4}$$

where N is the number of the atoms in the unit volume of deposited material. The number concentration of the reactant in gas-phase is $C_g = y_i C$, where y_i is the reactant mole fraction and C is the total number of molecules per unit volume in the gas phase. The final equation for the growth rate can be written as

$$r = \frac{h_g k_s}{h_g + k_s} \cdot \frac{C}{N}\, y_i. \tag{3.5}$$

The Grove model leaves out the flux of the reaction products, which do not take part in the layer deposition, and assumes the first order reaction. Nevertheless, it can still describe MOVPE growth process and explain the two growth regimes.

Growth temperature

The logarithmic growth rate dependence on reciprocal deposition temperature is plotted in Fig. 3.3. The dependence is well known for MOVPE process and has been often reported in the literature [55, 58–62]. Also, the three main growth regimes are marked in the picture: kinetic-controlled (surface reaction), diffusion-controlled (mass transfer) and desorption/pre-reactions-limited regime. The discussed Grove model explains the first two of three listed regimes. The smaller of the values h_g and k_s limits the growth rate. At low temperatures, the reaction proceeds slower than diffusion and the growth is limited by the reaction kinetics. In the kinetic-controlled regime, the growth rate is given by the equation

$$r \approx k_s \frac{C}{N}\, y_i. \tag{3.6}$$

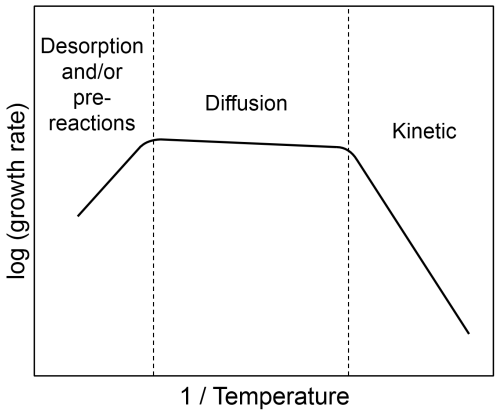

Figure 3.3: The temperature dependence of a growth rate in MOVPE process. The three main growth regimes are distinguished.

In this range, the growth rate is proportional to the surface reaction rate constant. The temperature dependence of a reaction rate constant is described by the Arrhenius equation

$$k_s = A \cdot \exp\left(-\frac{E_a}{RT}\right), \tag{3.7}$$

where A is the pre-exponential factor, E_a – the reaction activation energy, R – the gas constant, and T – the temperature. Since the rate constant depends exponentially on the temperature, also the growth rate shows the exponential dependence on the deposition temperature. Hence, the plot in Fig. 3.3 is linear in the kinetic-controlled regime.

At some temperature, the reaction rate reaches such a high value that the diffusion process is slower than proceeding reactions and the mass transfer coefficient starts to limit the growth rate. This is so called diffusion-limited regime. Then, the Eq. 3.5 can be approximated with

$$r \approx h_g \frac{C}{N} y_i, \tag{3.8}$$

In the diffusion-limited regime, the growth rate changes negligibly with the temperature and is nearly constant, therefore it is the perfect range for epitaxial growth of materials. However, the gas-phase reactions can modify the reactants delivered to the surface and influence the growth rate by changing the surface reaction rate constant k_s.

At very high temperatures the growth rate drops down again. This is due to the fact that the gas-phase pre-reactions and/or the desorption of materials from the substrate start to dominate in the reactor. Therefore, the diffusion of the reactants towards the substrate surface decreases, while the diffusion outwards increases. Consequently, this suppresses the deposition of the material. The Grove model fails at describing the high-temperature growth regime because of its simplicity. As already mentioned before, the model neglects the flux of the particles diffusing out from the surface. It also does not consider the possible pre-reactions in the gas-phase. From now on, further discussion in this chapter will focus on the kinetic- and diffusion-controlled deposition.

Total gas flow

The deposition temperature states the growth regimes for MOVPE. Nevertheless, the growth rate is still influenced by other parameters and conditions in the reactor. The mass transfer coefficient can be expressed as

$$h_g = \frac{D_g}{\bar{\delta}}, \tag{3.9}$$

where $\bar{\delta}$ is the average thickness of the boundary layer and D_g is the diffusivity. Since the growth rate in the diffusion-controlled regime (Eq. 3.8) is proportional to the mass transfer coefficient, it is clearly inversely proportional to the boundary layer thickness. The boundary layer thickness is often defined as the distance from the surface to the point over it where the gas velocity is equal to 99% of the free stream gas velocity, $u = 0.99u_g$. Considering the MOVPE susceptor and a wafer on it as a flat plate, and a laminar flow in the reactor, the boundary layer thickness approximately equals [63]

$$\delta(x) \approx 5\sqrt{\frac{\nu x}{u_g}}. \tag{3.10}$$

In the above equation, ν is the kinematic viscosity (defined as the ratio of the gas viscosity to density, $\nu = \mu/\rho$), x is the distance the gas has flowed over the plate, and u_g is the free stream gas velocity in the reactor. Then, the average value of the boundary layer thickness is expressed with

$$\bar{\delta} = \frac{1}{L}\int_0^L \delta(x)dx = \frac{10}{3}\sqrt{\frac{\nu L}{u_g}} \sim \frac{1}{\sqrt{u_g}}, \tag{3.11}$$

where L is the reactor specific length. The main message from the Eq. 3.10 and Eq. 3.11 is that the boundary layer thickness is inversely proportional to the square root of the gas velocity. Hence, the growth rate in the diffusion-controlled regime (Eq. 3.8) increases with the increase of the gas velocity in the reactor as

$$r \sim \sqrt{u_g}. \tag{3.12}$$

This dependence was observed experimentally [59].

The gas velocity is related to the volumetric flow Q_V in the reactor by formula

$$Q_V = \frac{dV}{dt} = S\,\frac{dx}{dt} = Su_g. \tag{3.13}$$

S stays for the area of MOVPE liner cross-section formed by a plane normal to the gas flow direction. It is clearly seen that the values of the gas velocity and the volumetric flow are proportional to each other, which is intuitive and not surprising. Therefore, increasing any of those two is equivalent and will increase the growth rate in the diffusion-controlled regime proportionally to the square root of the value.

In the MOVPE technology, mass flow controllers (MFCs) are used for regulation of the flows in the reactor. MFCs measure the gas flow in the terms of volumetric flow at standard conditions[2] and typically express it in the unit of standard cubic centimeters per minute (sccm). For a given gas, the volumetric flow measured at standardized conditions can be identified with the mass flow. Mass flow is given with equation

$$Q_m = \frac{dm}{dt}, \tag{3.14}$$

where m denotes mass, and t stays for time. The value of the mass flow is related to the volumetric flow. Deriving dt from the Eq. 3.13 and substituting it to the Eq. 3.14, one gets

$$Q_m = \frac{dm}{dV}\, Q_V = \rho\, Q_V. \tag{3.15}$$

Assuming steady flow of a homogeneous gas, the density $\rho = m/V = nM/V$, where n is number of moles and M is the molar mass of the gas. Using the ideal gas law[3], it is easy to show that

$$Q_m = \frac{Mp}{RT}\, Q_V, \tag{3.16}$$

where R is the gas constant, and p and T denote pressure and temperature, respectively. In general, the mass transported (mass flow) by certain volumetric flow varies with the pressure and the temperature, and depends on the gas composition. However, at standard conditions for a given gas $\rho = Mp_{Std}/(RT_{Std}) = const.$ Therefore, the standardized volumetric flow directly refers to, and can be used to describe, the mass flow.

Typical conditions in a MOVPE reactor are far from the standard conditions. Therefore, to calculate the gas velocity in the reactor, first the real volumetric gas flow has to be calculated according to the equation

$$Q_V = \frac{T}{T_{Std}} \cdot \frac{p_{Std}}{p}\, Q_{V,Std}, \tag{3.17}$$

where T_{Std} and p_{Std} denote the standard temperature and pressure, T and p are the reactor temperature and pressure, and $Q_{V,Std}$ is the total gas flow (TGF) in the reactor measured at the standard conditions.

In this thesis, the TGF value will be used to describe the stream in the reactor. One has to remember about the consequences of this convention. While it is handy to operate with values directly measured by MFCs, the values apply only to the MOVPE with the specific cross-section area of the reactor. If one would like to repeat the experiments in a reactor of different size, the parameters would need to be recalculated using the Eq. 3.13.

So far the influence of the TGF value expressed in sccm on the deposition rate was described in detail and discussed with respect to the diffusion-limited growth regime. But

[2]The standard conditions: $T_{Std} = 273.15$ K (0 °C) and $p_{Std} = 1013.25$ mbar

[3]A remainder from the author: $pV = nRT$

how does the gas velocity affect the rate in the kinetic regime? If the reaction kinetics limits the growth process, it means that the amount of reactants diffusing towards the surface is higher than the amount consumed in the surface reactions. Intuitively, for given temperature the growth rate should not change, since the surface is suffused with the reactants. But this logic assumes that the whole *magic* of the MOVPE process happens on the substrate surface. This is not necessarily true! Before reaching the substrate and while diffusing through the boundary layer, the mixture of a carrier gas and precursors is exposed to the heat emitted by the heater and hot susceptor. The precursors pyrolysis and pre-reactions start and take place already in the gas-phase [59, 60]. Gas-phase reactions lead to a change of reactants transfered to the substrate surface, which consequently can affect the surface reaction rate constant. The fraction of the precursors reacted in the gas-phase depends on the gas-phase reaction rate constant k and the residence time of the precursors in the reactor. The residence time can be defined as the time needed for the gas to travel from the front edge of the susceptor to the front edge of the wafer used in epitaxy. Let us denote this distance as x_{sub} – the position of the substrate on the susceptor in direction of the gas flow. Then, the residence time is expressed as $t_r = x_{sub}/u_g$. Assuming the first order reaction, the fraction of the decomposed precursors equals

$$\alpha = 1 - \exp\left(-\frac{kx_{sub}}{u_g}\right). \tag{3.18}$$

While the gas velocity u_g increases, the decomposition parameter α decreases. Therefore, it is expected that also the amount of the decomposed source molecules diffused to the substrate surface will be reduced. This can change the growth rate in the kinetic-controlled regime. The growth rate reduction with the increase of the TGF value in the reactor has been observed experimentally for GST alloys [5]. Additionally, the gas-phase reactions can influence the deposited solid composition, that also has been discussed in the literature [60].

Total pressure in the reactor

The growth rate dependence on the total pressure in the MOVPE reactor is not directly revealed in the Eq. 3.5. The problem is complex and, again, the final effect will depend on the growth regime. First, let us take assumption that the total pressure is the only parameter which will be varied in this consideration. Second, it is important to mention that the TGF value in the reactor is assumed to be constant. As a consequence, while changing the total pressure, also the gas velocity varies according to the Eq. 3.17 and Eq. 3.13. The increase of the total pressure will lead to reduction of the gas velocity in the reactor. Therefore, it will rise the boundary layer thickness (Eq. 3.11) and decrease the growth rate (see Eq. 3.12). Moreover, lower value of the gas velocity will extend the residence time, enhancing the effect of gas-phase pre-reactions. This can boost parasitic deposition of the materials on the reactor walls and further decrease the growth rate.

The effect has been reported in the literature [58, 61]. On the other hand, in the kinetic-controlled regime, increase of the residence time will speed up the deposition, as it has already been discussed previously. The influence of the reactor pressure on the precursors decomposition and on the growth of GST via MOVPE has been observed and reported by Schuck et al. [4].

Partial pressure of precursors

The effect of precursors partial pressures on the growth rate is intuitive. The higher the partial pressures, the higher the growth rate [59, 62]. This correlation is revealed in the Eq. 3.5. Notice that the mole fraction y_i can be expressed with the partial pressure of the reactant

$$y_i = \frac{n_i}{n} = \frac{p_i}{p}, \tag{3.19}$$

where n and p are the total number of moles and the total pressure in the reactor, respectively. In the same manner, n_i and p_i denote the number of moles and the partial pressure of given precursor i. As one can expect, the ratio of the precursors partial pressures will influence the composition of the deposited solid [60, 64, 65]. Therefore, it is important to have control over the partial pressures during the epitaxy.

The amount of reactants injected into the reactor is regulated with MFCs, as already mentioned earlier. Some of the source compounds exist in the gas phase (hydrides, e.g., AsH_3, NH_3). MO materials are mostly delivered in a liquid phase, sometimes solid, packed in so-called bubblers. A bubbler is a kind of sealed bottle with a special design. An arrangement of a bubbler in MOVPE system is presented schematically in Fig. 3.4. Carrier gas bubbles through the MO compound and gets saturated with its vapor. The gas flow through the source is denoted in the picture as $Q_{m,s}$ – source flow. The compound equilibrium vapor pressure p_v is regulated by the temperature of the source (T_s), which is placed in a thermal bath. The source flow mixes with so-called push flow $Q_{m,p}$. A pressure controller (PC) controls the pressure p_b in the bubbler and is an injection path of the mixture into a run line leading to the MOVPE reactor. Further, the mixture is diluted in the carrier gas flow $Q_{m,c}$ of the run line. Final partial pressure of the MO reactant in the reactor is expressed as [66]

$$p_{MO} = \frac{Q_{m,s}}{Q_{m,t}} \cdot \frac{p_v(T_s)}{p_b}\ p. \tag{3.20}$$

In the above equation p is the reactor pressure, and $Q_{m,t}$ is the value of TGF in the reactor. Note that $Q_{m,t}$ is a sum of flows from all sources and lines in the MOVPE setup, and that the flows are given in sccm.

Gaseous sources are usually delivered to MOVPE systems pressurized in bottles. The dopant line configuration was used for the hydride source while carrying on experiments for this thesis. Scheme of the line is shown in Fig. 3.5. The source gas is sealed in a bottle. The hydride concentration in the source gas equals C_h. Before injection into the reactor,

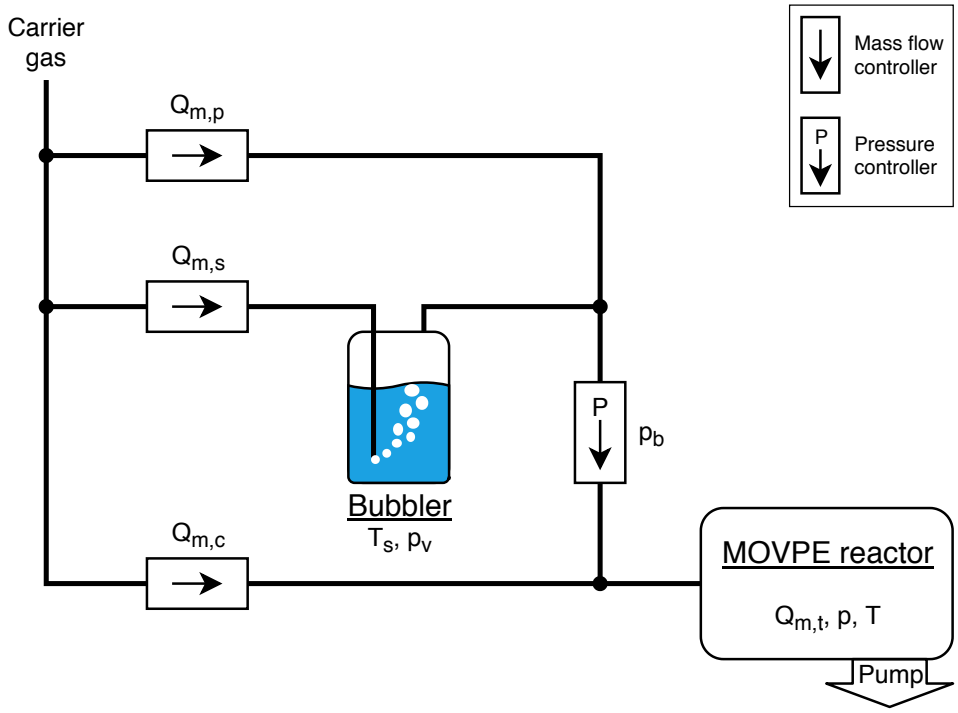

Figure 3.4: An arrangement of a bubbler in the MOVPE system. The carrier gas bubbles through the MO source and gets saturated with its vapor.

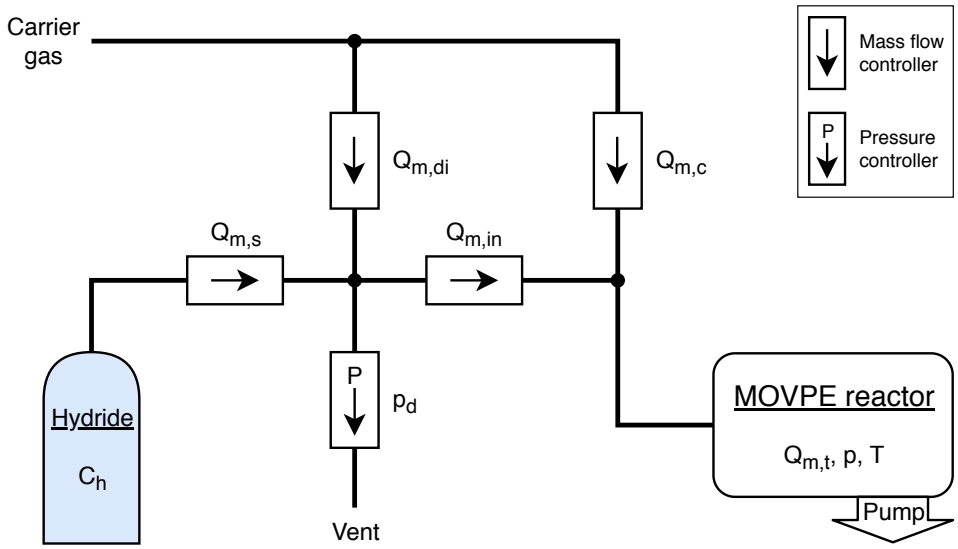

Figure 3.5: Dopant line configuration for a gaseous precursor source. Before injection into the MOVPE reactor (flow $Q_{m,in}$), the source gas (flow $Q_{m,s}$) is diluted with the carrier gas (flow $Q_{m,di}$).

the flow $Q_{m,s}$ from the source bottle is diluted in the carrier gas flow of $Q_{m,di}$. The pressure p_d in the dopant line is controlled with a PC. The flow $Q_{m,in}$ of the diluted source gas is injected into a hydride run line and transfered to the reactor. As earlier, the total reactor pressure is p, the TGF value in the reactor is $Q_{m,t}$, and the flows are given in sccm. Then, the partial pressure of the hydride molecules in the reactor is given with the equation

$$p_h = \frac{C_h \, Q_{m,s}}{Q_{m,s} + Q_{m,di}} \cdot \frac{Q_{m,in}}{Q_{m,t}} \, p. \tag{3.21}$$

3.1.2 MOVPE 1119

One of the setups in the facilities of Peter Grünberg Institute (PGI-9) at Research Center Jülich is the MOVPE 1119, the system used for the growth of the samples reported in this thesis. The MOVPE 1119 is a horizontal low-pressure Aixtron AIX200 reactor equipped with *in situ* LayTec reflectometer EpiR-M-TT. A bulk graphite susceptor is used in the reactor as a sample holder and an absorber of the heater radiation. The susceptor dimensions are 150 mm × 77 mm × 26 mm – length, width, height, respectively. A place for a quarter of 2 inch wafer is profiled in the middle of the susceptor, so the levels difference between the susceptor and the substrate surface is reduced, to avoid a disturbance of the laminar flow during epitaxy. There is no sample rotation in the system. The liner in the reactor is 88 mm wide and 31 mm high over the susceptor surface, resulting in a cross-section area of 2728 mm^2. The temperature in the reactor is monitored with two thermocouples placed inside of the susceptor. One of the thermocouples gives a feedback signal for the heater controller. Flows in the system and pressures of the sources are controlled with MFCs and PCs, respectively. Three run lines are available: two MO lines (MO1 and MO2) and one hydride line. Fig. 3.6 shows schematically the arrangement of the lines and sources in the MOVPE 1119. In the scheme, MFCs are marked with Fx, and PCs with Px (where x is a number). The functions and operating ranges of all controllers are listed in Tab. 3.1. The MO1 line is a transfer path for triethylantimony (TESb), diethyltelluride (DETe) and trimethylindium (TMIn). One more DETe source is connected to the MO2 line. The hydride line is used to deliver digermane (Ge_2H_6) to the reactor. While working on experiments for this thesis, only the MO1 and the hydride line were used to transfer TESb, DETe and Ge_2H_6 to the reactor. The dopant line was applied for injection of digermane to the reactor. During the growths, the MO2 line was flushed with the constant carrier gas flow of 200 sccm.

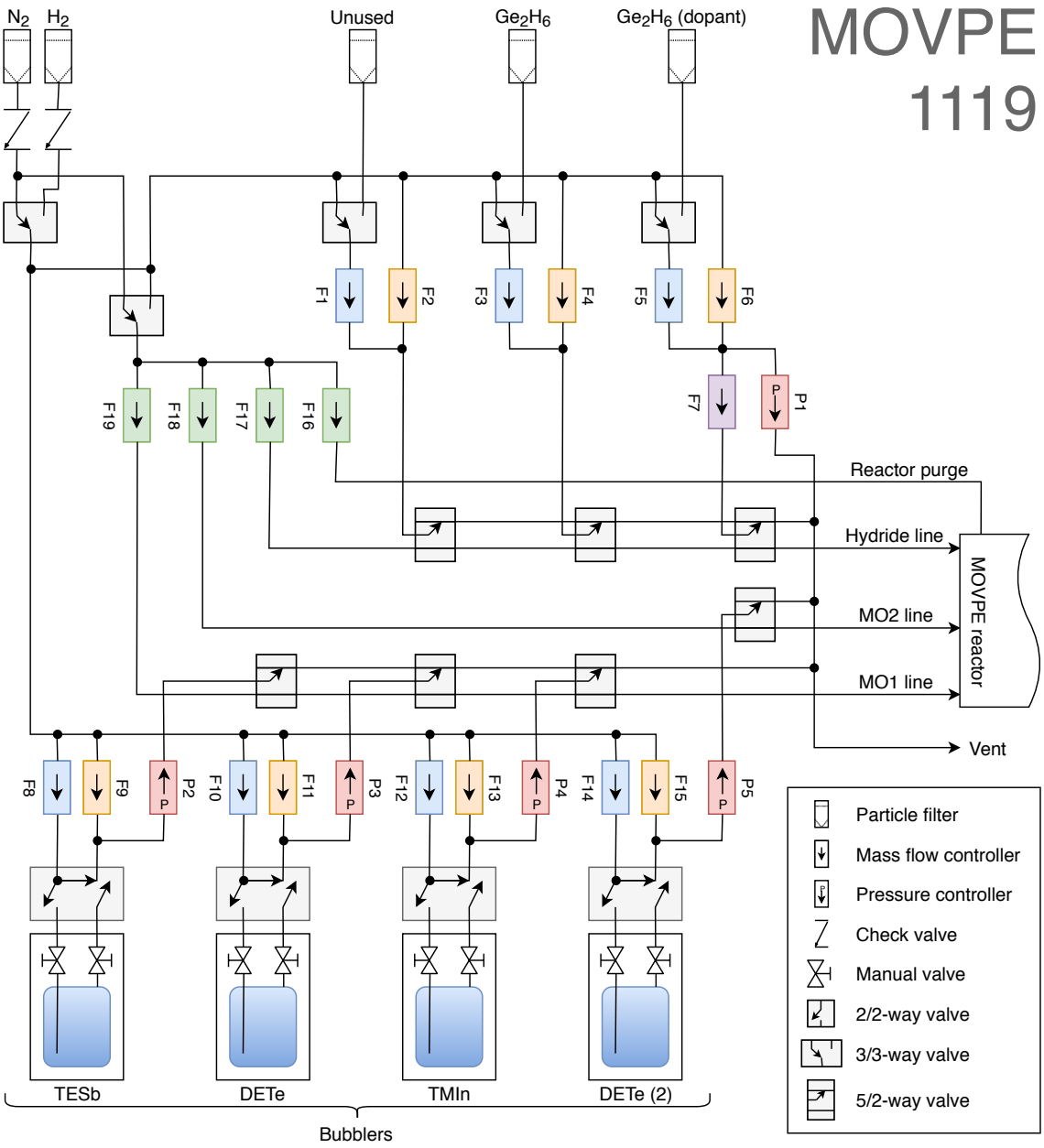

Figure 3.6: Scheme of the MOVPE 1119. MFCs and PCs are denoted with Fx and Px, respectively (x is a number). The functions and operating ranges of used controllers are listed in Tab. 3.1. In the picture, the PCs are marked in red. The MFCs are colored in blue, orange, purple and green. The color corresponds to the function of the controller: source, push, inject and run line, respectively.

Table 3.1: Functions and operating ranges of MFCs and PCs used in the MOVPE 1119.

MFC/PC	Function	Range	
F1	Hydride (1) source (unused line)	100	sccm
F2	Hydride (1) push (unused line)	100	sccm
F3	Ge_2H_6 source	500	sccm
F4	Ge_2H_6 push	100	sccm
F5	Ge_2H_6 (dopant) source	50	sccm
F6	Ge_2H_6 (dopant) push	50	sccm
F7	Ge_2H_6 (dopant) inject	50	sccm
P1	Ge_2H_6 (dopant) pressure	1900	mbar
F8	TESb source	500	sccm
F9	TESb push	500	sccm
P2	TESb pressure	1900	mbar
F10	DETe source	500	sccm
F11	DETe push	1000	sccm
P3	DETe pressure	1900	mbar
F12	TMIn source	50	sccm
F13	TMIn push	1000	sccm
P4	TMIn pressure	1900	mbar
F14	DETe (2) source	50	sccm
F15	DETe (2) push	1000	sccm
P5	DETe (2) pressure	1900	mbar
F16	Purge line	2000	sccm
F17	Hydride line	5000	sccm
F18	MO2 line	1000	sccm
F19	MO1 line	5000	sccm

3.1.3 Precursors and possible reactions in the system

Digermane [Ge_2H_6 (10% in H_2)], triethylantimony [$(C_2H_5)_3Sb$] and diethyltelluride [$(C_2H_5)_2Te$] were used as chemical sources for deposition of GST alloys. The models of the molecules are shown in Fig. 3.7.

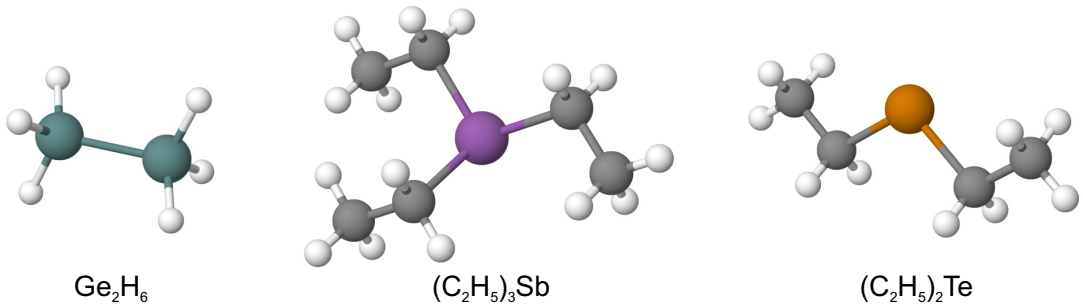

Figure 3.7: Models of molecules for the precursors used in the work. From left to right: digermane, triethylantimony and diethyltelluride. White balls represent hydrogen, gray – carbon, turquoise – germanium, violet – antimony and orange – tellurium.

Digermane is stored pressurized in a bottle. Bubblers are used for the MO sources, TESb and DETe, kept at 10 °C (283.15 K) and 17 °C (290.15 K), respectively. The temperature dependences of the vapor pressure for the MO precursors are given with[4]

$$\log p_v(\text{mmHg}) = 7.90 - 2183/T(\text{K}) \qquad \text{for TESb,} \tag{3.22}$$

$$\log p_v(\text{mmHg}) = 7.99 - 2093/T(\text{K}) \qquad \text{for DETe.} \tag{3.23}$$

The partial pressures of the precursors were calculated as described in section 3.1.1.

After the precursors are injected through the run lines into the reactor, they start to mix, heat up, and finally decompose and react. There is no one ultimate way of a reaction, the whole process is complex and difficult to describe. The least stable compound in the system is Ge_2H_6, with pyrolysis activation energy of 141 kJ·mol^{-1}. The decomposition reaction of Ge_2H_6 was investigated in detail within the narrow range of the temperatures, 210-222 °C [67]. Observed reaction is described by the equation[5]

$$Ge_2H_6 \longrightarrow 1.18\ GeH_4 + 0.49\ H_2 + 0.82\ GeH_{0.3}. \tag{3.24}$$

It was also found that the amount of GeH_4 produced in the reaction is reduced while the Ge_2H_6 thermal decomposition proceeds in the presence of propene (C_3H_6). At the same time, propene is converted to polymers and production of hydrogen increases. Slowing down the Ge_2H_6 pyrolysis by an organic compound might be essential in the MOVPE process, since organic ligands are released when MO compounds decompose. The presence

[4] 1 mmHg ≈ 1.333224 mbar

[5] $GeH_{0.3}$ describes the composition of the deposit on the walls of the reactor

of hydrogen does not show significant influence on the amount of the reaction products. Emeléus and Gunter Jellinek [67] suggested the following path for the pyrolysis of Ge_2H_6

$$Ge_2H_6 \longrightarrow 2\ GeH_3, \tag{3.25}$$

$$GeH_3 + Ge_2H_6 \longrightarrow GeH_4 + Ge_2H_5, \tag{3.26}$$

$$Ge_2H_5 \longrightarrow GeH_2 + GeH_3, \tag{3.27}$$

$$GeH_2 \longrightarrow Ge + H_2, \tag{3.28}$$

$$2\ GeH_2 \longrightarrow GeH_4 + Ge, \tag{3.29}$$

$$n\ GeH_2 \longrightarrow (GeH_2)_n. \tag{3.30}$$

Lu and Crowell [68] used Fourier-transform infrared spectroscopy for the investigation of Ge_2H_6 adsorption and pyrolysis on the Ge(111) surface. The experiment was done in an ultrahigh vacuum chamber, with a base pressure $\sim 10^{-10}$ mbar. It was found that already at 150 K adsorbed on the surface Ge_2H_6 converts to chemisorbed GeH_3. While gradually heating up the substrate to the room temperature (300 K), GeH_3 decomposes to di- and monohydride: GeH_2 and GeH. The decomposition proceeds with further increase of the temperature. At the temperature of 600 K (326.85 °C), no hydrides were found on the surface. The typical growth temperatures used for deposition of GST alloys via MOVPE are above 400 °C. Therefore, although the fraction of precursor decomposed in the gas-phase depends on its residence time in the reactor atmosphere, it is expected that after reaching the substrate surface remaining Ge_2H_6 decomposes very rapidly and only Ge is involved in the layer deposition. Hydrogen, being the second product of Ge_2H_6 pyrolysis, may influence the surface reactions of the MO compounds.

The MO precursors used for the epitaxy of GST are more stable compounds, compared to Ge_2H_6. Thermal decomposition of TESb was investigated at temperatures up to 650 °C, under the pressure $< 10^{-1}$ mbar [69]. In the gas-phase, the precursor shows stability up to 400 °C. The activation energy of the TESb decomposition was found to be 183 kJ·mol^{-1}. The main products of the precursor thermolysis are ethene (C_2H_4), ethane (C_2H_6) and *n*-butane (C_4H_{10}). The formation of the last product, *n*-butane, is more pronounced at high temperatures. It is proposed that TESb adsorbs on the surface by the loss of an ethyl ligand. The loss of the remaining ligands results in deposition of an antimony atom and formation of surface ethyl groups. Two ethyl groups, or ethene and ethane, can react and form *n*-butane. Also, the ethyl groups might exchange a hydrogen atom between themselves, with the surface, or in this particular case with decomposing Ge_2H_6, and be desorbed as ethene and/or ethane. The process is schematically presented in Fig. 3.8 and

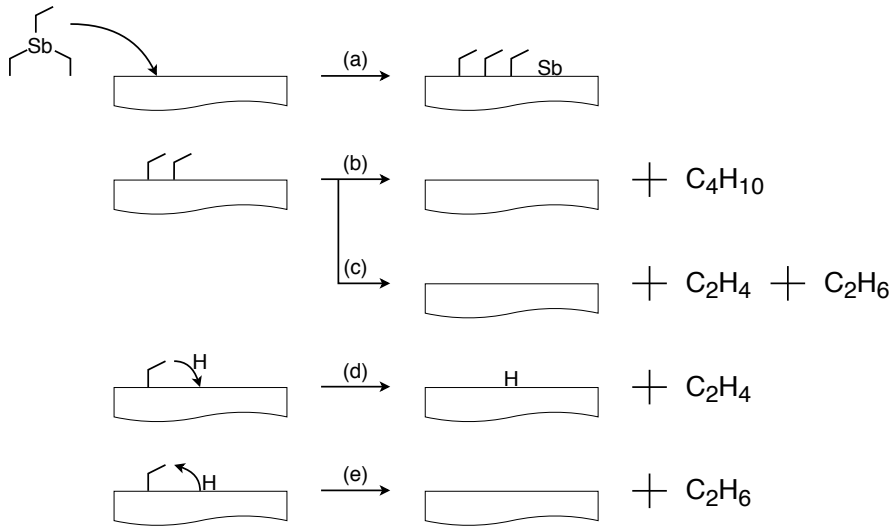

Figure 3.8: Schematic presentation of the TESb thermolysis reaction: (a) adsorption and migration of ethyl ligands to the surface; (b) formation of *n*-butane from two surface ethyl groups; (c) desorption of two ethyl groups as ethene and ethane; (d) formation of a surface hydrogen and desorption of an ethyl group as ethene; and (e) recombination of ethyl group with a surface hydrogen and desorption as ethane. Taken from Bahlawane et al. [69].

can be described with the sequence of reactions

$$(C_2H_5)_3Sb \longrightarrow 3\ C_2H_5^{\bullet} + Sb(s), \tag{3.31}$$

$$2\ C_2H_5^{\bullet} \longrightarrow C_2H_{10}, \tag{3.32}$$

$$2\ C_2H_5^{\bullet} \longrightarrow C_2H_4 + C_2H_6, \tag{3.33}$$

$$C_2H_5^{\bullet} \longrightarrow C_2H_4 + \tfrac{1}{2}H_2, \tag{3.34}$$

$$\tfrac{1}{2}H_2 + C_2H_5^{\bullet} \longrightarrow C_2H_6. \tag{3.35}$$

The standard enthalpy of formation $\Delta_f H^{\ominus}$ for ethene, ethane and *n*-butane is equal to 52.39 kJ·mol^{-1}, −83.96 kJ·mol^{-1} and −125.96 kJ·mol^{-1} [70], respectively. Then, using the Hess's law

$$\Delta_f H^{\ominus}_{reaction} = \sum \Delta_f H^{\ominus}_{products} - \sum \Delta_f, H^{\ominus}_{reactants} \tag{3.36}$$

for the reaction

$$C_2H_4 + C_2H_6 \longrightarrow C_4H_{10}, \tag{3.37}$$

the change of the standard enthalpy approximately equals $\Delta_f H^{\ominus}_{reaction} \approx -94$ kJ·mol^{-1}. So, the reaction is exothermic and, although conditions in the reactor are far from the standard conditions, an additional heat could be released in the reactor during the deposition process. However, one has to remember that the peak of *n*-butane formation was observed around 600 °C, which is much higher than usual temperatures used for the deposition of GST in this work.

The decomposition mechanism of DETe, the last of used precursors, is similar to the process described for TESb. The overall reaction proceeding during a deposition might be written as

$$(C_2H_5)_2Te \longrightarrow C_4H_{10} + Te(s). \tag{3.38}$$

In the above reaction, the formation of *n*-butane in the surface decomposition process is assumed. The presence of hydrogen in the reaction atmosphere can influence the process and support the production of ethane

$$(C_2H_5)_2Te + \tfrac{1}{2}H_2 \longrightarrow C_2H_6 + Te(s). \tag{3.39}$$

Hydrogen should not effect the deposition of tellurium. The activation energy for the decomposition of DETe was calculated to be around 167 kJ·mol^{-1} [71].

The formation of *n*-butane was not observed while conducting experiments on the pyrolysis of DETe below 500 °C [72], in He and H_2 atmosphere. It was proposed that the gas-phase decomposition may be preferred, proceeding in the following manner

$$(C_2H_5)_2Te \longrightarrow C_2H_4 + C_2H_5TeH, \tag{3.40}$$

$$C_2H_5TeH \longrightarrow C_2H_6 + \tfrac{1}{2}Te_2, \tag{3.41}$$

$$C_2H_5TeH \longrightarrow C_2H_5{}^{\bullet} + TeH^{\bullet}, \tag{3.42}$$

$$TeH^{\bullet} \longrightarrow \tfrac{1}{2}Te_2 + \tfrac{1}{2}H_2. \tag{3.43}$$

The activation energy for the reaction given in the Eq. 3.40 was found to be about 209 kJ·mol^{-1} [71–73]. In both described mechanisms of DETe decomposition (on the surface and in the gas-phase), ethene, ethane, and *n*-butane can be formed. But, as it has already been mentioned, while discussing the decomposition of TESb, the temperatures in the MOVPE reactor during the GST growth are most likely too low to cause the effective formation of *n*-butane.

Czerniak and Easton [74] investigated dependence of the DETe decomposition on temperature whilst a clean reactor was first heated up and then cooled down. The result of their experiment is shown in Fig. 3.9. They found that the pyrolysis is more efficient during cooling down, comparing to the same temperature when heating up. The experiment was repeated without cleaning the reactor, with tellurium deposited on the walls. The pyrolysis started at lower temperature and was less abrupt than in the first run. The result suggested that the pyrolysis of DETe is an autocatalytic process. The hysteresis in the temperature dependence of the DETe decomposition was also observed while the pyrolysis proceeds in the presence of diethylzinc, $(C_2H_5)_2Zn$ [73].

The activation energies, together with the values of the pre-exponential frequency factor for the Arrhenius equation (Eq. 3.7), are summarized in Tab. 3.2.

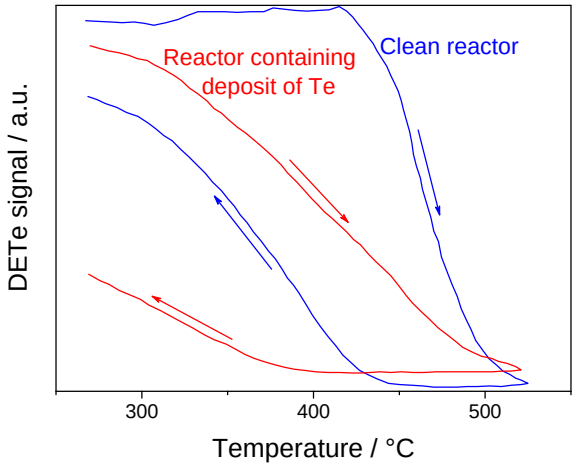

Figure 3.9: The temperature dependence of the DETe pyrolysis in a clean reactor (blue curve) and in a reactor with a deposit of tellurium (red curve). Taken from Czerniak and Easton [74].

Table 3.2: The frequency factors and the activation energies of the thermal decomposition for the precursors.

Precursor	A / $\mathbf{s^{-1}}$	E_a / $\mathbf{kJ{\cdot}mol^{-1}}$	**Reaction**	**Ref.**
Ge_2H_6	$2.44 \cdot 10^{13}$	141	Eq. 3.25	[67]
TESb	$1.00 \cdot 10^{13}$	183	Eq. 3.31	[69]
DETe	$1.00 \cdot 10^{12}$	167	Eq. 3.38	[71]
DETe	$5.00 \cdot 10^{13}$	209	Eq. 3.40	[71, 72]

3.1.4 Si(111) substrate

The depositions of GST alloys were carried out on quarters of 2 inch Si(111) wafers. The ⟨111⟩ orientation of the wafer was chosen due to the surface symmetry. In general, Si is described with the diamond cubic crystal structure (face-centered cubic), space group $FD\bar{3}m$ (No. 227). The lattice constant at room temperature is $a \approx 5.43053(7)$ Å [75]. The unit cell of Si is depicted in Fig. 3.10 (a). The Si crystal has threefold symmetry in ⟨111⟩ direction. Therefore it makes perfect substrate for the deposition of hexagonal GST compounds. The in-plane surface lattice constant of unreconstructed Si(111) is $a_{Si(111)} = 5.43053 \text{ Å}/\sqrt{2} \approx 3.84$ Å. Fig. 3.10 (b) shows the formation and orientation of the Si(111) surface in relation to the unit cell, and (c) reveals the threefold symmetry of the surface.

Before the growth, each silicon wafer was cleaned chemically to remove organic residues and the native oxide from the surface. The procedure started with 10 min dip in piranha solution – the mixture of sulphuric acid and hydrogen peroxide in the ratio of 1:1

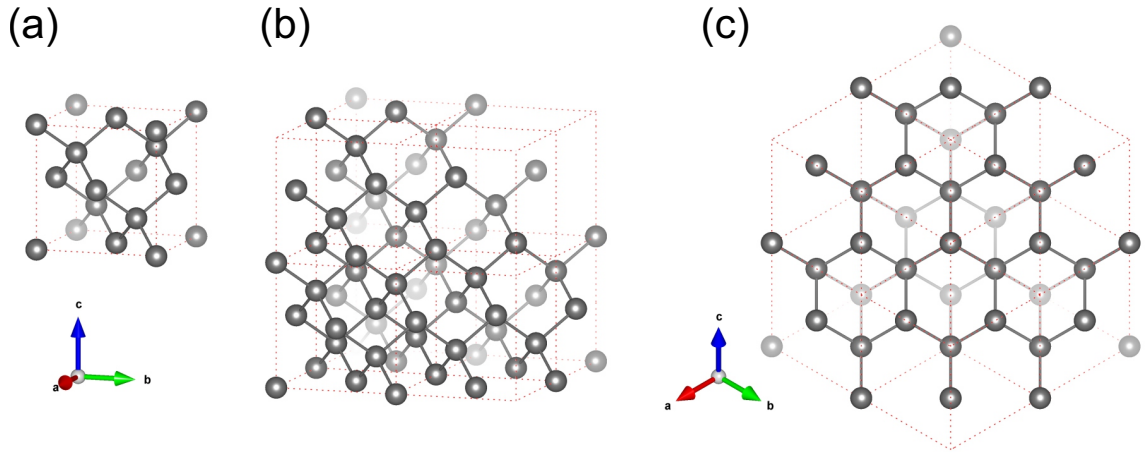

Figure 3.10: The crystal structure of silicon: (a) the unit cell; (b) eight unit cells cleaved along (111) crystallographic plane; and (c) unreconstructed Si(111) surface – projection of (b) along ⟨111⟩ direction.

[H_2SO_4(96%):H_2O_2(30%)]. The piranha etch removes any organic contaminants from the surface. Next, the wafer was rinsed in deionized (DI) water for at least 2 min, until the rainbow-like color film of residual acid was dissolved and disappeared from the surface. Then, the substrate was dipped for 5 min in hydrofluoric acid [HF (1%)], to remove the native oxide. In the end, the wafer was again rinsed in DI water, this time for 1 min, dried under the nitrogen spray gun and transfered immediately into the MOVPE reactor.

3.2 Characterization methods

Advanced experimental techniques were applied for characterization of samples morphology, crystal structure, composition, and electrical properties. This section shortly discusses used characterization methods and information yielded from them. For more details regarding the specific technology, working principles, and physics behind the measurement, one should check cited literature.

3.2.1 *In situ* reflectometry

The MOVPE 1119 is equipped with *in situ* LayTec reflectometer EpiR-M-TT. Therefore, the *in situ* reflectance measurement was the first method employed for the characterization of deposited samples, giving information about the grown layer already during the epitaxy process. The arrangement of the reflectometer in the MOVPE 1119 system is presented schematically in Fig. 3.11. The incident beam is partially reflected and partially transmitted into the layer. The fraction of reflected radiation depends on the refractive

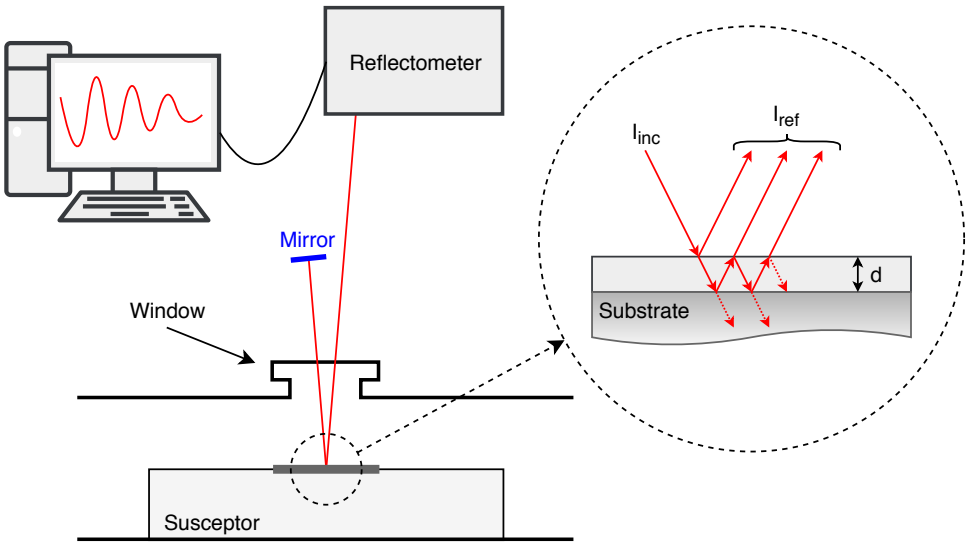

Figure 3.11: The arrangement of the *in situ* reflectometer in the MOVPE 1119 (proportions not kept) and sample closeup with shown Fabry-Pérot interference geometry.

index and the extinction coefficient of the layer material. Assuming normal incidence[6], the layer reflectance is expressed with

$$R = \frac{I_{ref}}{I_{inc}} = \frac{(n-1)^2 + \kappa^2}{(n+1)^2 + \kappa^2}, \tag{3.44}$$

where n and κ are the refractive index and the extinction coefficient of the layer material, respectively.

Epitaxial layer is a thin film of a material. The transmitted part of the incident beam again partially reflects from the layer/substrate interface. This leads to Fabry-Pérot interference conditions, depicted in the sample closeup in Fig. 3.11. Therefore, Fabry-Pérot oscillations can be observed in the time-resolved reflectance signal. Knowing the oscillations period T, the wavelength of used radiation λ, and the refractive index n of the layer material, one can calculate the growth rate

$$r = \frac{\lambda}{2nT}. \tag{3.45}$$

The above equation holds well for layer-by-layer growth, while fails for islands growth mode. The roughness of the layer and the absorption coefficient of material influence the measured signal intensity. Thus, proper choice of the probing wavelength is essential for the experiment.

Integrated with MOVPE 1119, LayTec EpiR-M-TT reflectometer is able to measure in the spectral range from 0.8 eV (1550 nm) to 3.1 eV (400 nm). To find an optimal

[6] Although the back-reflecting mirror is used in the setup (as shown in Fig. 3.11), the beam incident angle is nearly zero. Such configuration is possible, ensuring sufficiently large distance from the mirror to the sample, comparing to the size of the mirror.

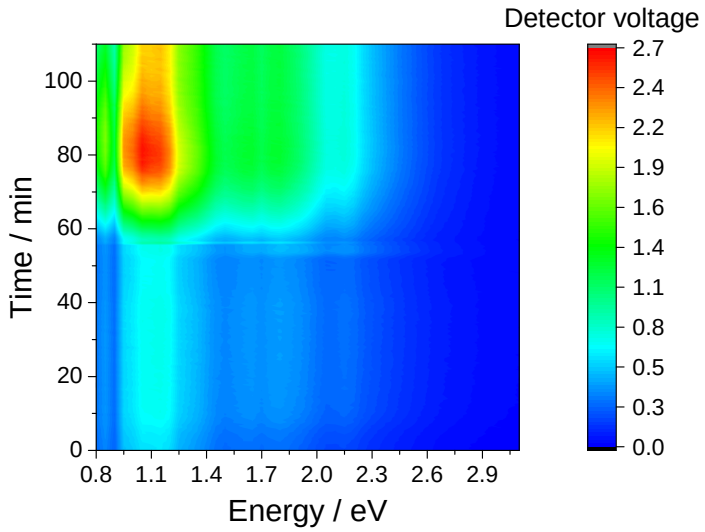

Figure 3.12: Spectrally- and time-resolved *in situ* reflectance recorded during growth of $Ge_1Sb_2Te_4$. The highest contrast in the time-resolved signal is visible for the wave energies around 1.1 eV.

wavelength for the *in situ* time-resolved measurements of GST samples, a spectrally- and time-resolved measurement was performed over a growth run of a $Ge_1Sb_2Te_4$ layer. The recorded color plot is shown in Fig. 3.12. No Fabry-Pérot oscillations are visible in the plot. This is because $Ge_1Sb_2Te_4$ is a narrow band gap material, with a band gap of 0.44 eV (in stable hexagonal phase) [19]. Even lower values were reported [21]. The band gap energy is below the bottom energy limit of the reflectometer. Thus, high absorption is expected, which suppresses Fabry-Pérot oscillations. The biggest change in the intensity of the signal is found for the energies around 1.1 eV (1127 nm). Therefore, the value of 1.1 eV was chosen to monitor the growth of GST samples. The penetration depth in a GST layer for electromagnetic radiation with energy of 1.1 eV is in the range of ∼100 nm [22, 76]. Thereby, the growth rate calculation can be difficult to perform and less precise, but the intensity of the measured signal yields information about the surface roughness. A rougher surface will scatter more radiation and reduce the intensity of the detected signal.

3.2.2 Electron microscopy

Electron microscopy employs a focused beam of electrons for observation and characterization of a sample at nanometer to micrometer scale. In scanning electron microscopy (SEM) the image is obtained by scanning the surface of the sample with an electron beam. Different types of signals are produced while the electrons interact with the sample. These signals include secondary electrons and backscattered electrons – two main signals used for imaging with SEM. Secondary electrons are outer shell electrons of the specimen atoms, which gained sufficient kinetic energy in the process of inelastic scattering of the electron beam to be emitted from the atom and escape the sample. The probability that secondary

electron will escape the sample decreases with the depth, at which the emitting atom is situated under the surface of the sample. The depth of emission depends on the material and ranges from 5 nm to 50 nm. Due to shallow sampling depth, secondary electrons are suitable to produce high-resolution micrographs of the sample surface. Backscattered electrons are electrons that interacted with the specimen in elastic scattering events and left to the sample surface. Elastic scattering of electrons depends on the atomic number Z of the atom they interact with. Therefore, the backscattered signal is characterized by Z-contrast and carries information about subsurface details of the sample structure [77].

Another electron microscopy method is scanning transmission electron microscopy (STEM). Here, the recorded signal comes from electrons transmitted through a thin electron-transparent specimen. Typically, thickness of the specimen is in the order of 5–100 nm [78]. The STEMs are usually operated at an acceleration voltage of 100–300 kV and the measurements are performed with use of a bright-field and/or an annular dark-field detector. The bright-field detector is an axial detector located in the path of transmitted electron beam and is used for the phase-contrast imagining. The annular dark-field detector is an annulus-shaped detector placed in the optical far field beyond the specimen[7] [79]. High-angle annular dark-field (HAADF) refers to particular configuration of STEM setup. In the HAADF-STEM a short camera length is used, to ensure that diffracted to small angles Bragg-scattered electrons do not reach the annular dark-field detector. Therefore, the signal detected in the HAADF-STEM comes from electrons scattered to high angle (larger than 5°) in the elastic Rutherford forward scattering process. In the HAADF-STEM, a specimen is scanned with electron beam and the total intensity of the Rutherford-scattered signal is saved as a function of the beam position. The intensity of the high-angle elastic scattering shows Z^2 dependence on the atomic number of target atom [80, 81]. Thus, the contrast in a HAADF-STEM image allows to distinguish heavier elements from lighter. If the specimen contains atoms of which atomic numbers differ significantly, the image yields information about the location and distribution of the elements.

Energy dispersive X-ray spectroscopy (EDX) adds analytical capabilities to the electron microscopy methods. In the EDX interaction of the beam electrons with inner shell electrons of the specimen atoms is utilized to recognize the sample composition. The incident beam electron can eject an electron from a shell and ionize the specimen atom. The ion with missing inner shell electron is in an excited energetic state. The relaxation process occurs within the time of around 1 ps, through allowed transition of an outer shell electron into vacancy in the inner shell. Each element has defined energies of electrons in the shells – atomic energy levels. Therefore, also the energetic differences between shells are characteristic for the element. The energy released during the relaxation process can be transfered to another outer shell electron and eject it from the atom in the Auger process. Or, the difference between shell energies can be emitted in the form of a photon

[7] The annular dark-field detector records the signal only in the presence of a specimen in the system, otherwise it stays **dark**.

– characteristic X-ray radiation. In the EDX, characteristic X-ray spectrum is recorded and analyzed to extract the information about the sample composition. Typically, X-rays studied in the EDX have energies of 0.1 keV to 20 keV [77].

In this work, Zeiss Gemini 1550 SEM was used for characterization of the samples morphology. The SEM was operated at 20 kV and the images were recorded with high-resolution InLens secondary electrons detector. The measurement is nondestructive, so it was the prime method employed for qualitative evaluation of the deposited samples (layer coalescence, roughness). The SEM can be also used for quantitative analyses of such parameters as deposited crystals size, nucleation density and other values, which are measurable or countable during post-measurement image processing.

The HAADF-STEM images were taken with FEI Titan G2 80–200 ChemiSTEM microscope operated at the acceleration voltage of 200 kV. In the material system of interest, the atomic numbers of Ge, Sb and Te are equal to 32, 51 and 52, respectively. The atomic number of Ge differs much from the atomic numbers of Sb and Te, which have neighboring values. Since the signal intensity in HAADF-STEM micrographs is Z^2 dependent, it is expected to observe in the images a low intensity at points corresponding to the sites where a Ge atom is situated between heavier elements. The contrast and averaged intensity profiles extracted from HAADF-STEM images were successfully used to resolve the stacking sequence in epitaxial GST [5, 31].

The composition of the samples was analyzed using the Hitachi SU8000 SEM equipped with Oxford X-Max^N 80 EDX detector. Accelerating voltage of 10 kV was used for the measurement. The measurements were carried out at few spots on the sample and compared. If the results were uniform over the sample, the average composition was calculated. The SEM-EDX is fast to proceed and nondestructive method. However, measured composition is an averaged over the measurement spot and no composition profile is possible to extract. Furthermore, the accuracy of the measurement is limited to few percent, thus the compositional analysis of the sample was supported by other experiments.

3.2.3 Atomic force microscopy

While SEM is a perfect tool for qualitative evaluation of the sample surface, atomic force microscopy (AFM) is more suitable for quantitative characterization, e.g., using root mean square (RMS) roughness. The AFM is a type of scanning microscope capable to take images even with atomic resolution. In the AFM, the sample surface is scanned with a tip placed on a spring cantilever. The end of the cantilever is lighted with a laser beam, which is reflected to a position-sensitive detector. The detector records the vertical position and the deflection of the cantilever [82]. The cantilever has a given free resonant frequency. While the tip approaches the sample, at first it is attracted by long-range vdW interactions. Later, when it gets into contact with the sample, repulsive force appears, arising from the overlapping of the tip and the sample atoms electron orbitals. Both, the attractive and repulsive interactions modify the resonant frequency of the cantilever. This effect is

used in so-called tapping mode AFM, which prevents the tip from sticking to the sample and reduces tip/sample degradation [83]. In the tapping mode, the cantilever oscillates driven by a force with the frequency near its resonant frequency. If the distance between the tip and the sample changes during scanning of the surface, it affects the cantilever resonant frequency and changes the oscillation amplitude [84]. The vertical position of the cantilever is then adjusted by a feedback loop, to preserve the oscillation amplitude. This position reflects the topography of the sample surface.

National Instruments Nanoscope III AFM operated in the tapping mode was employed in this research. Images with the resolution of 512×512 px^2 were taken with the scan rate set between 0.5 Hz and 2.0 Hz, for smoother and rougher samples, respectively. The RMS roughness of the surface was calculated from the area of 15×15 μm^2. The roughness was used for quality evaluation and quantitative comparison of the samples grown under different conditions. While for smooth layers the results of the measurement are rather repeatable, this does not have to be the case for rough and nonuniform surfaces. The roughness can varied between the measurements taken at different spots on the sample, therefore the experimental data were collected from few locations on the surface of each investigated layer and an average roughness was calculated.

3.2.4 X-ray diffraction

X-ray diffraction (XRD) is a powerful and nondestructive characterization method, giving detailed information about the epitaxial layer crystal structure and its alignment with respect to the substrate. The technique utilizes the interaction of X-ray beam with atoms ordered in a crystal lattice. The incident X-ray beam scatters on atoms in crystalline samples. If scattered waves are in phase, they interfere constructively and diffraction beam appears in a specific direction. The possible directions of the diffracted beam depend on the wavelength of X-ray radiation and the structure of the examined sample. The relation is described by well-known Bragg's law [85]

$$2d_{hkl} \sin\theta = n\lambda, \tag{3.46}$$

where d_{hkl} is interplanar spacing between $\{hkl\}$ crystal planes, θ is the incident angle [the angle between the incident beam and the (hkl) plane], n is an integer representing the order of the reflection, and λ is the wavelength of the incident X-rays.

Bruker D8 diffractometer was used for structural and compositional XRD characterization of the samples. Various scan geometries yield different information about the characterized sample. The basic and extensively used in experimental work performed for this thesis is a simple 2θ-θ scan. In such a scan, the detector and the specimen rotate in the same direction around the diffractometer axis. The angular velocity of the detector is double of that for the sample [86]. In the 2θ-θ diffractogram of a monocrystal with (hkl) orientation, only $(nh\ nk\ nl)$ reflections are found, where n represents the order of the re-

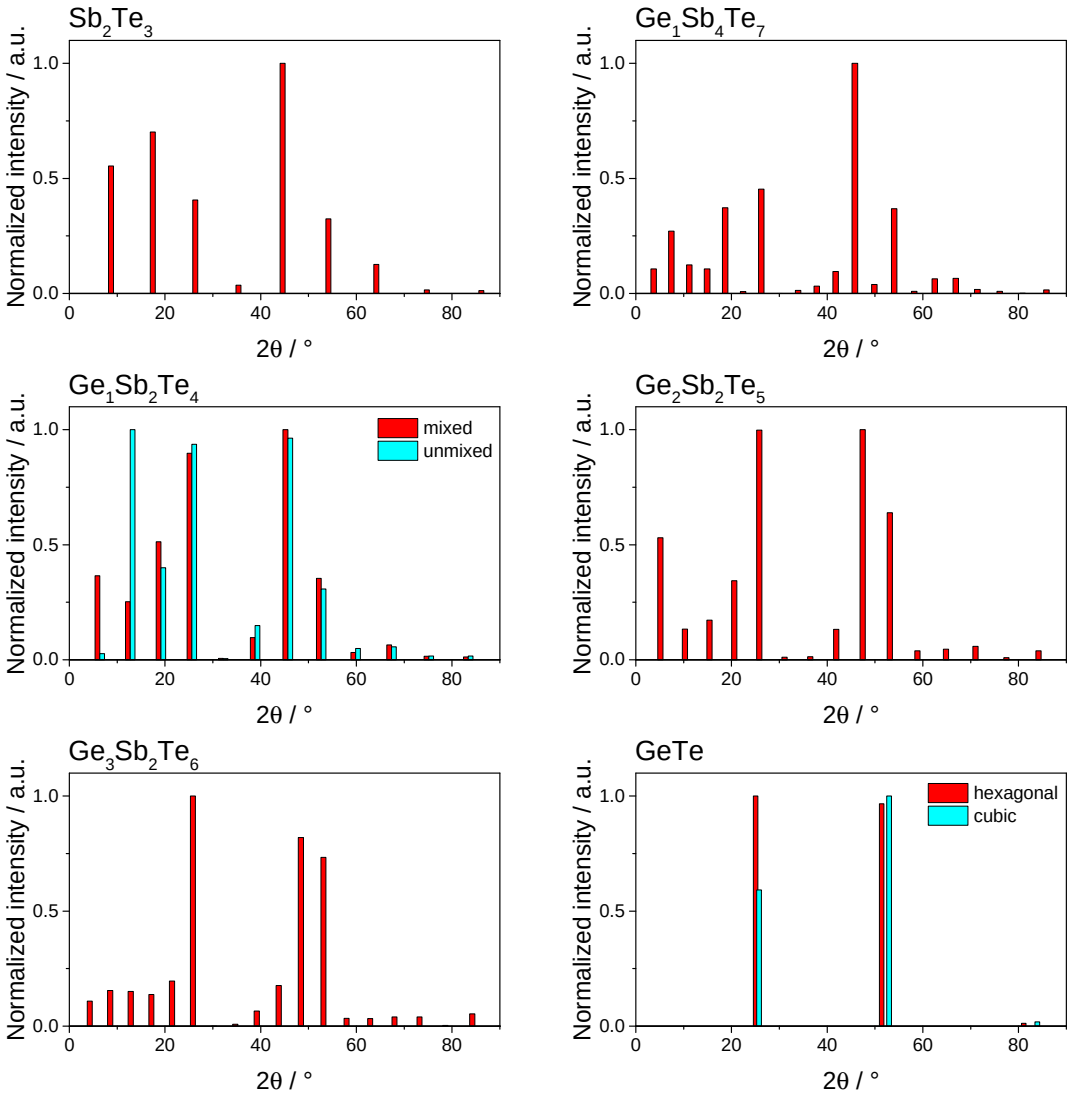

Figure 3.13: Simulated XRD 2θ-θ diffractograms for materials along the GeTe-Sb_2Te_3 pseudo-binary line. Peaks in the diffractograms correspond to $(00l)$ reflections [(hhh) for cubic GeTe]. The reflexes were normalized to the intensity of the strongest reflection. Using the XRD 2θ-θ scan one can determine the composition of the deposited layer. Moreover, it is possible to resolve the cation layers configuration in $Ge_1Sb_2Te_4$, since the intensity of reflections differs significantly for the mixed and unmixed case.

flection. For GST samples grown on the Si(111) substrate, $(00l)$ reflections were recorded in 2θ-θ scans. Simulated diffractograms with $(00l)$ reflexes, (hhh) in case of cubic GeTe, for crystals of different composition along the GeTe-Sb_2Te_3 pseudo-binary line are shown in Fig. 3.13. The simulations were done using the VESTA software [87]. It is easy to notice that with XRD 2θ-θ scan one can determine the stoichiometry of GST crystal, since the positions of reflexes vary with the material composition. Furthermore, in the case of $Ge_1Sb_2Te_4$, there is a noticeable difference between the intensity of peaks in diffractograms

of a crystal with mixed and of a crystal with unmixed cation layers. Thanks to this, it is possible to resolve the configuration of the cation layers, which was successively done and reported [5, 31].

Other scanning geometries were also employed for the characterization of the samples. Pole figures, or simpler ϕ-scans, were recorded to check the presence of rotational twin domains in the deposited layer and their alignment with respect to the Si substrate. In a ϕ-scan measurement, the position of the detector is fixed and the specimen is rotated around the normal direction to the sample surface. A pole figure can be obtained by tilting the specimen and changing the tilt angle χ during the measurement. This will give information about the layer texture too [88]. The layer quality can as well be evaluated with rocking curve measurement – a scan with a fixed position of the X-ray source and detector, and the incident angle θ changed by rocking the sample (ω-scan). Also, reciprocal space maps (RSMs) were recorded and analyzed to determine the lattice constants of grown materials.

3.2.5 Other methods

Other experimental methods were also employed for characterizations of chosen samples. The thickness of layers was measured with Rutherford backscattering spectrometry (RBS), a characterization method employing the elastic Coulomb scattering of a high energy ion beam on specimen nuclei [89]. The composition and distribution of the elements in layers were analyzed with secondary-ion mass spectrometry (SIMS) and atome probe tomography (APT), both are destructive methods. In SIMS primary ion beam is used to erode the sample surface. This leads to the formation of a secondary ion beam of specimen elements, which is then collected and analyzed with a mass spectrometer [89]. The second method, APT, allows detecting the situation of individual elements in a three-dimensional needle-shaped sample. In APT, the specimen is held at positive voltage and ions are evaporated from it, e.g., with a laser pulse. Next, the ions are accelerated towards the detector and based on the recorded signal three-dimensional image of the specimen is reconstructed [90]. The results of SIMS and APT were compared with those received from XRD and EDX measurements. Finally, the electrical characteristics of fully coalesced layers were determined in Hall effect measurements. In the experiment, the Hall voltage is utilized to determine the electrical properties of a sample. The Hall voltage is an electrical potential difference across a sample conducting electric current in presence of an external magnetic field. Squared 7×7 mm^2 samples in the van der Pauw geometry were used during the Hall effect measurements.

Chapter 4

Results and discussion

4.1 Growth of Ge-Sb-Te alloys

The influence of pre-annealing atmosphere, TGF in the reactor (gas velocity) and growth temperature on deposition of GST alloys was investigated in detail. All samples were grown for 60 min on a quarter of a Si(111) wafer. The substrate was cleaned chemically right before the growth according to the procedure described in subsection 3.1.4. The growth started with 30 min pre-annealing at 690 °C. If not mentioned differently, the annealing prior to the deposition of GST was done in H_2 atmosphere. Then the temperature was reduced to the growth temperature. Pure N_2 was used as a carrier gas [91]. The Si surface was pretreated with Ge_2H_6 and TESb for 2 min. Strong effect of pretreatment with Ge and Sb precursors on GST deposition, especially surface coverage and layer coalescence, have been reported in the literature before [4, 92]. After the pretreatment, a 2 min break in the precursors supply was introduced and only the carrier gas flow was preserved. Finally, the proper growth of GST started for one hour. The total pressure in the reactor was identical during all growth sessions and kept at 50 mbar. The partial pressures of the precursors were fine-tuned around those reported by Schuck et al. [4]. For all growth runs of GST alloys they were kept constant at values given in Tab. 4.1. The details about growth procedure for GST alloys are presented in Tab. 4.2.

Table 4.1: Partial pressures of precursors used for the growth of GST alloys.

Precursor	**Partial pressure / mbar**
Ge_2H_6	$7.16 \cdot 10^{-3}$
TESb	$4.78 \cdot 10^{-3}$
DETe	$1.33 \cdot 10^{-1}$

Table 4.2: The growth procedure and parameters used for the deposition of GST alloys. The parameters written in dark red were investigated in detail.

	Annealing	**Cooling**	**Pretreatemnt**	**Break**	**Growth**
t / min	30	7-11	2	2	60
Carrier gas	**H_2**	N_2			
T / °C	690	decreases	**465-485**		
p / mbar	50				
TGF / sccm	lower than during GST growth, dependent on flows from used precursor sources				**2100-3250**

4.1.1 Pre-annealing atmosphere

The impact of Si substrate annealing prior to deposition of GST by MOVPE has already been investigated [4]. The studies show, that an annealing for 20 min at 680 °C in H_2 atmosphere enhances the Si surface coverage and GST layer coalescence. The annealing at high temperature is a cleaning step of Si surface. It aims at desorption of hydrogen adatoms and gaseous impurities adsorbed from the air during transportation of the substrate from the chemical hood (after cleaning) to the MOVPE reactor. The influence of annealing atmosphere on the growth was not examined in the study by Schuck et al. [4]. The flow and pressure of H_2 during annealing process is well controlled. However, one should consider the influence of parasitic deposition in the reactor, which could cause a memory effect. During the annealing the susceptor is heated up to a temperature of 690 °C. At this point it is hard to control the desorption of material from the reactor walls. Desorbed materials could deposit and diffuse into the Si substrate while it is annealed or cooled down to the growth temperature. This would change the surface properties and potentially affect the growth of GST. Moreover, since pyrolysis of DETe is an autocatalytic reaction [74], presence of parasitic deposition in the reactor can affect the fraction of the decomposed DETe, especially at the beginning of growth when the reactor atmosphere is not saturated with products of the decomposition reaction. To check whether the desorption of parasitic material influences the growth or not, the effect of annealing atmosphere on the deposition of GST was investigated. To this end, six samples were prepared: one reference and five with varied pre-annealing atmosphere. The substrate annealing temperature of 690 °C was the same for all samples. The details about the annealing conditions of the samples are presented in Tab. 4.3.

First, a reference sample was grown in the standard for MOVPE 1119 operation fashion. Before the run, the reactor was neither chemically nor thermally cleaned. A GST layer was grown for 60 min at 475 °C with the TGF value of 3000 sccm. Prior to the growth of GST, the Si substrate was annealed for 30 min at 690 °C in H_2 atmosphere with a

Table 4.3: List of samples grown on Si substrates pre-annealed at varied conditions. The annealing temperature and the growth parameters for GST were unchanged.

Sample	Bake-out	Annealing atmosphere
Reference	no	H_2
No. 2	yes	H_2
No. 3	yes	H_2 + DETe
No. 4	yes	N_2 + DETe
No. 5	yes	H_2 + TESb
No. 6	yes	28 min H_2 + 2 min (H_2 + DETe)

flow of 2182 sccm. Before the next run, the reactor was baked-out for an hour in pure H_2 atmosphere. A bake-out is a thermal cleaning procedure, which aims at suppression of desorption from the reactor walls during the pre-growth annealing. During the bake-out, the reactor temperature and pressure change from 600 °C to 800 °C and from 10 mbar to 500 mbar, respectively. The bake-out procedure consists of four 15 min steps, while the temperature and pressure vary in a sequence:

800 °C, 500 mbar → 600 °C, 10 mbar → 800 °C, 500 mbar → 600 °C, 10 mbar.

After the bake-out, next sample was grown using exactly the same recipe as for the reference sample. SEM micrographs of the reference sample and the sample grown after reactor bake-out are shown in Fig. 4.1 (a) and (b), respectively. The difference is clearly visible. In the SEM image of the reference sample fully coalesced GST layer is visible, while on the surface of sample grown after the reactor bake-out only islands of the material are found. This is strong indication, that there is a memory effect in the reactor caused by desorption of parasitic material. Considering that vdW epitaxy is common in the case of chalcogenides, it is reasonable to assume that Si surface is saturated with Te atoms. Dangling bonds on the surface disturb heteroepitaxy of a layered material. A termination of Si surface dangling bonds with Te allows vdW growth, starting with quasi-vdW gap [93]. Deposition of chalcogenides on Te-terminated Si surface via MBE have also been reported in the literature [94, 95].

In purpose of verification if the observed memory effect is caused by passivation of Si surface with Te atoms, a third sample was grown. The sample was deposited after the reactor bake-out. This time, the substrate was pre-annealed for 30 min in H_2 atmosphere with an addition of DETe. During the annealing, the mass flow of DETe was identical as the flow used for the growth of GST. The growth took place in DETe partial pressure

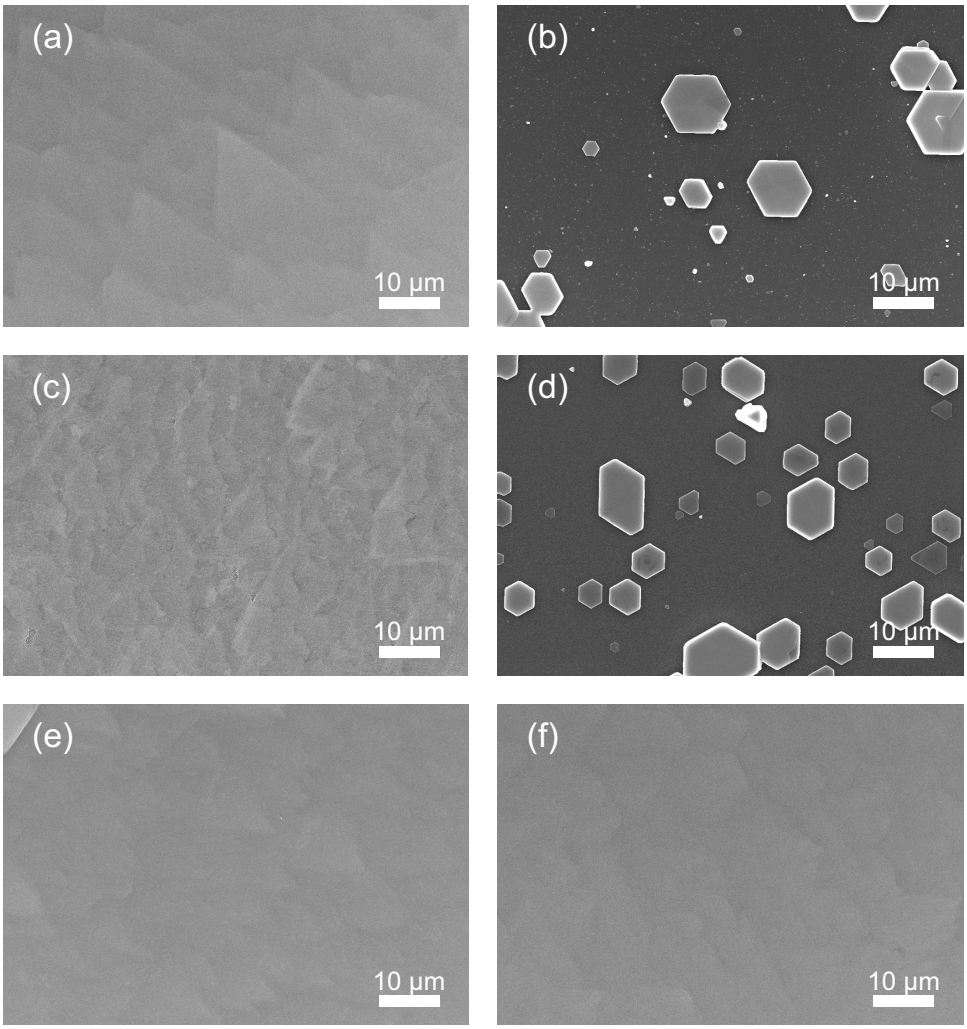

Figure 4.1: SEM micrographs of $Ge_1Sb_2Te_4$ grown on Si(111) annealed for 30 min at 690 °C in varied atmospheres. Image (a) presents reference sample grown in uncleaned reactor. Prior to the growth of samples (b)-(f), the reactor was baked-out for one hour. The samples were grown on Si(111) substrates annealed in the following conditions: (a) and (b) 30 min in pure H_2; (c) 30 min in H_2 with addition of DETe; (d) 30 min in N_2 with addition of DETe; (e) 30 min in H_2 with addition of TESb; and (f) 28 min in pure H_2 plus 2 min in H_2 with addition of DETe.

of $1.54 \cdot 10^{-1}$ mbar and 400 sccm higher TGF[1] value of 2582 sccm. The SEM image of the grown layer is presented in Fig. 4.1 (c). The growth yields a fully coalesced layer, similarly like in the case of the reference sample. Consequently, the presence of Te in the annealing atmosphere is essential for the deposition of fully coalesced and uniform GST layers. However, it also rises a question about the role of H_2 in the pre-annealing. Does it really support cleaning of the surface from gaseous impurities as it was indicated by Schuck et al. [4]? To verify this concern, another sample was prepared (Tab. 4.3, sample

[1]The TGF during annealing was tested in the range of 1685-2600 sccm. No noticeable influence on GST layers structure and morphology was found.

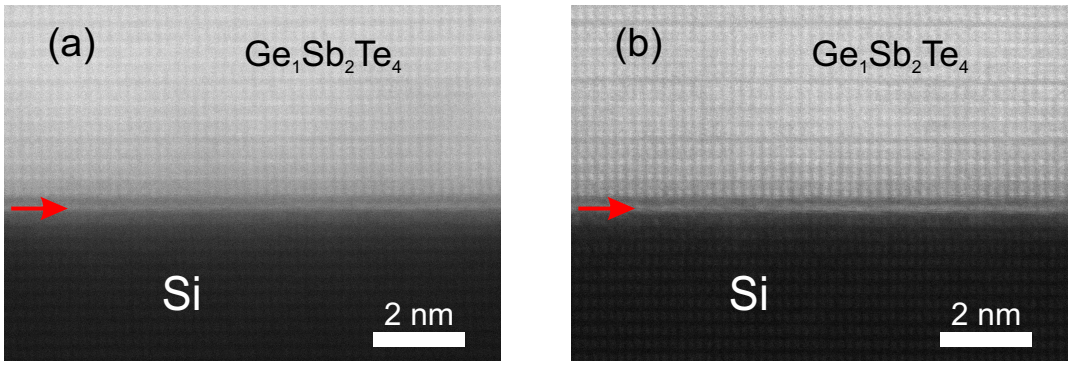

Figure 4.2: HAADF-STEM images of GST/Si interface: (a) the reference sample grown in uncleaned (no bake-out) reactor after the annealing of Si substrate in H_2 atmosphere; and (b) sample grown after the reactor bake-out and annealing of Si substrate in H_2 atmosphere with the addition of DETe. Red arrows mark Te wetting layer. The wetting layer is followed by vdW gap and further by blocks of $Ge_1Sb_2Te_4$. Images are projected along $[1\bar{1}0]_{GST}/[211]_{Si}$.

No. 4). In the annealing atmosphere, H_2 was replaced with N_2, but DETe flow was kept the same. All other growth parameters were kept constant, including the reactor bake-out before the growth. Again, the change in morphology is clearly visible in the SEM picture shown in Fig. 4.1 (d). As in the case of the sample grown after the reactor bake-out and pre-annealing in pure H_2 (Fig. 4.1 (b)), only GST islands are found on the Si surface. It shows that the presence of H_2 and Te in the pre-annealign atmosphere is important for the deposition of fully coalesced and uniform GST films via MOVPE. It is suspected that H_2 supports desorption of gaseous impurities from the Si surface and Te supports vdW epitaxy by terminating Si dangling bonds.

HAADF-STEM characterization was carried out around GST/Si interface for the reference sample and the sample grown after annealing in H_2 with the addition of DETe. Recorded images projected along $[1\bar{1}0]_{GST}/[211]_{Si}$ direction are shown in Fig. 4.2. No difference was found between the interfaces of these samples. In both cases, the Si surface is covered with a Te wetting layer. The growth of GST starts with a gap, characteristic for vdW epitaxy. The gap is followed by a GST film composed of blocks containing seven atomic layers, which indicate the $Ge_1Sb_2Te_4$ composition. Fig. 4.3 presents a close-up into Fig. 4.2 (b) around the GST/Si interface. The image was filtered using five points (pixels) moving average filter. Next, the average intensity profile was extracted from the picture and compared with a model $Ge_1Sb_2Te_4$ structure (right-hand side of Fig. 4.3). In HAADF-STEM images with atomic resolution the intensity is approximately proportional to Z^2, where Z is the atomic number of the corresponding element [79]. Since in the investigated samples, Te is an element with the highest atomic number of 52, higher peaks in the intensity profile stem from the Te layers. Nevertheless, in the periodic table a neighbor of Te is Sb with an atomic number of 51. Thus, Te and Sb layers cannot be distinguished from HAADF-STEM images, and it cannot be resolved, if visible wetting

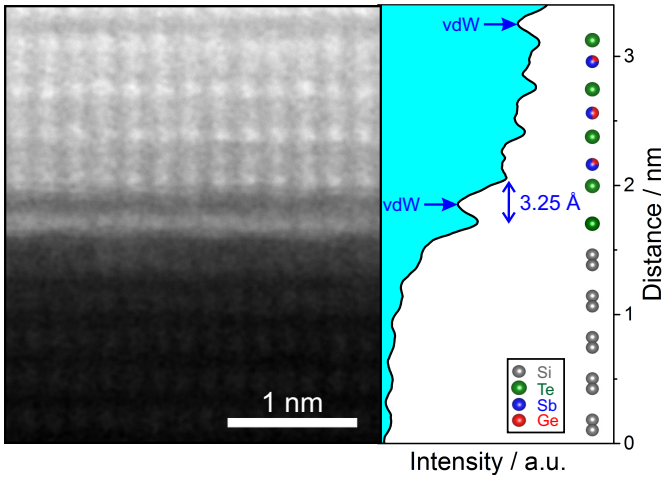

Figure 4.3: HAADF-STEM image of GST/Si interface (close-up into Fig. 4.2 (b)), on the left-hand side, and averaged intensity profile with a model $Ge_1Sb_2Te_4$ structure, on the right-hand side. The vdW gap measure between the substrate and $Ge_1Sb_2Te_4$ layer is marked in the graph. The distance equals 3.25 Å.

layer is purely composed of Te. However, applied growth procedure and pre-annealing in presence of DETe in the reactor give a strong indication that the interface is Te-rich.

Deposition of chalcogenides on Sb terminated substrate has also been reported [96]. Therefore, the next sample was grown on the Si(111) substrate annealed for 30 min in H_2 atmosphere with the addition of TESb (No. 5 in Tab. 4.3). During the pre-annealing, the TESb partial pressure of $3.99 \cdot 10^{-2}$ mbar and the TGF of 2582 sccm were applied. Other growth parameters were unchanged compared to the reference sample. Again, the growth results in deposition of coalesced and uniform layer. The SEM micrograph of the sample surface is depicted in Fig. 4.1 (e). It does not differ from the SEM image of the reference sample. The difference is revealed in the HAADF-STEM images presented in figure Fig. 4.4. In the HAADF-STEM pictures, a wetting layer is exposed on the Si surface. The wetting layer is followed by a vdW gap, and then by a five-atomic-layer segment, which resolves the Sb_2Te_3 composition, as indicated with the intensity profile shown in Fig. 4.4 (b). Further, seven-atomic-layer segments are grown, corresponding to the stable phase of $Ge_1Sb_2Te_4$. Saturation of Si(111) substrate with Sb atoms, prior to deposition of GST, causes the growth to start with a layer of Sb_2Te_3. However, it is not resolved with the HAADF-STEM measurement whether the wetting layer is Sb-rich or Sb atoms are replaced with Te at the beginning of the GST deposition, which could explain the lack of Te in the first segment of the grown film.

Comparing the reference sample with the samples grown on Te-saturated surface and on Sb-saturated surface, a clear similarity is visible between the first two. The HAADF-STEM micrographs taken around GST/Si interface (Fig. 4.2) are basically identical for both, the reference sample and the layer grown after the annealing in H_2 atmosphere with the addition of DETe. Therefore, the presence of Te in the reactor during pre-annealing

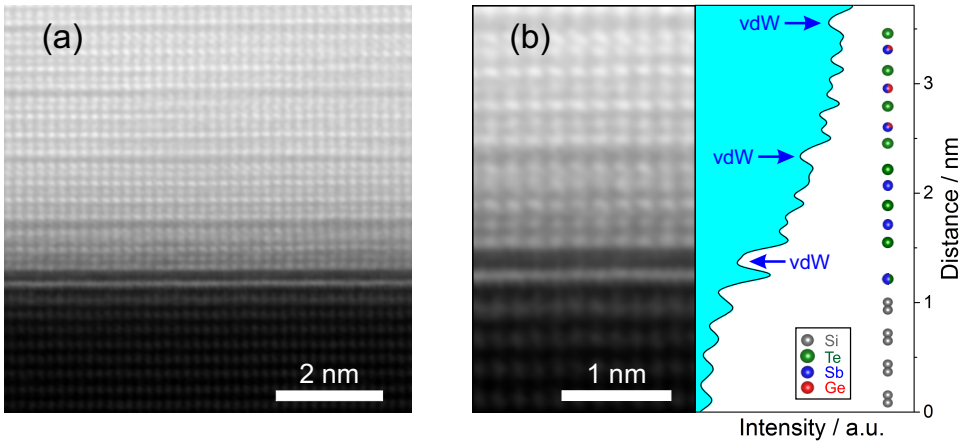

Figure 4.4: (a) HAADF-STEM image around GST/Si interface of the sample grown after substrate pre-annealing in H_2 atmosphere with TESb addition; and (b) close-up to the interface and averaged intensity profile with a model structure. The growth starts with a wetting layer followed by a five-atomic-layer block of Sb_2Te_3. Later seven-atomic-layer blocks are grown, characteristic for $Ge_1Sb_2Te_4$. Images are projected along $[1\bar{1}0]_{GST}/[211]_{Si}$.

is expected to be a crucial factor for the deposition of coalesced GST films via MOVPE. However, injecting DETe into the reactor over the whole 30 min annealing step, is a waste of the source compound since no growth takes place at the time. Hence, it has been verified that injection of DETe into the reactor for only a part of the annealing time is sufficient to terminate the Si(111) surface and this results in the deposition of a coalesced layer. Another sample was grown after the reactor bake-out. This time, the annealing was composed of two steps, both at 690 °C. First, the substrate was annealed in pure H_2 atmosphere for 28 min (TGF of 2182 sccm), and then additionally DETe (partial pressure of $1.54 \cdot 10^{-1}$ mbar) was injected into the reactor and annealing was continued for 2 min yet (TGF of 2582 sccm). Next, GST was deposited in the standard fashion. The growth results in a fully coalesced layer, as depicted in Fig. 4.1 (f). The HAADF-STEM image of the sample is shown in Fig. 4.5. No difference is revealed in the micrograph of GST/Si interface in the sample, compared to the reference. A wetting layer is visible on the Si substrate and the growth starts with a vdW gap followed immediately by $Ge_1Sb_2Te_4$ blocks. The experiment shows that the injection of DETe into the reactor for 2 min in the end of pre-annealing is sufficient to obtain a fully coalesced and uniform $Ge_1Sb_2Te_4$ layer.

The samples grown on Si(111) substrates annealed in various atmospheres were examined extensively using XRD. No compositional differences is resolved in 2θ-θ scans of the specimens, shown in Fig. 4.6 (a), and all samples are found to contain $Ge_1Sb_2Te_4$. The curves indicate the stable hexagonal phase of $Ge_1Sb_2Te_4$ with mixed Ge/Sb layers – concluded from the ratio of observed peaks intensities compared to simulated pattern shown in Fig. 3.13. However, the sample deposited after pre-annealing in pure H_2 atmosphere and the one grown after pre-annealing in N_2 with the addition of DETe (both grown after reactor back-out) are characterized with broad peaks in the diffractograms. Notice, these

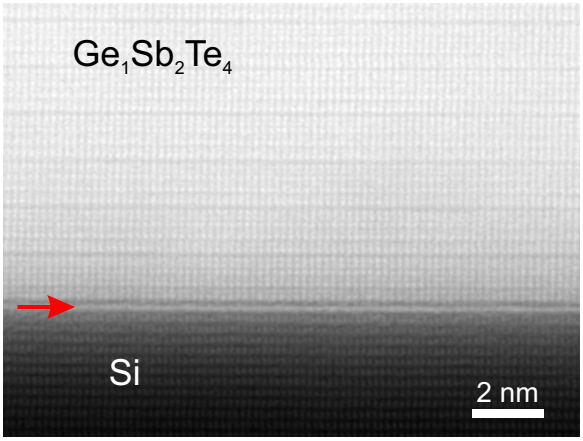

Figure 4.5: HAADF-STEM image around GST/Si interface of the sample grown after 28 min H_2 and 2 min H_2 with DETe pre-annealing of substrate. Red arrow marks wetting layer. Image is projected along $[1\bar{1}0]_{GST}/[211]_{Si}$.

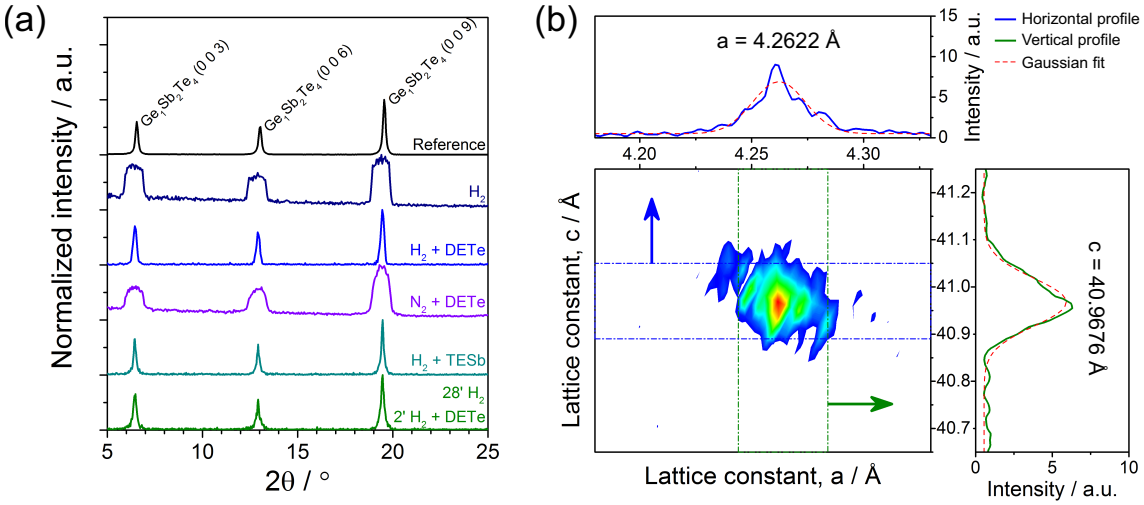

Figure 4.6: XRD characterization of layers grown on Si(111) substrate annealed at 690 °C in various atmospheres: (a) 2θ-θ scans for the samples – the annealing atmospheres are indicated in the chart (next to each curve), $Ge_1Sb_2Te_4$ reflexes are also signed; (b) RSM recorded around (1 0 23) reflection of $Ge_1Sb_2Te_4$ for the sample grown after 30 min substrate annealing in H_2 atmosphere with addition od DETe [H_2 + DETe, blue 2θ-θ curve in (a)].

are the samples which did not form coalesced layer, but triangular islands on the surface, see SEM images in Fig. 4.1. The broadening of the peaks displays the misalignment of the triangular crystals.

Fig. 4.6 (b) presents XRD-RSM measured around (1 0 23) reflection of $Ge_1Sb_2Te_4$ for sample grown after Si substrate annealing in H_2 atmosphere with injection of DETe for 30 min (No. 3 in Tab. 4.3). Intensity profiles were extracted from the map and are depicted on the top and right-hand side of the picture. The profiles are fitted with Gaussian function (red dashed line in the charts) and the lattice parameters for MOVPE-grown $Ge_1Sb_2Te_4$

are measured based on the centers of the peaks. The hexagonal lattice constants are found to be equal to $a = 4.2622$ Å and $c = 40.9676$ Å. The lattice parameters differ slightly from those reported in the literature for sputtered $Ge_1Sb_2Te_4$ with mixed cation layers, $a = 4.27$ Å and $c = 41.69$ Å [13]. The variation of a lattice constant is not significant, more pronounced difference is between the values of c lattice constant. MOVPE-grown $Ge_1Sb_2Te_4$ is characterized by lower value of c, which can be due to higher crystallinity and lower defect density, as discussed in work by Hardtdegen et al. [31].

4.1.2 Total gas flow

In the next step, the influence of the TGF in the reactor on the growth of $Ge_1Sb_2Te_4$ was investigated. The effect of the TGF on MOVPE growth process is discussed extensively in subsection 3.1.1. All samples in the series were grown for 60 min at 475 °C, after 30 min annealing in H_2 atmosphere and 2 min Ge_2H_6-TESb pretreatment of the substrate at the growth temperature. The TGF value was varied in the range from 2100 sccm to 3250 sccm. The flows from sources were adjusted between growth runs to keep the partial pressures of the precursors at values given in Tab. 4.1.

The SEM micrographs of the samples from the series are presented in Fig. 4.7. The SEM images reveal the influence of the gas velocity during the growth on the GST layer morphology. At 2100 sccm, the layer consists of merged triangular islands of the material. While the TGF value increases, the three-dimensional growth is gradually suppressed and surface gets smoother. The growth with the TGF value of 3000 sccm results in fully coalesced layer with surface nearly completely free of triangular islands. The layer is homogeneous and has fish scale texture. The SEM images do not expose any pronounced difference between the morphology of the sample grown with the TGF value of 3000 sccm

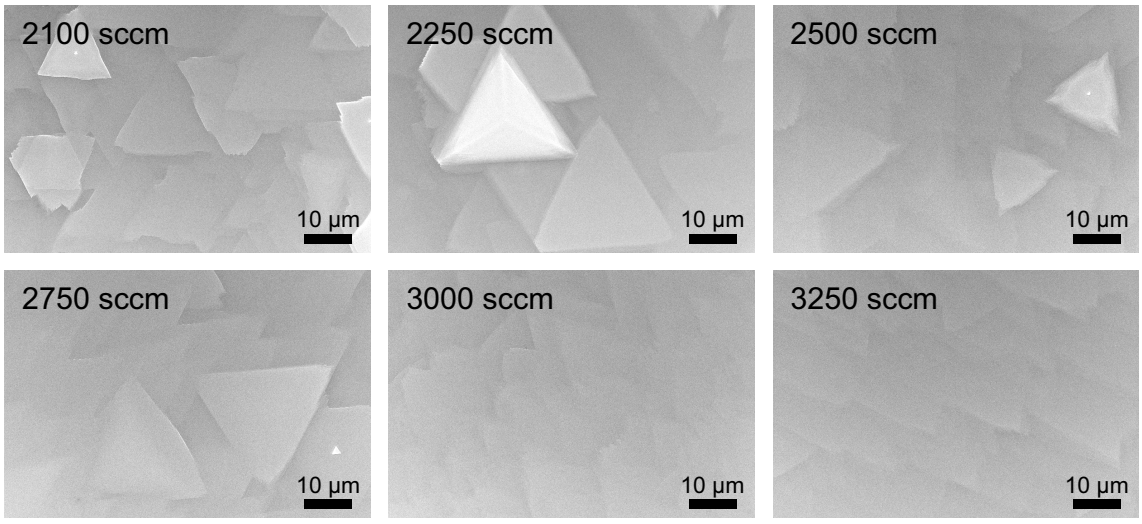

Figure 4.7: SEM images of samples grown with various TGF value – from the range of 2100 sccm to 3250 sccm. The effect on layer morphology is clearly visible.

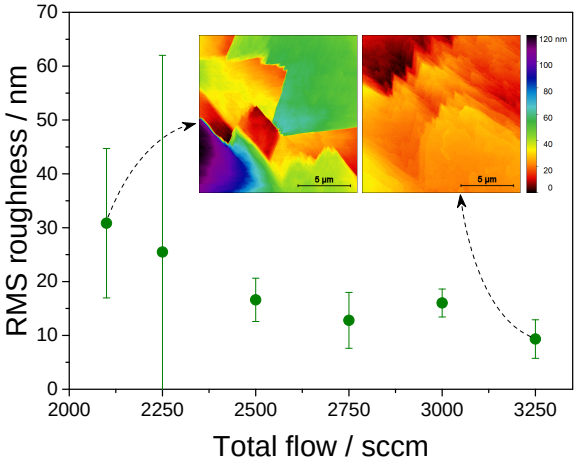

Figure 4.8: AFM measured RMS roughness of samples grown with various TGF value in the reactor during deposition. The roughness values are averages of four to five measurements and error bars mark the standard deviation. The insets in the graph show AFM images of samples grown with TGF value of 2100 sccm (left) and 3250 sccm (right).

and 3250 sccm.

The observations from the SEM pictures are confirmed by AFM quantitative analysis, i.e., the RMS roughness. All samples from the series were measured with AFM at four to six different spots on the surface. For each sample, the averaged RMS roughness was calculated from the pertinent scans. The result is plotted in Fig. 4.8. In the figure, error bars mark the standard deviation, and the color map insets in the figure show examples of AFM images for sample grown with the TGF of 2100 sccm and 3250 sccm. Similarly as in the case of SEM pictures, the change in surface morphology is noticeable in the AFM images. The image for the sample grown with 2100 sccm reveals the height differences on the sample surface in the range of 120 nm, which corresponds to around 29 unit cells of $Ge_1Sb_2Te_4$. For sample grown under TGF of 3250 sccm, this height differences are strongly reduce – below 10 unit cells of $Ge_1Sb_2Te_4$. Calculated RMS roughness further confirm the tendency of the material system to improve the layer morphology with the increase of the TGF value in the reactor. The roughness decreases nearly linearly in the TGF range of 2100-2750 sccm. Later, it stays at the same level, below 20 nm. One should also notice that the standard deviation reduces with the TGF value too. It has extremely high values for low TGFs, but for flows of 2500 sccm and higher, it is rather stable at the level of ~ 5 nm. While the RMS roughness gives an information about the surface morphology at a specific spot on the sample surface, the standard deviation reflects long-range uniformity of the sample. Therefore, the AFM measurements expose overall improvement of the samples morphology with the increase of TGF value in the reactor during the epitaxy.

In the SEM micrographs presented in Fig. 4.7, triangular islands are visible, especially for low TGFs as discussed earlier. Some of the islands point to opposite directions, i.e., they are rotated by 60°. This is an indication for the presence of rotational twin domains in the

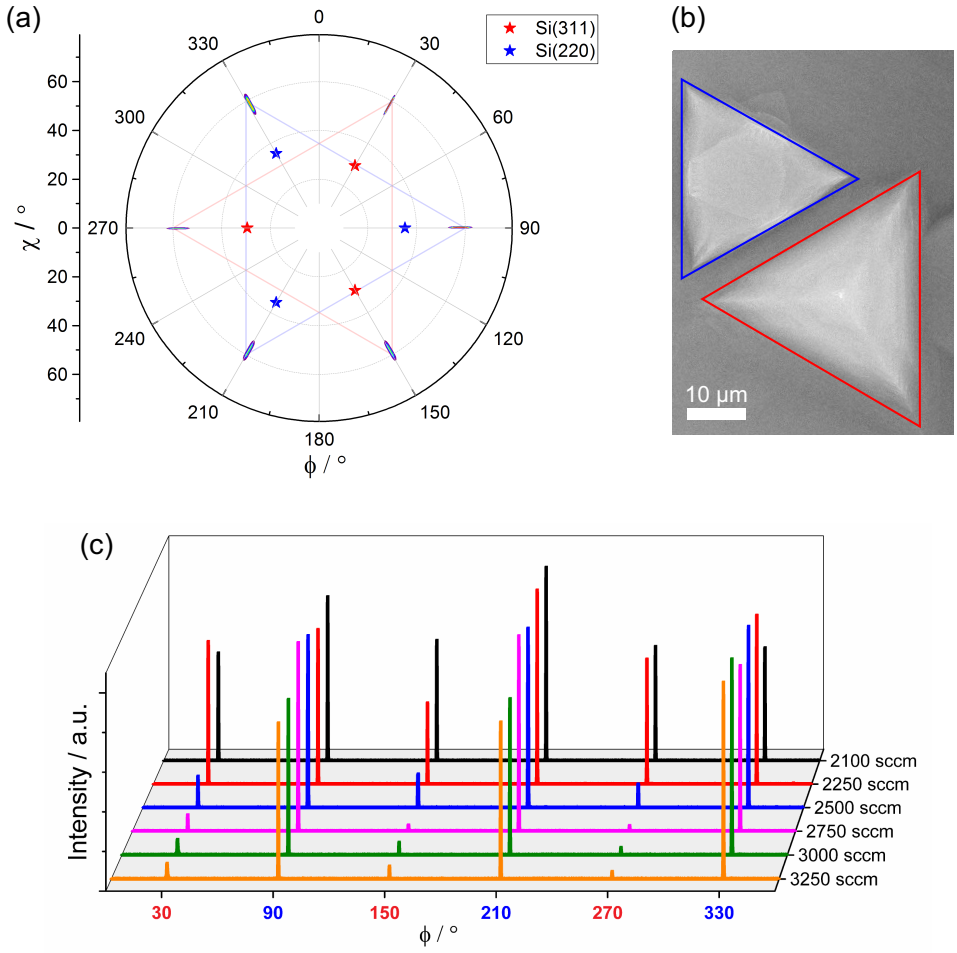

Figure 4.9: XRD ϕ-scan measurements showing presence of rotational twin domains in $Ge_1Sb_2Te_4$ layers grow with different TGF values: (a) pole figure measured around the (107) reflection of $Ge_1Sb_2Te_4$ for the sample grown under the flow of 2250 sccm – red and blue lines connect the reflexes from the same domains collinear to Si(311) and Si(220), respectively; (b) SEM image of the same sample with marked triangular islands corresponding to opposite rotational twin domains; and (c) ϕ-scans for all samples from the TGF series – one of the rotational twin domains gets strongly suppressed at higher TGF values. Red and blue color code of x-axis labels denotes collinearity of GST reflexes to Si(311) and Si(220) reflections, respectively.

layer. Therefore, extensive XRD characterization for all samples form the TGF series was carried out. The XRD 2θ-θ scan does not reveal a compositional differences between the samples, the diffractograms of all layers correspond to composition of $Ge_1Sb_2Te_4$ crystal [similar as in the case of pre-annealing atmosphere series, Fig. 4.6 (a)]. The difference, as one could expect, appears in the measured pole figures and ϕ-scans shown in Fig. 4.9. Pole figure measured around the (107) reflection of $Ge_1Sb_2Te_4$ reveals the sixfold symmetry of deposited layers, see Fig. 4.9 (a), which is a clear evidence for the presence of rotational twin domains. Reflexes corresponding to the same domain are connected with red and blue lines in Fig. 4.9 (a). One of the domain is collinear with Si(311) reflections, while another

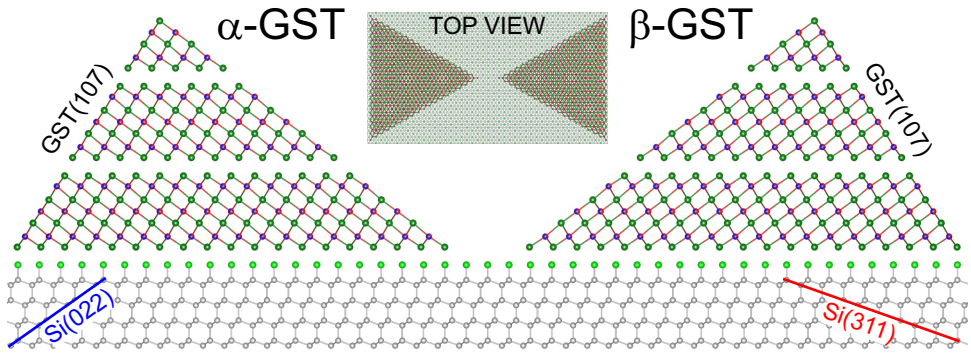

Figure 4.10: Model of $Ge_1Sb_2Te_4$ rotational twin domains on Si(111) substrate – projection along $[0\bar{1}1]_{Si}$ direction. Red and blue lines mark the Si(311) and Si(022) crystallographic planes, respectively. The (107) planes of $Ge_1Sb_2Te_4$ are also designated in the picture revealing collinearity to adequate Si planes. Contrary $Ge_1Sb_2Te_4$ domains are denoted as α-GST and β-GST. Inset in the middle of the image shows the top view of the model – along $[111]_{Si}$ direction.

one is collinear with Si(220) reflections. In the pole figure, Si(311) and Si(220) reflexes are marked with red and blue stars, respectively. The arrangement of opposite $Ge_1Sb_2Te_4$ twin domains on a Si(111) substrate is modeled in Fig. 4.10. In the figure, Si(311) and Si(022) crystallographic planes are marked with red and blue lines, respectively. Due to symmetry the Si(022) plane is equivalent to the Si(220) plane. Two opposite domains of $Ge_1Sb_2Te_4$ with marked (107) planes are situated on the Si surface. The top view inset reveals 60° rotation of the domains. The contrary domains are also shown, and marked with red and blue triangles, in SEM image in Fig. 4.9 (b). Note that the coloration in the SEM picture is symbolic and does not refer directly to the color code used in XRD pole figure. The $Ge_1Sb_2Te_4$ domain collinear with Si(220) reflections is called in this thesis α-GST, and the one collinear with Si(311) reflections – β-GST.

To better depict how the formation of rotational twin domains depends on the value of TGF during deposition, single line ϕ-scans were measured for each sample. The results of the measurements are shown in Fig. 4.9 (c), where red labels on the graph x-axis mark the position of the Si(311) reflections and blue labels correspond to the Si(220) reflections. It is visible that one of the domains gets strongly suppressed with the increase of the TGF value. The remaining domain is found to be collinear with the Si(220) reflections. Since the intensity of recorded reflexes is proportional to the volume of the corresponding domain in the characterized crystal, the fraction of the domain in the layer can be estimated based on the average intensity of observed reflections. Therefore, the fraction of β-GST domain in grown layers can be calculated as the ratio

$$\frac{\beta}{\alpha+\beta} = \frac{\bar{I}_\beta}{\bar{I}_\alpha + \bar{I}_\beta}, \tag{4.1}$$

where $\bar{I}_{\alpha/\beta}$ denotes the arithmetic mean of intensities measured for reflections correspond-

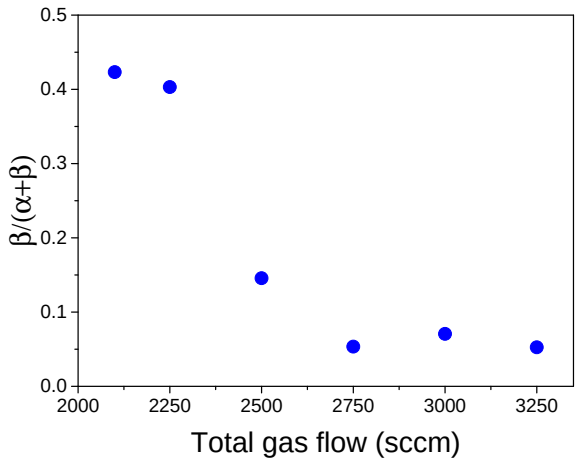

Figure 4.11: The fraction of β-GST domain in $Ge_1Sb_2Te_4$ layers grown with various TGF values in the reactor. Estimated basing on the averaged intensities of reflexes recorded in XRD ϕ-scans, presented in Fig. 4.10 (c).

ing to α/β-GST. The fraction of the β-GST domain for layers grown with various TGF values in the reactor is plotted in Fig. 4.11. The graph illustrates a strong suppression of the domain, for an increase of the TGF value from 2100 sccm to 2750 sccm. Later, the incorporation of the β-GST domain in the layer is kept at the level of ∼5%. The TGF range where the domain gets suppressed is identical to the range where pronounced improvements of surface morphology and reduction of the RMS roughness were observed (see Fig. 4.7 and Fig. 4.8).

At this point, the question about the reason for the improvements of layer characteristics with increase of the TGF arises. Analogous behavior has been reported for MBE-grown chalcogenides [94, 95], where the reason for the suppression of twinning was a reduction of the growth rate. Therefore, the growth rates were estimated for all samples from the TGF series using *in situ* time-resolved reflectance. The measured signal was fitted using LayTec software and the growth rates were extracted from the fitting curves. The values of $n = 6.51$ and $\kappa = 4.16$ were taken for fitting as refractive index and extinction coefficient of $Ge_1Sb_2Te_4$ at used during measurement wavelength of 1127 nm [19].

Fig. 4.12 (a) compares normalized detector signal recorded during the growth run of each sample from the series. For all samples, the reflected signal intensity increases until it reaches the maximum value. The lower the TGF value during the deposition, the higher the slope of the time-resolved signal in the region before the extrema point. This is already an indication that the growth is faster for lower flows in the reactor. After reaching the maximum, the signal decreases until the end of the growth or rather stabilizes at certain level in the case of higher TGFs. Fabry-Pérot oscillations are repressed due to absorption, however the intensity of the signal carries information about the surface roughness. Rough surface scatters incident light and causes losses in the signal, therefore detected intensity is reduced. The reduction of detector signal is stronger for the samples

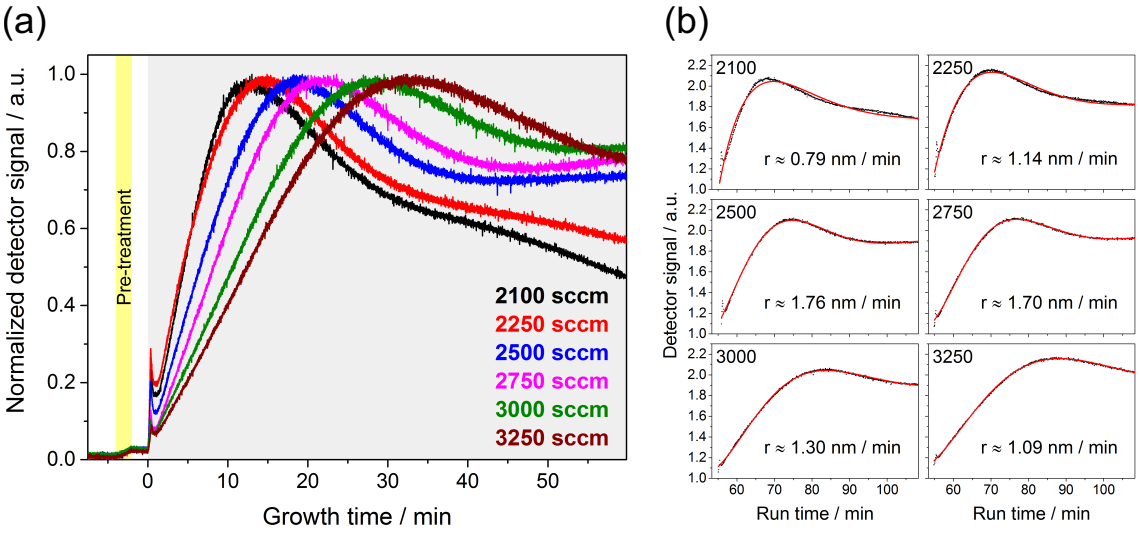

Figure 4.12: *In situ* time-resolved reflectance for $Ge_1Sb_2Te_4$ layers grown with various TGF values: (a) comparison of normalized signals; and (b) fitting curves (red) of measured signals (black dots) – numbers in the top left corners of the graphs indicate corresponding TGF values in sccm. The values of extracted growth rates are also inserted in the charts.

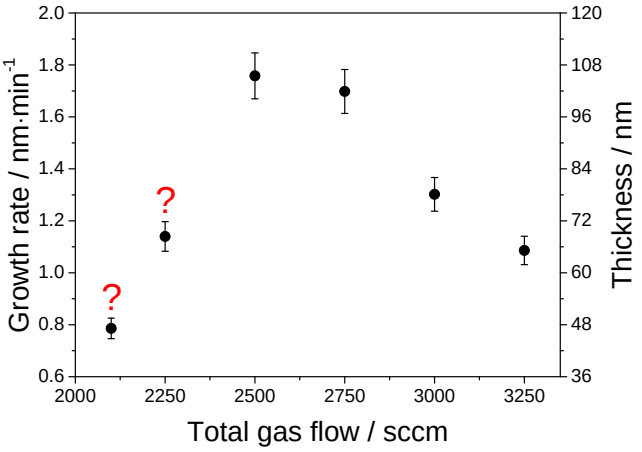

Figure 4.13: Growth rates extracted from *in situ* time-resolve reflectance measurement for samples deposited with various TGF values. The values marked with question marks are most likely artificially lowered due to a high roughness of the sample surface and the loss of the optical signal.

grown with lower TGFs, suggesting higher surface roughness for these specimens. Again, this observation is in perfect correlation with the findings from reported earlier in this section AFM measurements.

The fitting curves for each of the *in situ* recorded time-resolved reflectance signals are shown in Fig. 4.12 (b). Also, extracted growth rates are given as insets. For better representation and comparison the growth rates are plotted in Fig. 4.13. Calculated values of growth rate for the samples grown with the TGF value of 2100 sccm and 2250 sccm are lower and exhibit contrary trend than the rest of the samples – the rate is increasing

in this region. These values are most likely artificially lowered due to a high roughness of the sample surface and the loss of the optical signal during *in situ* measurement. A close look at the regression curves shown in Fig. 4.12 (b) reveals deviation from the signal and imperfection of the fitting for two first samples. For specimens grown with the TGF value of 2500 sccm and more the fitting curves match the signal well and the tendency is consistent – the growth rate decreases with the increase of the gas velocity in the reactor. The analysis of the *in situ* recorded reflectance indicates that the observed suppression of crystal twinning is really connected with the reduction of the growth rate and suggests that the growth take place in the kinetic-controlled regime.

Decomposition of precursors

In order to verify the experimental conclusion that the growth is kinetically controlled, the fraction of precursors decomposed in the gas-phase was calculated as a function of growth temperature using Eq. 3.18. The precursors decompositions were assumed to be the first order reactions with temperature dependence of the reaction rate constant described by the Arrhenius equation, Eq. 3.7, and parameters given in Tab. 3.2. The position of wafer on the susceptor in MOVPE 1119 system equals $x_{sub} = 75$ mm. The real volumetric flow and gas velocity in the reactor were calculated according to the Eq. 3.17 and Eq. 3.13. The results of calculations for the TGF value of 3000 sccm are presented in Fig. 4.14. As can be seen in the figure, according to the calculations Ge_2H_6 is fully decomposed already at temperature of ∼360 °C. However, one has to remember that the temperature of the gas in the reactor is not uniform, and decreases with the hight over the susceptor. The gradient of the temperature in the reactor also depends on the gas velocity. Therefore, part of the Ge_2H_6 molecules can be cracked on the sample surface. Pyrolysis of Ge_2H_6 on the surface will produce hydrogen, which can influence the decomposition of MO molecules. TESb and

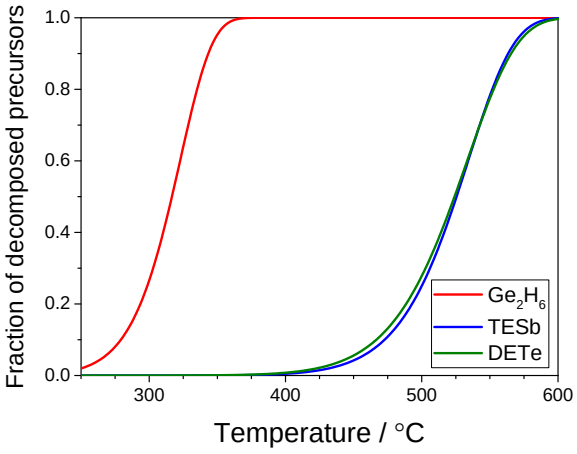

Figure 4.14: Fraction of decomposed precursors versus the susceptor temperature in MOVPE 1119. Calculated for the TGF value of 3000 sccm, at the position of the wafer front edge.

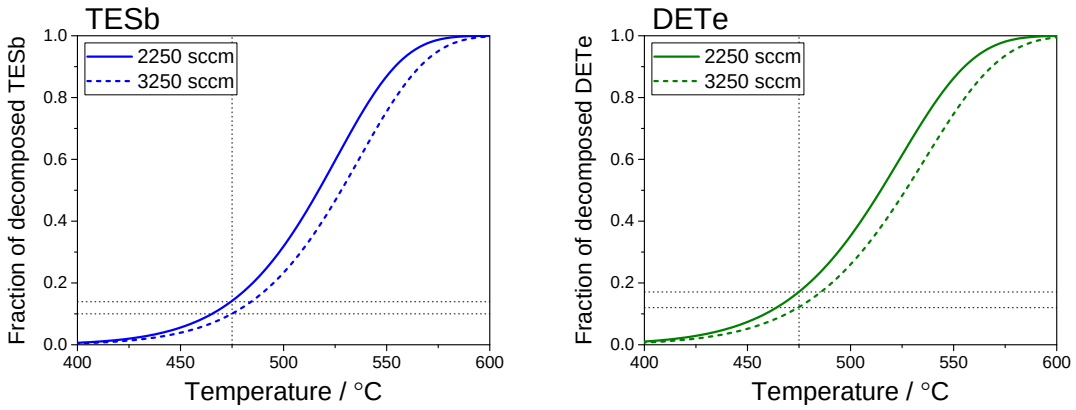

Figure 4.15: Influence of the TGF value on the fraction of decomposed TESb and DETe. Short-dashed lines mark the values for the growth temperature of 475 °C.

DETe seem to be entirely decomposed only at a temperatures near to and above 600 °C. At usual growth temperatures used in this work for GST alloys, around 475 °C, only a fraction of about 10-20% of precursor molecules undergoes pyrolysis. The calculations suggest that the growth of GST alloys at considered deposition temperatures is affected by gas-phase reaction kinetics. The problem is more clearly revealed when taking into account the fraction of decomposed precursors in dependence on the growth temperature for different TGF values in the reactor. Fig. 4.15 shows results of such calculations, where the fraction of decomposed TESb and DETe is calculated for the flow of 2250 sccm and 3250 sccm. At the growth temperature of 475 °C, the change of decomposition fraction for TESb and DETe between the flow of 2250 sccm and 3250 sccm approximately equals 4-5%.

Adequate calculations were done for all flows used for the deposition of GST. Obtained values were then normalized to the value for flow of 2500 sccm and then plotted together with the thicknesses of the grown layers, also normalized to the thickness of the layer grown with the TGF of 2500 sccm. The graph is displayed in Fig. 4.16. The change in the decomposed fraction of TESb and DETe is nearly identical, both dependencies decrease with the rise of TGF value and the lines cover each other in chart scale. However, *in situ* measured growth rate decreases faster than calculated fractions of decomposed precursors. While the growth rate for the TGF value of 3250 sccm drops to $\sim$ 62% of the value measured for 2500 sccm, the decomposition fraction is reduced only to the level of $\sim$ 78%, for both precursors. There could be few reasons for this inconsistency. On the one hand, for higher values of TGF the gas phase stays cooler and the reaction rate is reduced, but for calculations uniform temperature in the whole volume of the reactor was assumed. On the other hand, the assumption that the thermolysis of DETe is the first order reaction, does not clearly reflect the reality, since the pyrolysis of DETe is an autocatalytic reaction [74], see Fig. 3.9. Thus, the process can additionally slow down by itself, if the amount of reaction products is limited by an external factor. This could explain the observed deviation and stronger reduction of the growth rate. Moreover, the

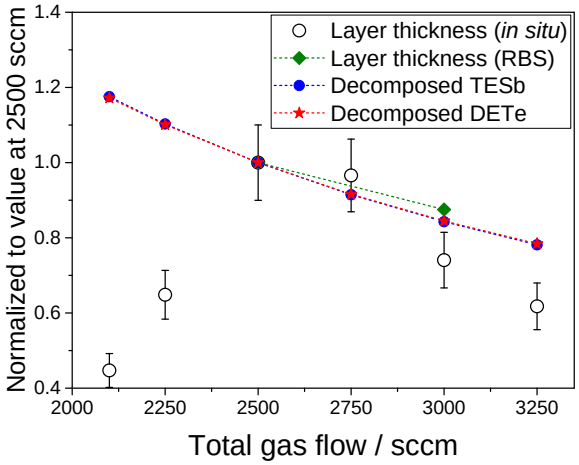

Figure 4.16: Calculated fraction of decomposed precursors compared to the thicknesses of $Ge_1Sb_2Te_4$ layers grown with various TGFs. All values are normalized to the corresponding value at 2500 sccm. The thickness was extracted from *in situ* reflectance and RBS measurements.

observed inconsistency can simply be an imperfection of the measurement method. First of all, the result is affected by the absorption, which lowers the accuracy, as discussed in subsection 3.2.1. Second, the incident and reflected beams pass through the glass window in the reactor wall. A dust particle or more likely parasitic deposition can reduce the window transparency and disturb the detected signal, which would influence the result of measurement.

The thickness of the chosen samples was also estimated using RBS. The values of 120 nm and 105 nm were obtained for specimens grown under the flow of 2500 sccm and 3000 sccm, respectively. The outcome implies the reduction of the growth rate to 87.5% (comparing the sample grown with 3000 sccm to the one grown with 2500 sccm, marked in Fig. 4.16 with green diamonds). For the same value of TGFs, calculated fraction of the decomposed precursors drops to $\sim 84\%$, and *in situ* measured growth rate to $\sim 74\%$. Hence, RBS results seems to be more consistent with the calculated values, which suggests that the inconsistency with *in situ* results is due to a low accuracy of the experimental method. All in all, the experiments and computations clearly indicate that the growth of GST proceeds in the kinetic-controlled regime.

Growth rate controlled with partial pressures

A series of samples with varied partial pressures of all precursors was prepared to resolve experimentally the influence of the growth rate on the formation of rotational twin domains. The starting point for the experiment was reference sample grown with the TGF value of 3000 sccm and standard partial pressures reported in Tab. 4.1. Next, two samples with lowered and three samples with raised partial pressures of precursors were grown. The partial pressures of precursors directly affects the growth rate, as indicated by Eq. 3.5

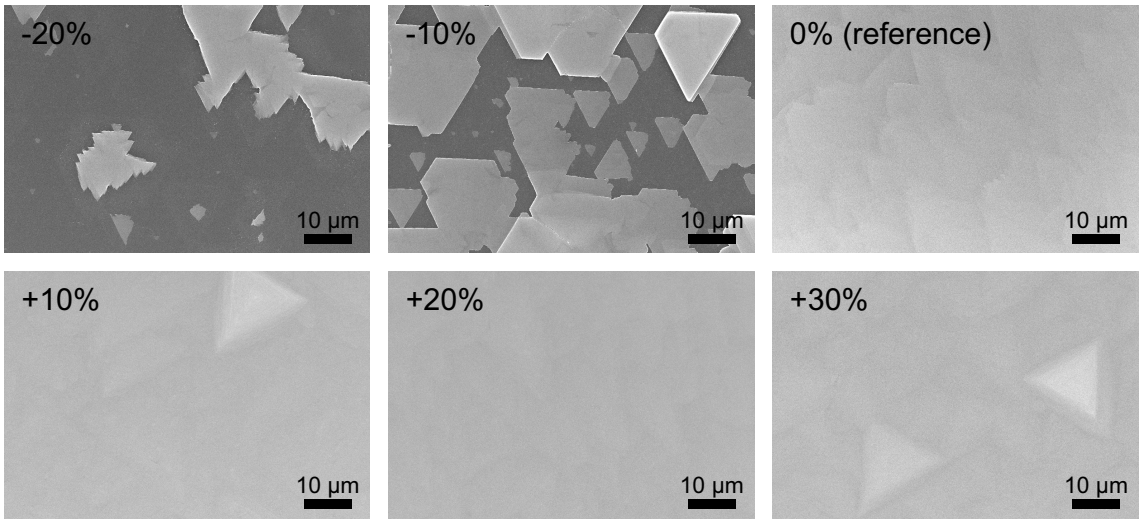

Figure 4.17: SEM images of samples grown with various partial pressures of precursors. The change of partial pressures in relation to the reference sample is indicated in each micrograph. The ratio of precursors partial pressures was identical for all samples.

and Eq. 3.19. The values of partial pressures were changed in 10% steps and were the only growth parameter varied in the series. The ratio of precursors partial pressures was kept identical for all samples.

As can be seen in SEM micrographs of the samples shown in Fig. 4.17, when the partial pressures are reduced insufficient amount of material is conveyed to the substrate surface to form a coalesced layer. While increasing the partial pressures of precursors, the sample morphology does not change significantly, albeit triangular islands are present in the images taken for samples grown with 10% and 30% higher partial pressures.

Although the effect of higher partial pressures on the layer appearance is unnoticeable, the change leads to enhanced formation of β-GST domain in $Ge_1Sb_2Te_4$ films. The dependence is presented in Fig. 4.18 where the incorporation of the β-GST domain in the grown layer is estimated from XRD ϕ-scans, as previously, for the samples grown with various TGF. It is clearly visible that the fraction of β-GST increases for partial pressures higher than values used for the reference sample. While the partial pressures are reduced below the reference values, the ratio $\beta/(\alpha+\beta)$ does not change. Aside from proving that the suppression of crystal twinning in MOVPE-grown $Ge_1Sb_2Te_4$ layers is caused by the reduction of the growth rate, the experiment helps to chose appropriate partial pressures for deposition of GST alloys, those depicted in Tab. 4.1. For lower partial pressures, the epitaxy results in a growth of triangular islands, however highly oriented with one dominating domain. For higher values of partial pressures, the growth of fully coalesced films is achieved, but with two opposite rotational twin domains in the layer. Choosing the right partial pressures ensure the deposition of a fully coalesced $Ge_1Sb_2Te_4$ layer with one dominating domain.

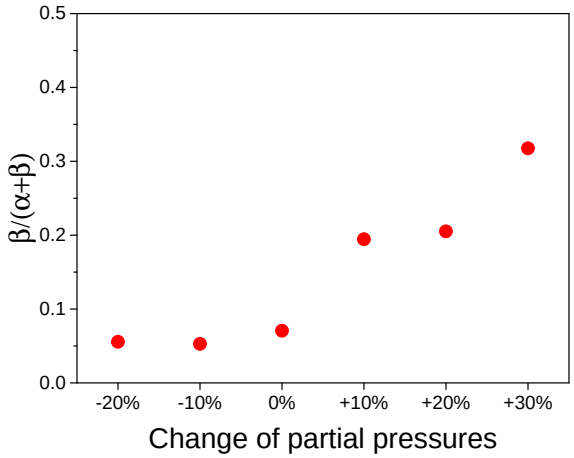

Figure 4.18: The fraction of the β-GST domain in $Ge_1Sb_2Te_4$ layers grown with various partial pressures of precursors (constant ratio). Estimation based on the average intensity of reflexes in XRD ϕ-scans. The reference sample, being the starting point of the experiment, is the one denoted by partial pressures change of 0%.

4.1.3 Growth temperature

The last growth parameter which influence on the deposition of GST alloys was investigated is the substrate temperature. As earlier, the samples were grown for 60 min, using partial pressures of precursors listed in Tab. 4.1, after 30 min annealing in H_2 atmosphere and 2 min Ge_2H_6-TESb substrate pretreatment. The TGF value of 3000 sccm was utilized during epitaxies. The growth temperature was changed from 465 °C to 485 °C with 5 °C step.

Samples described earlier in this chapter were grown at 475 °C, therefore this temperature is treated here as a reference point. The growth temperature has a slight effect on the morphology of the sample, as can be seen in SEM micrographs presented in Fig. 4.19. No explicit change in the sample surface is visible for layers deposited at higher temperatures, from 475 °C to 485 °C. All growths result in fully coalesced films with fish scale texture. More pronounced impact is noticeable when the temperature is decreased. Reduction of the temperature to 465 °C leads to the formation of openings in the layer and a diminishing of the coalescence. The reason for this is the reduced fraction of decomposed TESb and DETe molecules, according to the dependences revealed in Fig. 4.14 and Fig. 4.15. Diminished precursor decomposition limits the amount of materials contributing to the growth and results in a not fully covered substrate. It is another indication that the growth of GST alloys proceeds in the kinetic-controlled regime.

As indicated in Fig. 4.14, only the amount of decomposed TESb and DETe changes with temperature in the investigated range. Digermane should be fully decomposed at this region. Therefore, the ratio between particular elements participating in the growth changes with the substrate temperature. It is expected that the increase in the growth temperature will affect the composition of the deposited layer, shifting it towards lower

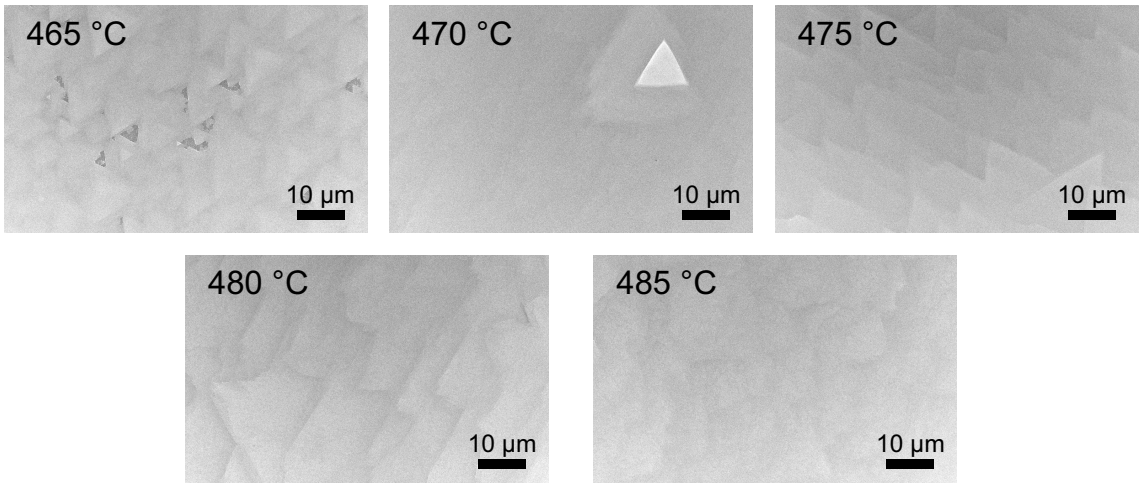

Figure 4.19: SEM images of GST samples deposited at different substrate temperatures, indicated in the micrographs. Other growth parameters were identical for all samples in the series.

Ge content. The prediction is confirmed by XRD 2θ-θ and EDX compositional analysis.

The XRD 2θ-θ diffractograms measured in the range of 5-50° for samples grown with various temperatures are depicted in Fig. 4.20. Recognized reflections are described in the image. For the lowest applied temperature of 465 °C, only reflections connected with $Ge_2Sb_2Te_5$ composition are found, which is equivalent to a pseudo-binary alloy of $(GeTe)_2(Sb_2Te_3)_1$. An increase of the temperature just by 5 °C results in the deposition of $Ge_1Sb_2Te_4$, $(GeTe)_1(Sb_2Te_3)_1$ alloy. No compositional difference is resolved with the 2θ-θ scans between samples grown at the temperatures of 470-480 °C. At the highest growth temperature of 485 °C, the grown layer is found to be a mixture of $Ge_1Sb_2Te_4$, $Ge_1Sb_4Te_7$ [equivalent to $(GeTe)_1(Sb_2Te_3)_2$], and Sb_2Te_3. It is evident, while the growth temperature is increased the incorporation of Sb_2Te_3 into the grown layer increases, which is equivalent to a reduced Ge content, as predicted.

The XRD 2θ-θ characterization was not able to resolve the compositional contrast between samples grown at 470 °C, 475 °C, and 480 °C. However, the difference is exposed in the EDX analysis of the samples, represented in Fig. 4.21. The EDX results are consistent with the XRD characterization. It is clearly visible in the chart that the Ge content in the layer is reduced with the increase of the temperature. As indicated by the 2θ-θ scans, also EDX shows that the composition of material deposited at 465 °C is close to $Ge_2Sb_2Te_5$ – ratio of atomic percentage for Ge and Sb that is close to one. The composition of the grown alloys gradually shifts with the temperature towards higher Sb_2Te_3 content, at 485 °C reaching the stoichiometry of $Ge_{1.00}Sb_{3.18}Te_{5.16}$. It agrees with the XRD analysis where a higher Sb_2Te_3 content was measured for the samples grown at higher temperatures. The statistical material compositions extracted from EDX measurements for the samples grown at various temperatures are listed in Tab. 4.4.

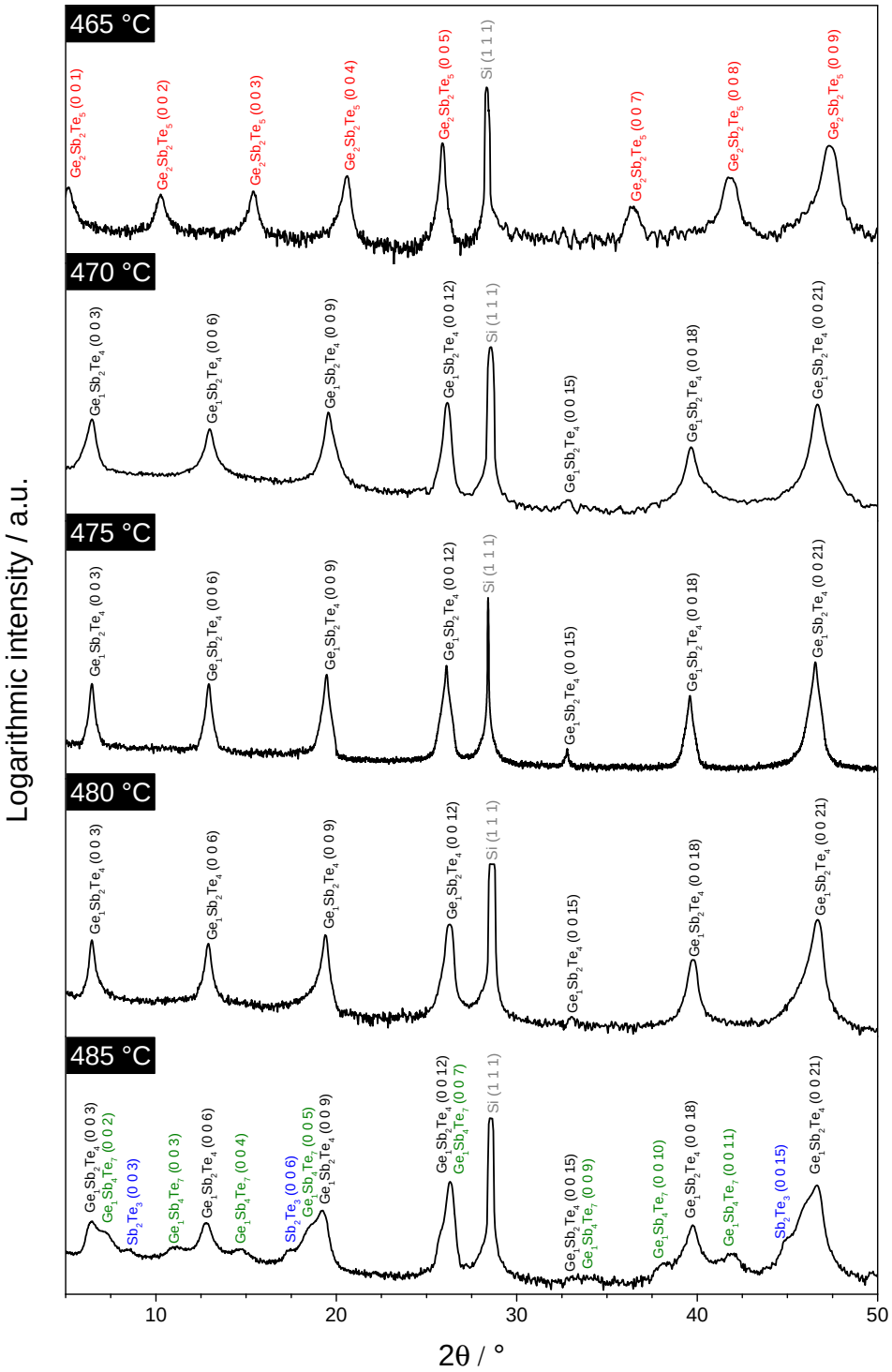

Figure 4.20: XRD 2θ-θ diffractograms measured for GST samples grown at various temperatures (indicated in black labels on the left-hand side). All recognized reflections are signed in the chart.

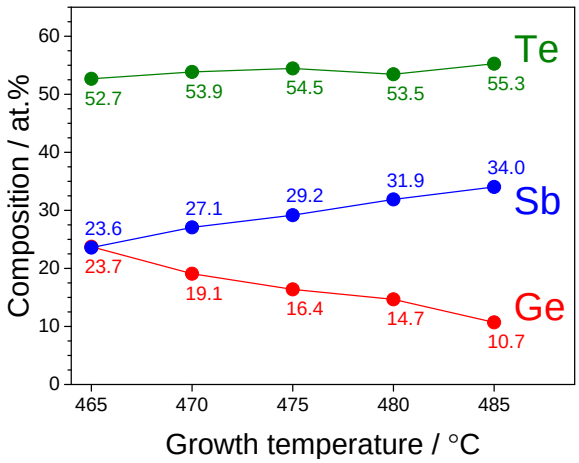

Figure 4.21: EDX compositional analysis of GST samples grown at various temperatures. The values next to points in the graph indicate atomic percentage content for each of the elements.

Table 4.4: Extracted from EDX measurements composition of GST alloys deposited at various temperatures.

Growth temperature / °C	Composition
465	$Ge_{2.00}Sb_{1.99}Te_{4.44}$
470	$Ge_{1.00}Sb_{1.42}Te_{2.82}$
475	$Ge_{1.00}Sb_{1.78}Te_{3.32}$
480	$Ge_{1.00}Sb_{2.17}Te_{3.65}$
485	$Ge_{1.00}Sb_{3.18}Te_{5.16}$

4.2 Modeling of Ge-Sb-Te twin domains

In subsection 4.1.2, the influence of TGF in the reactor on the deposited GST layer characteristics is reported. The reduction of the growth rate is observed when the flow is increased, which leads to a suppression of one rotational twin domain. It has also been mentioned that the suppression of twin domains has been observed in MBE-deposited chalcogenides [94, 95]. However, the reflexes of the dominating domain in MBE-grown materials are collinear with Si(311) reflections, which is contradictory with the tendency found for MOVPE-grown $Ge_1Sb_2Te_4$, where predominant domain shows collinearity with Si(220) reflections. Kampmeier et al. [94] proposed a simple model explaining the tendency of chalcogenides (Bi_2Te_3 in their case) grown on Si(111) substrate to form domains collinear with Si(311) reflections. They have shown that formation of this particular domain is energetically more favorable than the creation of the domain with reflexes collinear to Si(220) reflections. In their model, the triangular networks of Te atoms on Te-passivated

Si(111) surface are considered as a building blocks for the layer. The energy of such an island is computed as the sum of local vdW potentials for each Te atom from the network, approximated with

$$E_{vdW} \approx -\frac{C}{r^6}, \tag{4.2}$$

where C is a constant dependent on interacting atoms, and r is the distance between them. It is assumed that $C = 1$ regardless of interacting elements, so all atoms are treated equally and are indistinguishable. The model considers only interactions of Te atoms from the triangular island with four nearest Si substrate atoms and one nearest Te atom from the passivation layer.

4.2.1 Model

Based on the model of Kampmeier et al. [94], a more accurate approach is proposed in this thesis. Atoms are still treated as interacting indistinguishable points, i.e., the constant $C = 1$ in the Eq. 4.2, with the exception of having a cut-off radius for the vdW interaction rather than only taking the nearest neighbors into account, as done by Kampmeier et al. The cut-off radius defines the maximal distance between two atoms, which interaction energy contributes into computation of the total energy. Interactions between two elements separated by a distance larger than the cut-off radius are ignored and assumed to be zero. Naturally, the larger is the value of cut-off radius, the higher is the precision of calculations, but simultaneously more computational power and time is required.

Second change introduced to the model concerns the building blocks of the layer. Kampmeier et al. [94] assumed that an atomic layer of Te atoms is nucleation seed for the film of deposited material and determines the orientation (domain) of grown crystal in relation to the substrate structure. It is debatable whether this assumption is too simple. While it is possible to point out structural differences between two 60°-rotated triangular atomic layers on Si(111) substrate, in reality the difference and the island orientation are resolved by second layer of atoms (Ge/Sb in case of GST). Fig. 4.22 depicts the problem. Two bottom layers of contrary twins considered in conducted simulations are presented in shared reference system. It is easy to see that the bottommost Te layer is identical in

Figure 4.22: Two bottom atomic layers of GST film considered in calculations. Both configurations are energetically equivalent if they are not placed on Si(111) substrate. When they are places on a Si(111) substrate, they play as a starting point for opposite rotational twin domains. Green balls display Te atoms, and red/blue – Ge/Sb atoms.

both cases. What distinguishes the two cells is the second-layer Ge/Sb atom, which can occupy one of two possible positions: $(\frac{1}{3}, \frac{2}{3}, z)$ or $(\frac{2}{3}, \frac{1}{3}, z)$. Both positions are energetically equivalent with respect to the bottommost Te layer, due to symmetry, but they will create nucleation seeds for opposite domains, while placing the cells on Si(111) substrate, leading to formation of rotated by 60° triangular islands. The orientation of corresponding island is marked in Fig. 4.22 with turquoise triangles and shown in bigger scale in Fig. 4.10. The second atomic layer is essential for the identification of the twin domain and its correlation to Si(111) substrate. Therefore, in order to clearly distinguish between the two domains, at least two most bottom atomic layers of GST film should be taken into account when calculating the total energy of the system.

In the proposed model, the total energy for a twin domain is calculated as the sum of the local vdW potential energy for every atom of the GST twin. The local vdW potential for the twin atoms is computed as the sum of contributions from all substrate atoms that are closer to the twin atom than the defined cut-off radius. Hence, the total potential energy of a twin can be written as

$$E_{tot} = \sum_{n=1}^{n_{twin}} \sum_{k=1}^{k_{sub}} E_{n,k}, \tag{4.3}$$

where n_{twin} and k_{sub} are the total number of atoms of the simulated twin and the substrate, respectively. $E_{n,k}$ is the potential energy between the n-th atom of the twin and the k-th atom of the substrate, approximated with the vdW potential (Eq. 4.2) according to the formula

$$E_{n,k} = \begin{cases} -\dfrac{1}{|r_n - r_k|^6} & \text{for } |r_n - r_k| \leqslant r_{cut} \\ 0 & \text{for } |r_n - r_k| > r_{cut} \end{cases}, \tag{4.4}$$

r_n and r_k denote the position of the n-th atom of twin and the k-th atom of substrate, respectively. Parameter r_{cut} represents the cut-off radius.

The twins are simulated as triangular two-atomic-layers islands of Te and Ge/Sb atoms, which are considered to be nucleation seeds for $Ge_1Sb_2Te_4$ film. The in-plane lattice constant of $Ge_1Sb_2Te_4$ is $a_{GST} = 4.26$ Å, as indicated by XRD measurements shown in Fig. 4.6, and the Si(111) in-plane lattice constant is calculated to be $a_{Si(111)} = 5.43053\ \text{Å}/\sqrt{2} \approx 3.84$ Å [75]. Therefore, to meet the symmetry conditions, the islands representing GST twins are simulated as triangles with nine $Ge_1Sb_2Te_4$ unit cells on the edges, since

$$9 \cdot a_{GST} \approx 10 \cdot a_{Si(111)}. \tag{4.5}$$

Considered structures are presented in Fig. 4.23, where triangular networks of atoms (Te, Sb, Ge) representing nucleation seeds of α-GST [collinearity with Si(220) reflections] and β-GST domain [collinearity with Si(311) reflections] are marked with red and magenta dots, respectively. Blue rings denote Si atoms and green dots show Te atoms of the passi-

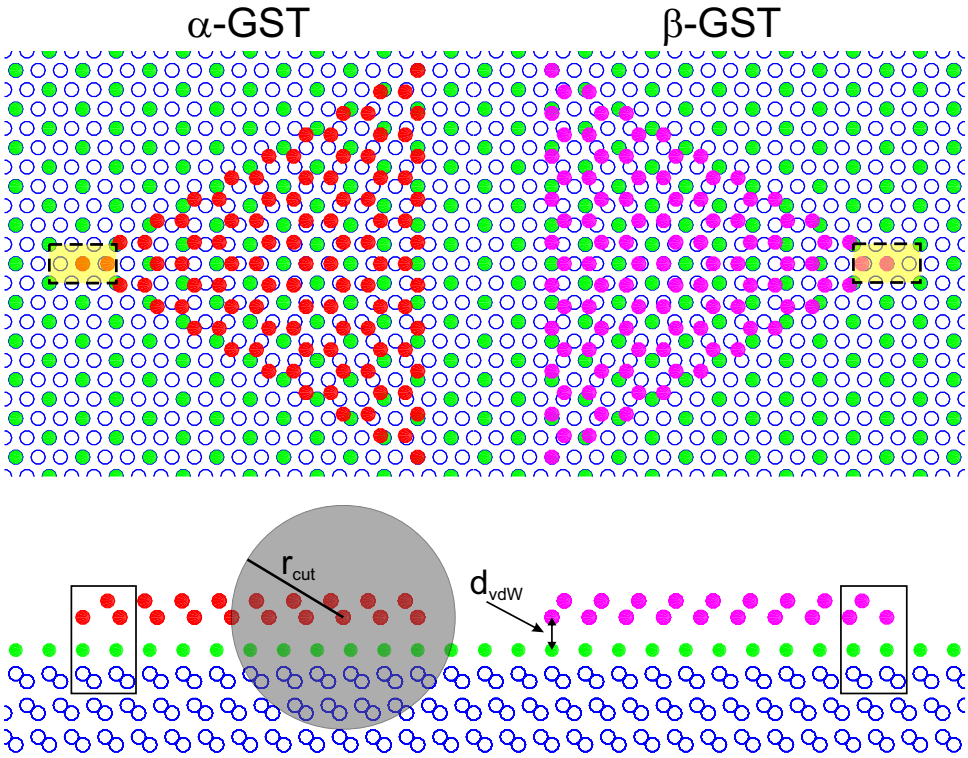

Figure 4.23: Top and side view of simulated islands representing opposite twin domains. Blue rings mark Si atoms, green points – Te atoms, and red and magenta points – atoms of contrary twin domains. Shadowed circle illustrates the concept of the cut-off radius. Only the influence of substrate atoms lying inside of the circle is taken into consideration when calculating the potential energy for the twin atom in the center of the circle. d_{vdW} denotes vdW gap between Te-passivation layer and GST film. Two unfilled rectangles in the bottom part of the figure on the left- and the right-hand side point out the configuration difference between the twins. Dashed-line rectangles with pastel yellow filling (top view) mark the regions within which the tip of each twin domain was moved around in order to find energetically optimal place for the island.

vation layer. Because of the covalent bonds between the Si surface atoms and the Te atoms of the wetting layer, the Te atoms adopt the same in-plane constant as the Si substrate, and hence the bond length between Si and Te atom from wetting layer is assumed to be the same as the length of the Si-Si bond. Although the model does not discern between the elements, colors are used in the picture and assigned to specific atoms for a better visualization and simplification. Fig. 4.23 also illustrates the idea of cut-off radius, which is marked there with shadowed circle. While the total potential energy for the atom placed in the center of the circle is computed, only interactions with substrate atoms (including Te-passivation) lying inside the circle are taken into account. Further, the bottom picture marks with two rectangular frames the difference in the configuration of the atoms, which makes the twins distinguishable. The vdW gap between the Te-passivated Si(111) substrate and GST film is also sign as d_{vdW}. The vdW gap dimension was determined

based on intensity profile extracted from HAADF-STEM micrograph, shown in Fig. 4.3. The value was measured as the difference between the center of the peak corresponding to Te-wetting layer and the center of the peak connected with first bottom Te layer of GST film. The distance amounts to 3.25 Å and it is assumed constant for the calculations. Other value taken from HAADF-STEM images was the distance between two atomic layers considered in modeled GST twin structures. The distance was determined in the same manner as the vdW gap. The value of 1.63 Å was obtained and employed in the simulations.

4.2.2 Cut-off radius

The aim of the computations is to find energetically preferred GST crystal domain on the Si(111) substrate. To this end, first the influence of the cut-off radius on the calculation results was studied. Proper choice of the cut-off radius is a compromise between the precision of simulations and computation time, which depends on available computing power. To find optimal value for the cut-off radius, the system presented in Fig. 4.23 was simulated for the cut-off distances between 4 Å and 30 Å. For each of the values, its impact on the calculated energies of twins was evaluated as the relative change of the energy with respect to the result obtained from the previously used cut-off conditions. The formula was applied

$$\Delta E_{tot}(r_{cut,i}) = \frac{E_{tot,i} - E_{tot,i-1}}{E_{tot,i-1}} \cdot 100\%, \tag{4.6}$$

where E_{tot} represents calculated twin potential energy, and i indexes tested values of cut-off radius r_{cut}. The change of the computed twin energies on increasing cut-off radii is plotted in Fig. 4.24 (a). The accuracy of the simulation increases with each subsequent increase of the cut-off distance. Exceeding the radius length over 28 Å changes the energies of twins by less than 0.5‰. Fig. 4.24 (b) shows how the cut-off length influences the energy difference

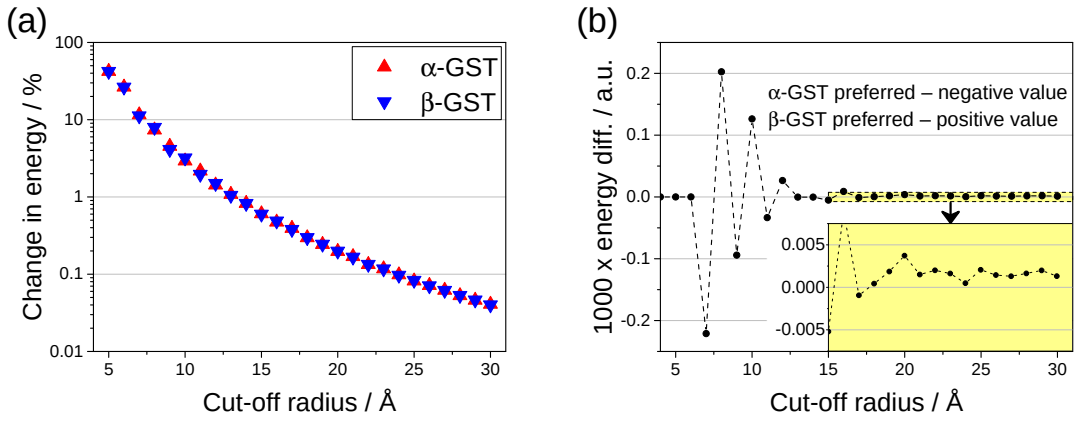

Figure 4.24: Studies of the cut-off radius influence on the total potential energy of the simulated GST twin domains: the change of the energy caused by the increase of the radius; and (b) the energy difference between twins in dependence on the radius length (inset zooms marked region of the graph).

between α-GST and β-GST twin, which indicates an energetically favored domain. The energy difference is calculated as

$$E_{diff} = E_{tot,\alpha} - E_{tot,\beta}. \tag{4.7}$$

Hence, the indicator takes positive value, if β-GST domain is energetically preferred, i.e., has lower total energy, and negative value, if α-GST is the more favorable configuration. For low values of the cut-off radius, the indicator is very sensitive for a change of the radius length and jumps between negative and positive values, giving opposite results for the same configuration of atoms. The model becomes less sensitive to the cut-off conditions with an increase of the radius. Calculated energy difference seems to stabilize and gives consistent results for cut-off distances larger than 18 Å. However, to keep the calculations at a very high degree of accuracy, the cut-off radius of 28 Å was used in further simulations.

4.2.3 Energetically favored domain

In order to resolve, which of twin domains is energetically more favorable, the total potential energy for both modeled twins was calculated in dependence on the twin position with respect to the Si(111) substrate. The twin coordinates were defined as the location of Te atom from the tip of the triangular island representing twin domain in the model. The position directly over an Te atom from passivation layer of Si surface was taken as the starting point with coordinates (0, 0). Next, the twin position was shifted in horizontal (x-shift) and vertical direction (y-shift) with the step of 0.1 Å within the region marked in Fig. 4.23 with dashed-line rectangles with pastel yellow filling. For every position, the total potential energy of each twin was calculated according to the procedure described earlier.

The results of the computations are presented as heat-map plots in Fig. 4.25. In the heat maps, in-plane positions of atoms from three top atomic layers of the substrate are marked with green and blue dots. Green points correspond to Te atoms of the passivation layer with the first layer of Si atoms underneath, and blue dots mark the second layer of Si atoms. The orientation of triangular islands is illustrated with red and magenta triangles next to the α-GST and β-GST labels, respectively. In such defined coordinates, α-GST twin exhibits the lowest energy for shift of −2.2 Å along x-axis, while β-GST twin takes the minimal energy for shift of 2.2 Å, also in x-direction. The general tendency of the change in potential energy is symmetrical for contrary twins, which is clearly revealed in Fig. 4.25. The minimal values of potential energies are calculated to be around −0.09025296 a.u. for α-GST and −0.09025159 a.u. for β-GST, which, according to the Eq. 4.7, results in negative energy difference of $-1.37 \cdot 10^{-6}$ a.u. The calculated difference indicates that the α-GST domain, with (107) reflexes collinear to Si(220) reflections, is the energetically preferred domain. The simulation result is in agreement with experimental data for MOVPE-grown $Ge_1Sb_2Te_4$ layers.

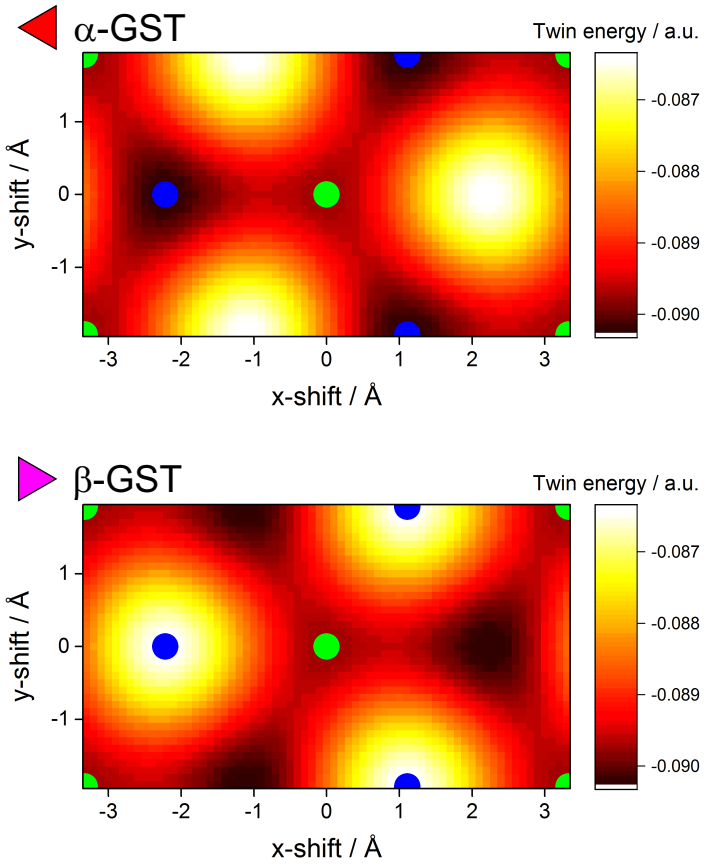

Figure 4.25: Total potential energy of simulated GST twin domains in dependence on position of the islands with respect to the Si(111) substrate. The position of the twin is defined as the coordinates of its tip atom. Red and magenta triangles next to the α-GST and β-GST labels indicate the orientation of GST island on Si surface. Green points mark the position of Te atoms of passivation layer with the first layer of Si atoms underneath, and blue dots correspond to Si atoms from the first layer underneath the Si surface layer.

The proposed model describing rotational twin domains of $Ge_1Sb_2Te_4$ on Si(111) substrate is in agreement with experimental observations for MOVPE materials. However, both experiment and simulation results are opposite to those reported by Kampmeier et al. [94] for MBE-grown Bi_2Te_3. There can be few reasons for this inconsistency. First, the model utilized in this thesis is more precise than model of Kampmeier et al. [94] and imitates the real world interactions better through the introduction of a cut-off condition. Second, the considered material system is different. Bi_2Te_3 hexagonal in-plane lattice constant is $a_{BT} = 4.38$ Å [97], which is larger then $Ge_1Sb_2Te_4$ in-plane lattice constant and results in different size of nucleation seed chosen for computations (seven unit cells on the edge of triangular island). However, the predominant domain in MBE-grown Sb_2Te_3 have been reported to be collinear with Si(311) too [95], although the lattice constant of the material is equal to the value of lattice constant used for reported here simulations. Nevertheless, it is worth to notice that the suppression of domain collinear with Si(220)

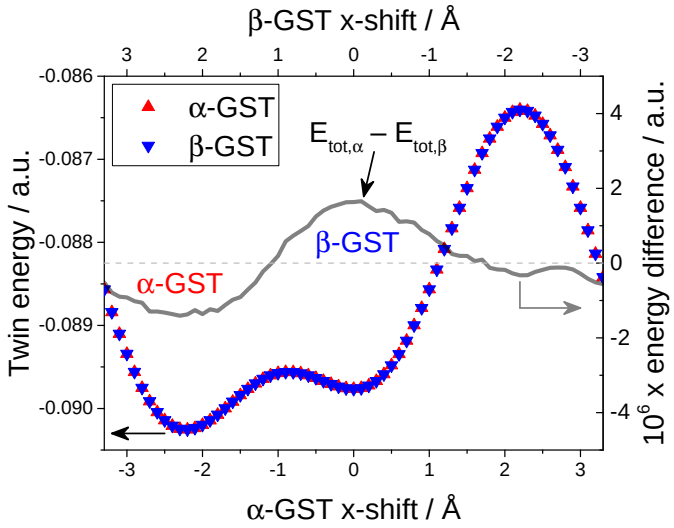

Figure 4.26: Potential energy of GST twin domains in dependence on shift of the islands in x-direction (along $y = 0$ line). Profiles extracted from Fig. 4.25. Note that the top axis, corresponding to β-GST, is reversed. The gray line plots the energy difference between the presented profiles and indicates the preferred twin domain at a given position.

reflections is not so pronounced in the case of MBE-grown Sb_2Te_3 as for Bi_2Te_3. Finally, the discrepancy between MOVPE- and MBE-deposited materials can be caused by different nucleation centers preferred in both methods. The change of optimal location for nucleation of crystal could be forced by different growth conditions, e.g., the substrate temperature. Fig. 4.26 shows twin potential energy profiles extracted from Fig. 4.25 along $y = 0$ line. Both profiles have the global minimum at x-shift of ± 2.2 Å and a local minimum at 0 Å. The local minimum can be interpreted as a metastable state. The important message is that at the global minimum α-GST is energetically favored domain, while at the local minimum β-GST if preferred, as indicated by the energy difference plotted with gray line in Fig. 4.26. It is a suggestion that the nucleation centers for chalcogenides differ in MOVPE- and MBE-grown samples. The metastable position could be more likely occupied in the case of MBE, due to lower growth temperatures used in the process.

The discussed and applied model is rather simple and does not give definitive explanation for observed experimentally tendency of chalcogenides to favor one of the twin domains. Despite its simplicity, the approach fits experimental results for MOVPE-deposited $Ge_1Sb_2Te_4$ and gives a possible explanation for the opposite tendency observed for MBE-grown materials.

4.3 Growth of Sb_2Te_3

The iPCMs are commonly deposited as $GeTe/Sb_2Te_3$ superlattices [3, 49], mainly via MBE or sputtering. However, MOVPE is an attractive alternative for the growth of superlattices due to its industrial relevance. In order to deposit a $GeTe/Sb_2Te_3$ superlattice, controlled

Table 4.5: The growth procedure and parameters used for the deposition of Sb_2Te_3. The impact of parameters written in dark red on the growth was examined in detail.

	Annealing	**Cooling**	**Pretreatment**	**Break**	**Growth**
t / min	28 + 2	6-11	2	2	40
Carrier gas	H_2	N_2			
Precursors	DETe	–	**Ge_2H_6, TESb**	–	***$R_{VI/V}$***
T / °C	690	decreases	**425-500**		
p / mbar	50				
TGF / sccm	2600-3000	2182-2200	2200-2600	2200	3000

and repeatable growth conditions for Sb_2Te_3 and GeTe have to be established.

The growth of Sb_2Te_3 by means of MOVPE has already been reported in the literature [65, 98, 99]. In this thesis, the growth of Sb_2Te_3 is explored with respect to the ratio of the precursors partial pressures $R_{VI/V}$, growth temperature and substrate pretreatment. The starting point for the research were the growth conditions set previously for $Ge_1Sb_2Te_4$ layers. Inspected samples were grown for 40 min on a quarter of 2 inch Si(111) wafer. The standard chemical cleaning procedure was applied to the substrate right before the deposition, as described in subsection 3.1.4. Prior to the epitaxy, the Si substrate was annealed for 30 min in H_2 atmosphere and in addition DETe was injected into the reactor in the last 2 min of the annealing. The temperature of this step was kept at 690 °C. Later, the temperature was reduced to the growth temperature and the substrate was pretreated with Ge_2H_6 and TESb for 2 min (however, this step was varied in series of sample examining the effect of the pretreatment). Finally, after a 2 min interruption in the precursors supply, the growth of Sb_2Te_3 was initiated. The TGF value was set to 3000 sccm and the total pressure in the reactor was 50 mbar – the values were identical for all of the samples. The details about the growth procedure are given in Tab. 4.5.

4.3.1 Partial pressures ratio

The optimization of the MOVPE growth conditions for Sb_2Te_3 started with the adjustment of the VI/V ratio $R_{VI/V}$, which is the ratio of DETe to TESb partial pressures. The first sample was deposited utilizing the partial pressures used for the growth of GST alloys, see Tab. 4.1, without Ge_2H_6. Further samples were grown with a gradual increase of the TESb partial pressure, while the amount of DETe injected into the reactor was kept constant. Information about investigated values of TESb partial pressures and VI/V ratios are given in Tab. 4.6. All samples in the series were grown at 475 °C.

Fig. 4.27 presents SEM pictures of Sb_2Te_3 samples grown on Si(111) substrate with

Table 4.6: Examined partial pressures of precursors and VI/V ratios used for deposition of Sb_2Te_3 samples.

Sample	p_{DETe} / mbar	p_{TESb} / mbar	$R_{VI/V}$
No. 1	$1.33 \cdot 10^{-1}$	$4.78 \cdot 10^{-3}$	27.7
No. 2		$1.19 \cdot 10^{-2}$	11.1
No. 3		$1.66 \cdot 10^{-2}$	8
No. 4		$2.21 \cdot 10^{-2}$	6

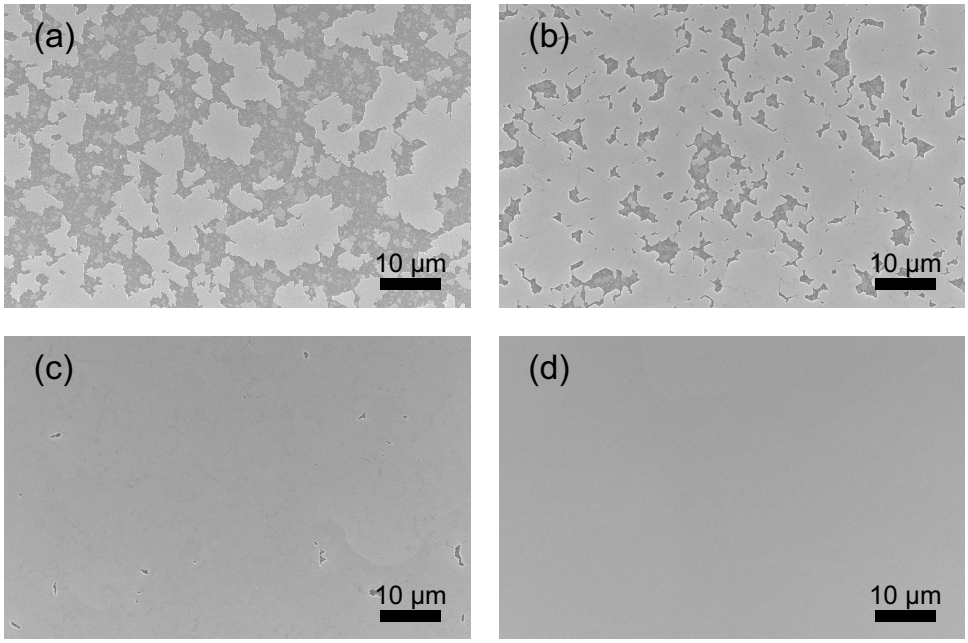

Figure 4.27: SEM micrographs of Sb_2Te_3 grown on Si(111) substrate with various ratios of DETe/TESb partial pressures: (a) 27.7; (b) 11.1; (c) 8; and (d) 6.

various $R_{VI/V}$ ratios. For the highest tested value of $R_{VI/V} = 27.7$, the Si surface is not fully covered with material and only islands of Sb_2Te_3 are found on the substrate, see Fig. 4.27 (a). A reduction of the VI/V ratio results in an improvement of the surface coverage, however a lot of micrometer-size openings are present in the layer deposited with $R_{VI/V} = 11.1$, shown in Fig. 4.27 (b). Further decrease of the $R_{VI/V}$ leads to significant improvement of the surface coverage and morphology. While small openings are still visible in the layer grown with $R_{VI/V} = 8$, Fig. 4.27 (c), epitaxy with $R_{VI/V} = 6$ results in deposition of fully coalesced, uniform, and smooth Sb_2Te_3 layer, for which a SEM micrograph is presented in Fig. 4.27 (d).

Adequate results are received with AFM measurements – the coverage of Si substrate

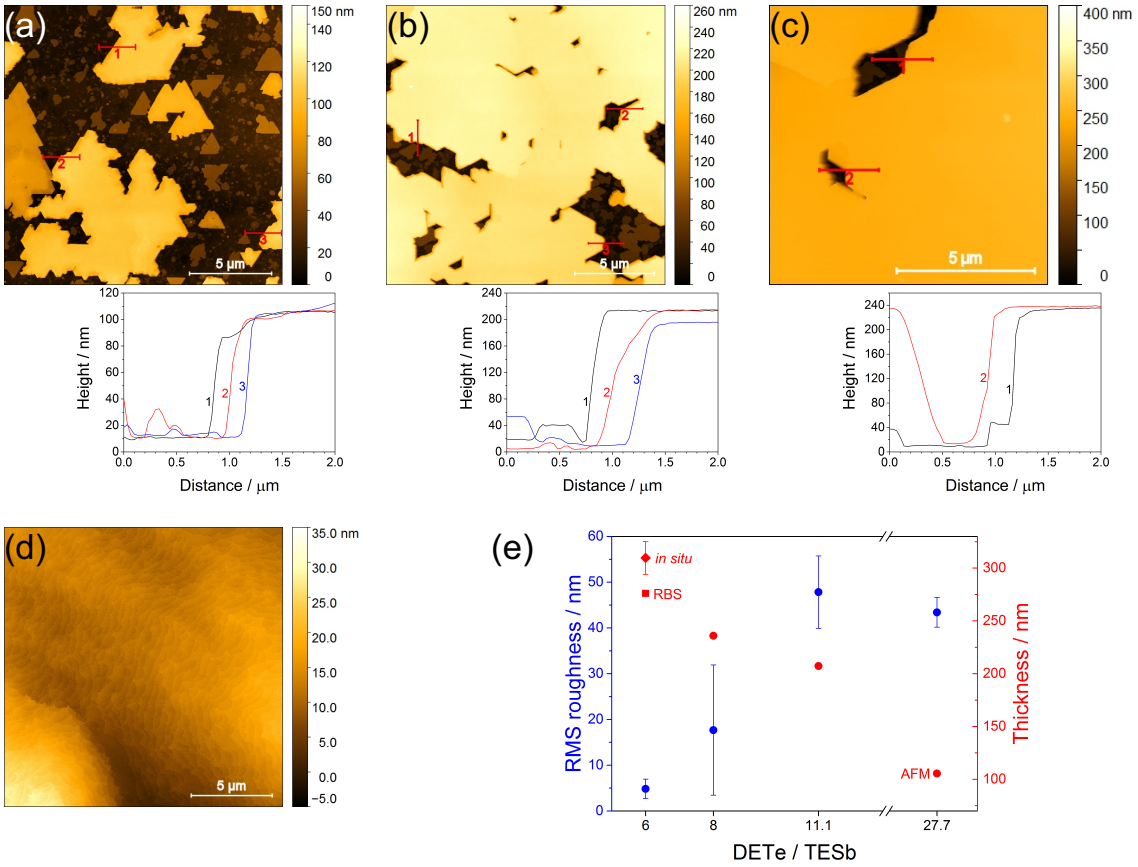

Figure 4.28: AFM characterization of Sb_2Te_3 grown on Si(111) substrate with various ratios of DETe/TESb partial pressures: (a)-(c) AFM images and height profiles along the red lines for samples deposited with the ratio of (a) 27.7, (b) 11.1 and (c) 8; (d) surface of fully coalesced layer grown with the ratio of 6; and (e) RMS roughness (blue) averaged over values extracted for each specimen from 4-5 AFM images (error bars mark the standard deviation), and thickness of islands/layer (red) extracted from height profiles in (a)-(c). For the layer grown with $R_{VI/V} = 6$ the thickness was estimated from *in situ* reflectance and RBS measurements.

increases with decrease of the $R_{VI/V}$ ratio. Moreover, AFM gives the possibility to measure the height of the deposited islands or incompletely coalesced layer by extracting the height profile over an opening in the film. The AFM characterization of the Sb_2Te_3 samples from the partial pressure ratio series is demonstrated in Fig. 4.28. The figure also presents the height profiles measured along the red lines in the corresponding AFM images (a)-(c). Measured heights are plotted versus $R_{VI/V}$ ratio in the chart in Fig. 4.28 (e) with red marks. The thickness of the fully coalesced layer, also plotted in the graph, was estimated from RBS and *in situ* reflectance measurements. For calculations of the growth rate from *in situ* measurement, the values of $n = 5.71$ and $\kappa = 2.03$ were assumed as refractive index and extinction coefficient of Sb_2Te_3 [19], respectively. The measured thickness of the deposited Sb_2Te_3 flakes/film increases with a decrease of the $R_{VI/V}$ ratio (which is equivalent to an increase of the TESb partial pressure) and takes values of around

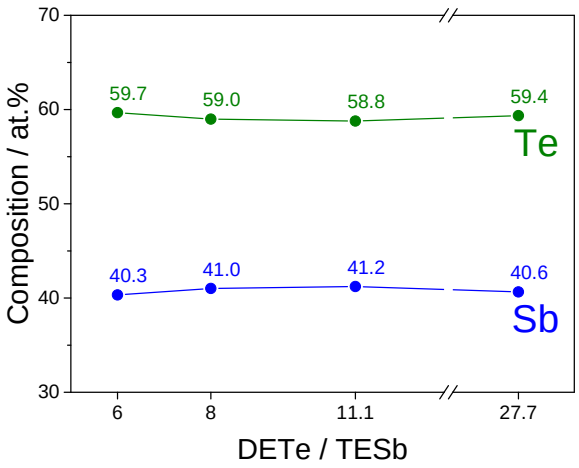

Figure 4.29: EDX-measured compositions of the Sb_2Te_3 grown with different ratios of DETe/TESb partial pressures on Si(111) substrate. The values next to the points in the chart indicate the atomic percentage of each element in the deposited material.

105 nm, 207 nm, 236 nm, and 276 nm (RBS) or 310 nm (*in situ*) for samples grown with DETe/TESb ratios of 27.7, 11.1, 8, and 6, respectively. It means that the access of Sb is a limiting factor for the growth of the material at given conditions. Fig. 4.28 (e) also represents the change of the RMS roughness with the $R_{VI/V}$ ratio. The roughness was extracted from 4-5 AFM micrographs, and its averaged values together with the standard deviation are plotted in the chart. A significant reduction of the RMS roughness is observed when the $R_{VI/V}$ factor decreases from 11.1 to 6. The epitaxy with the ratio of $R_{VI/V} = 6$ results in the deposition of a fully coalesced layer with the RMS roughness of ~ 4.82 nm, and the *in situ* measured growth rate equal to 7.74 nm $\cdot$ min^{-1}.

Finally, the composition and structure of the deposited materials were investigated using EDX and XRD. The EDX-measured atomic content for the samples from the series are displayed in Fig. 4.29. No pronounced difference in composition is revealed from the EDX analysis. All samples are Sb_2Te_3 with deviation below 1.5 at.% from the perfect alloy with a 2/3 ratio of Sb/Te atoms. The deviation is within a few-percent accuracy of the experimental method. Also, XRD 2θ-θ measurements verify the Sb_2Te_3 composition of the deposited materials. The XRD characterization is shown in Fig. 4.30, graph (a) presents 2θ-θ scans with the signal normalized to the intensity of the Si(111) reflex. The diffractograms do not show any hint of a compositional difference between the samples. The only explicit change is the relative intensity of the measured Sb_2Te_3 reflections, which is due to the variation of deposited layer thickness. The XRD ϕ-scans recorded around the (105) reflection of Sb_2Te_3 reveal the presence of rotational twin domains, however one of the domains is strongly suppressed. The reflections of the dominating domain are collinear with Si(220) reflexes, similarly as in case of MOVPE-grown $Ge_1Sb_2Te_4$ and in contrast with MBE-grown Sb_2Te_3 [95]. The scans measured for the samples grown with $R_{VI/V} = 8$ and $R_{VI/V} = 6$ are illustrated in Fig. 4.30 (b). Employing the Eq. 4.1, the fraction of the

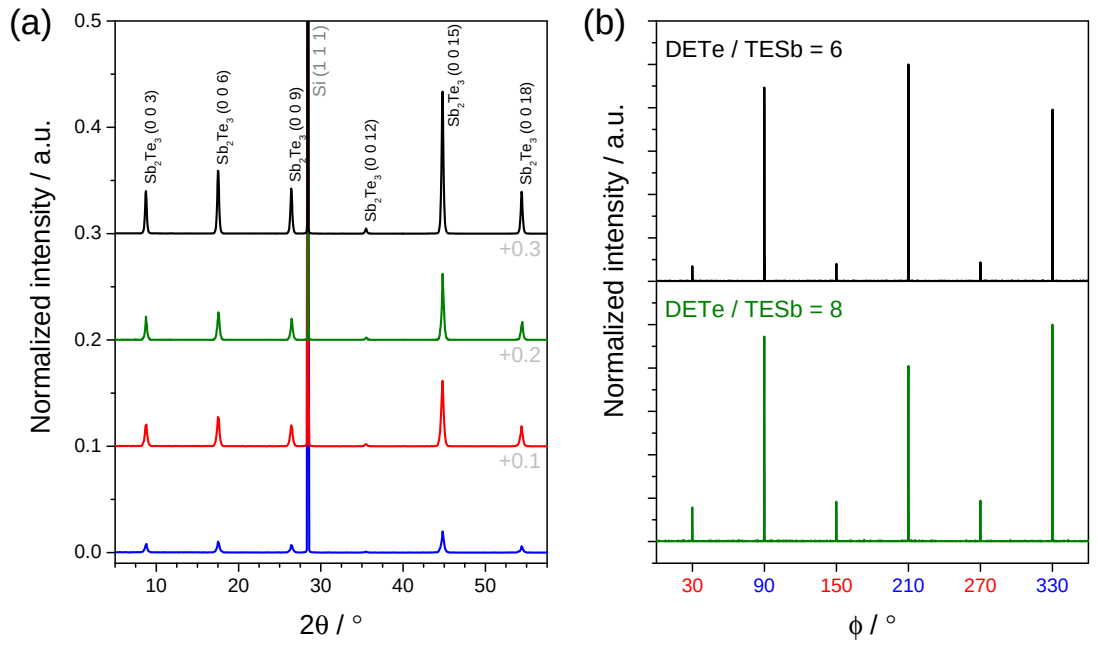

Figure 4.30: XRD measurements for Sb_2Te_3/Si(111) samples grown with various ratios of DETe/TESb partial pressures: (a) 2θ-θ scans – blue, red, green and black curves correspond to the precursors partial pressure ratio of 27.7, 11.1, 8 and 6, respectively (the curves are shifted vertically by 0.1 a.u. for the sake of clarity); and (b) ϕ-scan recorded around (105) reflection of Sb_2Te_3 for the two last of previously listed ratios, red and blue color code of x-axis labels marks the positions of Si(311) and Si(220) reflections, respectively.

β-domain [collinear to Si(311)] incorporated in the deposited layer was estimated from the intensities of the peaks in the ϕ-scan curves. While the $R_{VI/V}$ ratio is reduced from 8 to 6, the fraction of the β-domain in the layer decreases from ~ 0.16 to ~ 0.08. The result is somewhat unexpected, since the reduction of $R_{VI/V}$ ratio is achieved here by an increase of TESb partial pressure, which results in higher growth rate, as shown earlier in Fig. 4.28. The observation for Sb_2Te_3 is opposite from the one for GST alloys, where suppression of twin domain was observed with a reduction of the growth rate. Possible explanation of this behavior could be change of the growth mechanism from Volmer-Weber (islands formation for high values of $R_{VI/V}$) to Frank-van der Merwe (layer-by-layer growth for low $R_{VI/V}$). Perhaps, the layer-by-layer deposition from the early stage of epitaxy can favor one domain and cause a strong suppression of the other one. However, the growth mode has not been examined in detail here and further studies are required to draw the final conclusion.

The adjustment of the TESb/DETe partial pressures ratio for the growth of Sb_2Te_3 via MOVPE leads to a substantial improvement of the deposited samples morphology, without a change in the composition. The epitaxy with the ratio $R_{VI/V} = 6$ results in the deposition of fully coalesced and smooth layers with a relatively high growth rate. The found optimum $R_{VI/V}$ ratio is comparable with values reported earlier for deposition of Sb_2Te_3 utilizing the same precursors [98].

4.3.2 Growth temperature

In the next step, the MOVPE growth of Sb_2Te_3 was explored with respect to the deposition temperature, which was varied in the range from 425 °C to 500 °C with 25 °C step. The optimized partial pressure ratio of precursors $R_{VI/V} = 6$ was applied for all epitaxy runs in the series. Other growth parameters were kept constant at values given at the beginning of this section 4.3.

SEM micrographs of samples grown at various temperatures are depicted in Fig. 4.31. The sample presented in the image (c) is one of the samples from the partial pressure ratio series, discussed in the previous subsection, therefore it is taken here as a reference. A reduction of the temperature to 450 °C, and later to 425 °C, leads first to a vanishing of the film coalescence, and then to islands growth, as depicted in Fig. 4.31 (b) and (a), respectively. On the other hand, an increase of the temperature to 500 °C results in deposition of fully coalesced layer with cracks in the material, as visible in Fig. 4.31 (d).

Again, more detailed analysis of the deposited samples morphology was conduced using AFM, and the results are displayed in Fig. 4.32. In the figure, the micrographs of the samples grown at (a) 425 °C, (b) 450 °C, and (c) 500 °C are presented. The AFM image of the surface for the sample grown at 475 °C is shown in Fig. 4.28 (d). Fig. 4.32 (d) exposes the RMS roughness obtained from the AFM measurements for the samples grown at various temperatures. Two samples grown with lower temperatures are characterized with high roughness, in the range of ~ 50 nm. The layers grown at 475 °C and 500 °C have surface roughness in the order of a few nanometers. It is obvious that the temperature of 475 °C is optimal for the MOVPE growth of Sb_2Te_3, since the layer deposited at the highest temperature of 500 °C cracks – notice dark line in the bottom left corner of Fig. 4.32 (c).

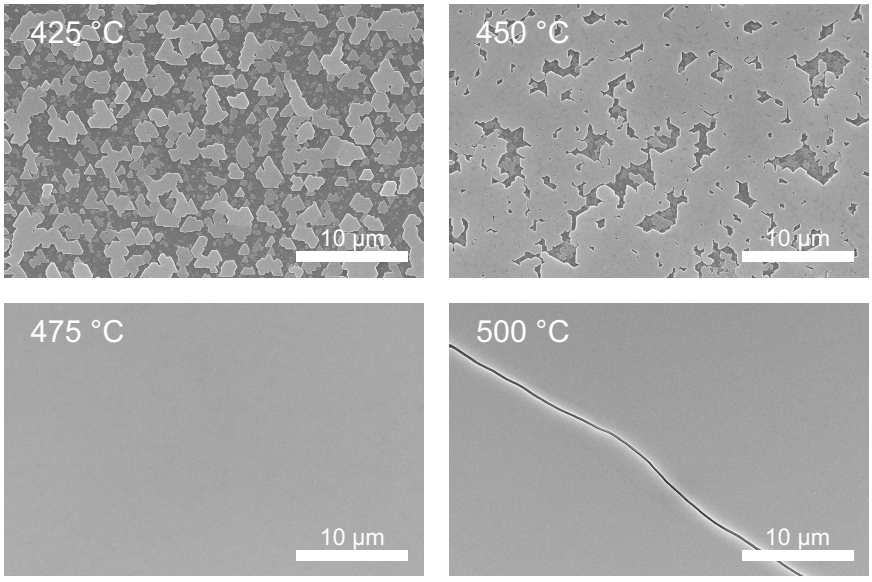

Figure 4.31: SEM images of Sb_2Te_3 grown on Si(111) substrate at different temperatures indicated in the pictures.

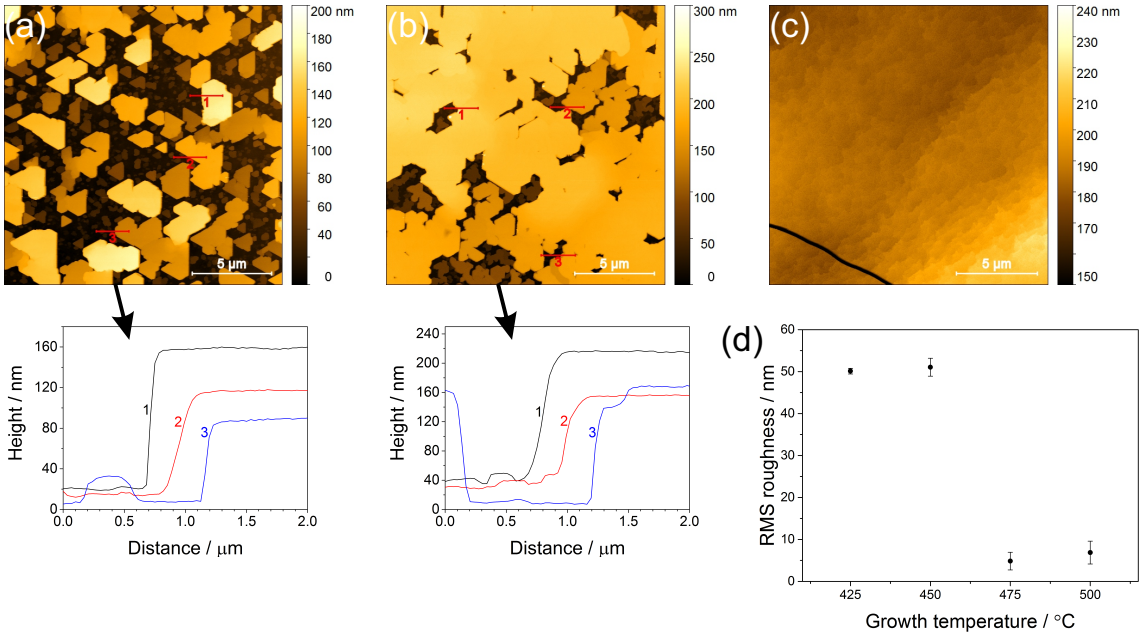

Figure 4.32: AFM characterization of Sb_2Te_3 grown on Si(111) at various temperatures: (a)-(c) AFM images and hight profiles along the red lines for samples deposited at (a) 425 °C, (b) 450 °C, and (c) 500 °C; (d) RMS roughness averaged over values extracted for each specimen from 4-5 AFM images – error bars mark the standard deviation.

Extracting the hight profiles from the AFM pictures, Fig. 4.32 (a) and (b), and using the *in situ* recorded reflectance for fully coalesced layers, the deposition rates were estimated to be 3.0 nm·min^{-1}, 4.5 nm·min^{-1}, 7.7 nm·min^{-1}, and 14.5 nm·min^{-1} for the Sb_2Te_3 specimens grown for 40 min at the temperatures of 425 °C, 450 °C, 475 °C, and 500 °C, respectively. The growth rates are plotted in Fig. 4.33 on a logarithmic scale and compared with calculated fraction of the decomposed precursors – TESb and DETe. The decomposition of the precursors and the deposition rates of the grown Sb_2Te_3 in dependence on the reciprocal growth temperature follow analogous tendency. It is an indication that the growth proceeds in the kinetic-controlled regime.

The layers grown at various temperatures do not exhibit difference in the composition of the deposited material. The content of the samples was verified with XRD and EDX measurements, which results are represented in Fig. 4.34. In 2θ-θ diffractograms merely reflections of Sb_2Te_3 (and the Si substrate) are found. The only change between the scans of the samples is relative intensity of measured Sb_2Te_3 reflections, normalized to the height of the Si(111) peak, as seen in Fig. 4.34 (a). The gain of the signal intensity is caused by the rise of layer thickness with increase of the growth temperature, as indicated in Fig. 4.33. The effect is especially pronounced for the temperature change from 475 °C to 500 °C. Also, EDX characterization does not reveal any compositional variation between the samples, see Fig. 4.34 (b). All specimens grown at temperatures from the range of 425-500 °C are Sb_2Te_3.

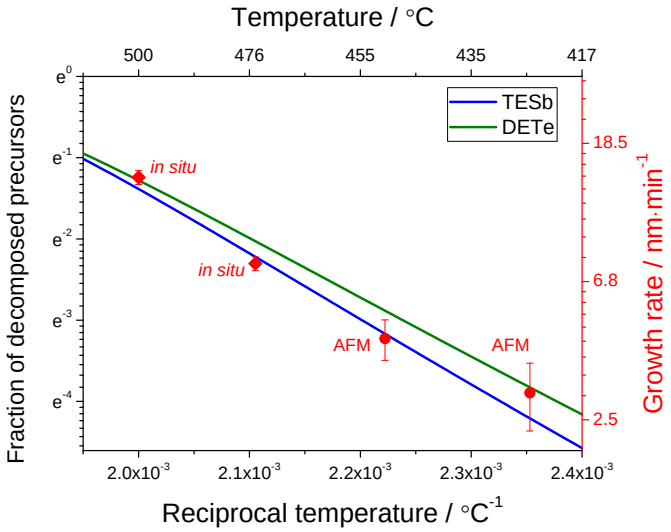

Figure 4.33: Growth rate of the deposited Sb_2Te_3 versus reciprocal growth temperature compared with the fraction of decomposed precursors. The decomposition curves of TESb (blue line) and DETe (green line) are calculated for the MOVPE 1119 reactor operated at TGF of 3000 sccm (as described in subsection 4.1.2). The hight of the Sb_2Te_3 island was measured with AFM (red dots) and the thickness of coalesced layers with *in situ* reflectance (red diamonds).

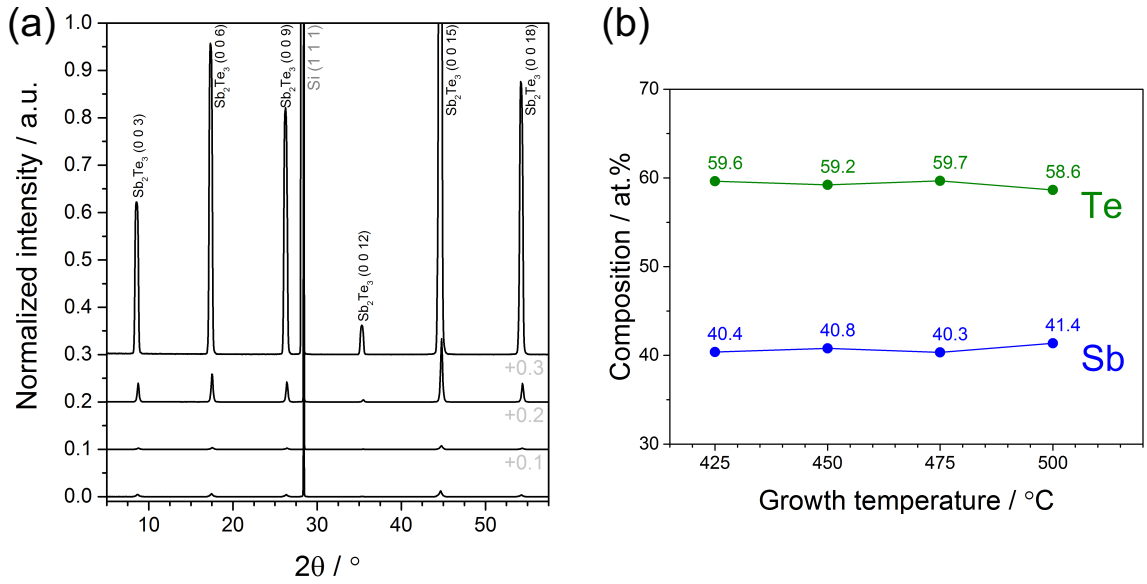

Figure 4.34: XRD and EDX compositional analysis of Sb_2Te_3/Si(111) grown at different temperatures: (a) 2θ-θ diffractograms, normalized to the intensity of the Si(111) reflex, measured for samples deposited at temperatures of (from the bottom to the top) 425 °C, 450 °C, 475 °C and 500 °C – the curves are shifted vertically by 0.1 a.u. for clarity; (b) EDX measured composition – the values next to the points in the graph indicate the atomic percentage of each element in the deposited material.

4.3.3 Substrate pretreatment

So far, all discussed Sb_2Te_3 samples were deposited after 30 min annealing of Si(111) substrate at 690 °C (with 2 min DETe injection in the end of the step) and 2 min pretreatment with Ge_2H_6 and TESb at the growth temperature, prior to the epitaxy. The influence of the pretreatment on the growth of GST alloys is known [4, 92]. Here, the effect of the pretreatment on the deposition of pure Sb_2Te_3 via MOVPE is investigated, mainly in the meaning of surface coverage and layer coalescence.

The sample grown with standard Ge_2H_6-TESb pretreatment is used as a reference. Additionally, three samples with various pretreatment conditions were prepared: (1) TESb for 2 min, (2) Ge_2H_6 for 2 min and (3) a sample without pretreatment step. If pretreatment was applied, 2 min break in precursors supply was introduced before the growth of the material was initiated. All specimens were deposited at the optimized conditions, i.e., 475 °C and $R_{VI/V} = 6$. The details about the pretreatment conditions for every sample are listed in Tab. 4.7. The difference between partial pressure of Ge_2H_6 applied for the reference samples and the sample No. 3 is caused by various values of TGF in the reactor during the pretreatment. In the case of the sample No. 3, there was no flow from the TESb source over the pretreatment step, therefore the TGF value was 2200 sccm. For the reference and the sample No. 2, TGF value during the pretreatment was 2600 sccm. However, the MFC setups and amount of Ge_2H_6 injected into the reactor was identical for both the reference and the sample No. 3.

Fig. 4.35 presents SEM micrographs of the Sb_2Te_3 samples grown after various Si(111) substrate pretreatment. The image (a) depicts the reference sample, for which standard 2 min Ge_2H_6-TESb pretreatment was applied. If Ge_2H_6 is not injected into the reactor in the step, the coalescence is lost and island growth is observed. The effect of the change is clearly revealed in the picture (b), which presents the sample grown on the substrate pretreated with TESb only. On the other hand, while the pretreatment is proceeded with exclusive injection of Ge_2H_6, further Sb_2Te_3 deposition results in the formation of a fully

Table 4.7: Tested pretreatment conditions prior to deposition of Sb_2Te_3 on Si(111) substrate.

Sample	Pretreatment	Partial pressure / mbar	Break / min
Reference	2 min Ge_2H_6-TESb	$8.26 \cdot 10^{-3}$ / $5.51 \cdot 10^{-3}$	2
No. 2	2 min TESb	$5.51 \cdot 10^{-3}$	2
No. 3	2 min Ge_2H_6	$9.76 \cdot 10^{-3}$	2
No. 4	no pretreatment	–	–

Note: The difference between Ge_2H_6 partial pressure for the reference and the sample No. 3 is due to the change of TGF during pretreatment. The amount of injected Ge_2H_6 was unchanged.

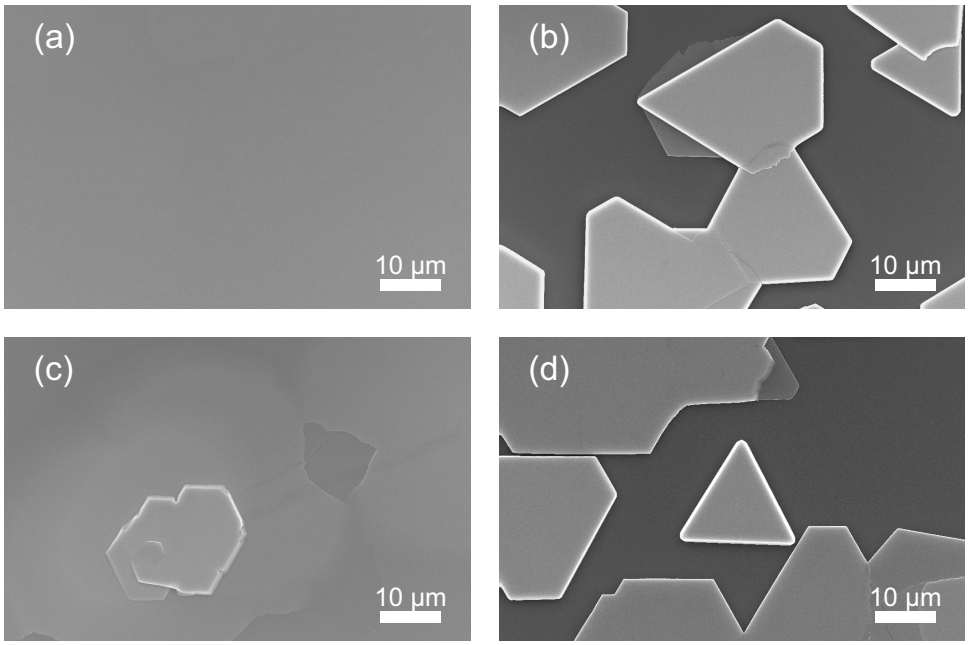

Figure 4.35: SEM micrographs of Sb_2Te_3 grown on Si(111) substrate after various surface pretreatment: (a) 2 min Ge_2H_6 and TESb; (b) 2 min TESb; (c) 2 min Ge_2H_6; and (d) no pretreatment.

coalesced film. Nevertheless, the layer is not as smooth and uniform as in the case of the growth after Ge_2H_6-TESb pretreatment. Islands and steps are found on the surface, as exposed in Fig. 4.35 (c). AFM-measured RMS roughness equals 11.05 nm for the sample grown after pretreatment with Ge_2H_6 only, compared to 4.82 nm for the reference sample grown after standard Ge_2H_6-TESb pretreatment. Finally, skipping the pretreatment step yields the result comparable with the outcome after the usage of TESb alone. The substrate is covered with islands, as depicted in Fig. 4.35 (d).

HAADF-STEM image taken around Sb_2Te_3/Si interface for the sample grown after 2 min Ge_2H_6-TESb pretreatment of Si(111) substrate is shown in Fig. 4.36. The Si surface is covered with a passivation layer, which is expected to be Te-rich due to the utilized pre-annealing atmosphere with the addition of DETe. As for the GST alloys, here the growth starts with vdW gap as well, revealing vdW type of epitaxy. The gap is followed by a 5-atomic-layer bloc indicating Sb_2Te_3 composition (denoted in Fig. 4.36 on the right-hand side). After the Sb_2Te_3 segment, a 7-atomic-layer block is found which corresponds to $Ge_1Sb_2Te_4$. The sequence repeats one more time in the same fashion, one block of Sb_2Te_3 plus one block of $Ge_1Sb_2Te_4$, and later pure Sb_2Te_3 is grown. $Ge_1Sb_2Te_4$ is formed because the surface contains Ge atoms after pretreatment with Ge_2H_6 and TESb. Here in Fig. 4.36, two segments of $Ge_1Sb_2Te_4$ are revealed, however spots with higher number of GST blocks (also $Ge_1Sb_4Te_7$) were found while carrying out the HAADF-STEM characterization.

All in all, similarly like in the case of GST alloys, also in the case of pure Sb_2Te_3, the pretreatment with Ge_2H_6 and TESb prior to the growth of the material strongly enhanced

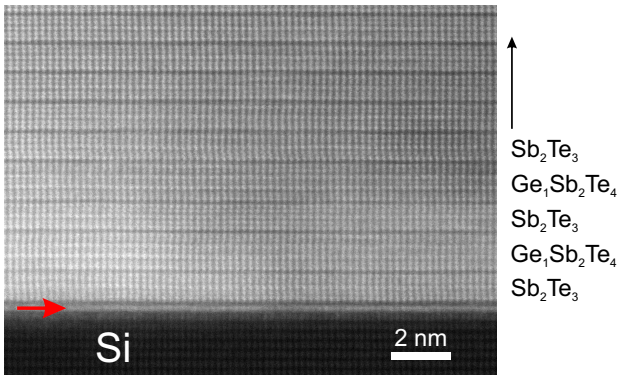

Figure 4.36: HAADF-STEM image around Sb_2Te_3/Si interface of the sample grown on Si(111) substrate pretreated for 2 min with Ge_2H_6 and TESb at the growth temperature. Red arrow marks the wetting layer on the Si surface. Composition of visible vdW-gap-separated segments is denoted on the right-hand side of the picture. Projection is along $[1\bar{1}0]_{ST}/[211]_{Si}$.

the Si(111) surface coverage. While Ge_2H_6 seems to be responsible for the film coalescence, the experiment suggests that TESb influences the layer morphology and uniformity. Hence, a 2 min substrate pretreatment with Ge_2H_6 and TESb before the deposition of Sb_2Te_3 via MOVPE on Si(111) substrate is an important step, in order to reproducibly grow uniform and coalesced layers of the material.

4.4 Growth of GeTe and Te-doped Ge

GeTe is the second of the components building iPCM superlattices, for which controllable and repeatable grow conditions are required while depositing GeTe/Sb_2Te_3 heterostructures. Therefore, the MOVPE growth condition for GeTe on the Si(111) substrate were investigated and are discussed in this chapter. The influence of the following parameters on the growth of GeTe was checked: doping with Sb, deposition temperature, TGF in the reactor, ratio of precursors partial pressures, and pretreatment with Ge_2H_6 and TESb before the growth. Tab. 4.8 provides details about the growth procedure explored for the deposition of GeTe on Si(111) substrate. Again, the starting point for the experiments was the procedure optimized for deposition of GST. The samples were grown on a quarter of a 2 inch Si(111) wafer cleaned chemically prior to the epitaxy, see subsection 3.1.4. Before the growth started, the substrate was annealed at 690 °C in H_2 atmosphere for 30 min, with addition of DETe in the last 2 min of the step. Then, the temperature was decreased to the growth temperature, the substrate was pretreated with Ge_2H_6 and TESb for 2 min, and finally 40 min deposition was initiated. The total pressure in the reactor was kept at the value of 50 mbar for all samples.

Table 4.8: The growth procedure and parameters used for the deposition of GeTe. The parameters written in dark red were investigated in detail.

	Annealing	**Cooling**	**Pretreatment**	**Break**	**Growth**
t / min	28 + 2	7-10	2	2	40
Carrier gas	H_2	N_2			
Precursors	DETe	–	**Ge_2H_6, TESb**	–	***$R_{V/IV}$, $R_{VI/IV}$***
T / °C	690	decreases	**425-475**		
p / mbar	50				
TGF / sccm	2600-3000	2182	2600	*	**1000-3000**

* 418 sccm less than during the growth

4.4.1 TESb doping

The experiments on the deposition of GeTe on Si(111) substrate started with the growth of a sample using a partial pressure of $1.33 \cdot 10^{-2}$ mbar for Ge_2H_6 and $1.33 \cdot 10^{-1}$ mbar for DETe, resulting in the VI/IV ratio $R_{VI/IV} = 10$. The growth temperature was set to 475 °C and the TGF value to 3000 sccm. The effect of the deposition is presented in Fig. 4.37 (a). Only a wetting layer is observed on the substrate surface, with randomly located, thin, circular islands of material, as shown in the picture. Such islands are typically created at

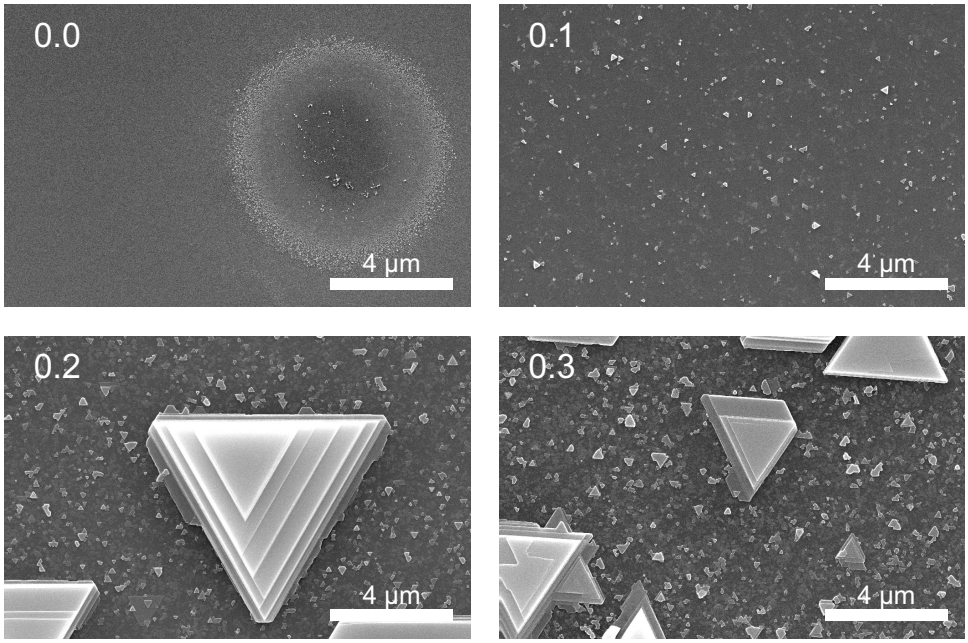

Figure 4.37: SEM images of Sb-doped GeTe grown on Si(111) substrate. The values in the top-left corners of the micrographs indicate TESb/Ge_2H_6 partial pressure ratio. The DETe/Ge_2H_6 partial pressure ratio was identical for all samples and equal to 10.

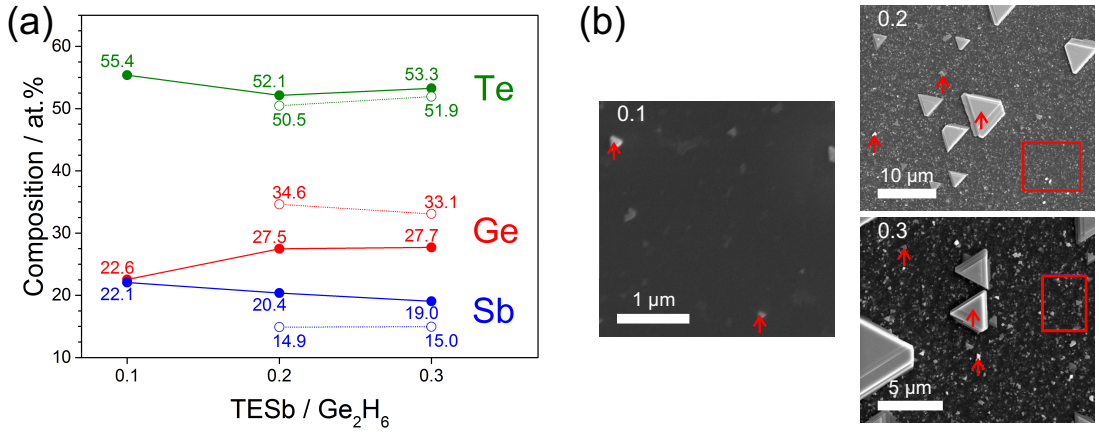

Figure 4.38: EDX compositional characterization of Sb-doped GeTe on Si(111) substrate: (a) composition of the deposited samples measured with EDX – filled dots mark the averaged results of point measurements on the deposited crystals, and open dots represent the compositions extracted from the area on the sample surface; (b) SEM images with red arrows pointing at the measurement spots [corresponding to filled dots in (a)] and rectangles indicating the analyzed areas [open dots in (a)]. The value in top-left corner of each picture gives TESb/Ge_2H_6 ratio.

nucleation centers originated from contamination residuals after chemical cleaning. Since there is basically no deposition while using only Ge and Te precursors during epitaxy, the next three samples were grown with the addition of TESb to the growth atmosphere. Sb is known to be a surfactant and plays catalytic role in deposition via MOVPE, as it has been reported for growth of Ge films [100]. Therefore, TESb to Ge_2H_6 partial pressures ratio $R_{V/IV}$ was gradually increased from 0.1 to 0.3. The ratio $R_{VI/IV}$ was unchanged and kept at a value of 10 for all samples. SEM micrographs of the specimens grown in presence of the Sb precursor are depicted in Fig. 4.37 (b)-(d). The SEM images reveal that the injection of TESb into the reactor during growth supports the deposition. While only small islands are grown for the ratio $R_{V/IV} = 0.1$, utilizing the V/IV ratio of 0.2 or 0.3 results in the deposition of micrometer-size triangular islands of material.

EDX and XRD analysis indicate that the composition of the deposited crystals does not match GeTe. The results of EDX experiments are illustrated in Fig. 4.38. The measurement was carried out as a point analysis of the deposited crystals, but also characterization of surface area between bigger islands of material was done. The addition of TESb at the level of $R_{V/IV} = 0.1$ results in the deposition of GST alloy with the composition of $Ge_2Sb_2Te_5$ except GeTe. Continued increase of TESb partial pressures shifts the content of the deposited crystals towards $Ge_3Sb_2Te_6$. Even mixtures close to $Ge_4Sb_2Te_7$ are found on the surface of the samples. Details about the composition of grown materials extracted from EDX measurements for various values of $R_{V/IV}$ ratio are listed in Tab. 4.9. Suprisingly, the composition of the grown alloys shifts towards higher GeTe content, while the partial pressure of TESb is increased. This behavior highlights the catalytic role of Sb in the deposition process.

Table 4.9: Composition of Sb-doped GeTe/Si(111) samples extracted from EDX measurements. Columns **Crystals** and **Area measurement** list compositions calculated from values marked with filled and open dots in Fig. 4.38 (a), respectively.

$R_{V/IV}$	Crystals	Area measurement
0.1	$Ge_{2.00}Sb_{1.96}Te_{4.91}$	–
0.2	$Ge_{3.00}Sb_{2.22}Te_{5.69}$	$Ge_{4.00}Sb_{1.72}Te_{5.83}$
0.3	$Ge_{3.00}Sb_{2.06}Te_{5.77}$	$Ge_{4.00}Sb_{1.81}Te_{6.28}$

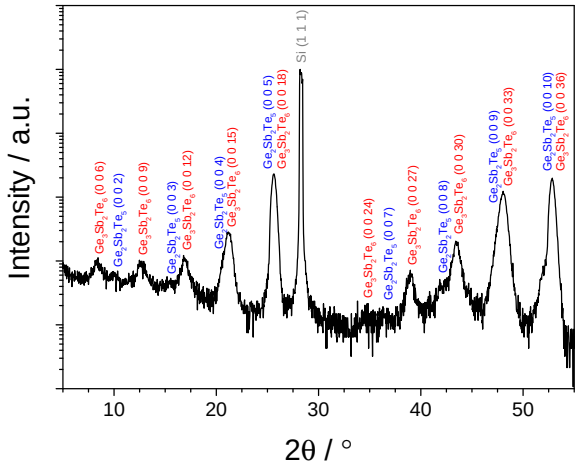

Figure 4.39: XRD 2θ-θ scan of Sb-doped GeTe sample grown with TESb/Ge_2H_6 ratio of 0.3. $Ge_3Sb_2Te_6$ and $Ge_2Sb_2Te_5$ reflexes are marked with red and blue labels, respectively.

Fig. 4.39 (b) presents the 2θ-θ scan of the sample grown with $R_{V/IV} = 0.3$. $Ge_3Sb_2Te_6$ reflections are dominating in the diffractogram, nevertheless indications for the presence of $Ge_2Sb_2Te_5$ are also found and marked with blue labels in the chart.

The study highlights the catalytic role of Sb in the deposition of materials from the GST family via MOVPE. Sb acts as a surfactant, enhancing the nucleation and growth of GST crystals on Si(111) substrate. Although it was aimed to grow GeTe, the epitaxy results in the deposition of $Ge_2Sb_2Te_5$ alloy already at low concentration of TESb vapors in the reacting atmosphere.

4.4.2 Growth temperature

Since the approach to grow GeTe on Si(111) substrate using surface-catalytic properties of Sb failed due to high incorporation of Sb in the grown material, the effect of the growth temperature on the epitaxy was examined in the next step. The temperature was varied from 475 °C down to 425 °C. The TGF value of 3000 sccm was applied and the samples were grown with precursors partial pressure ratios of $R_{VI/IV} = 10$ and $R_{V/IV} = 0.2$.

SEM micrographs of the specimens deposited at 475 °C, 450 °C, and 425 °C are depicted

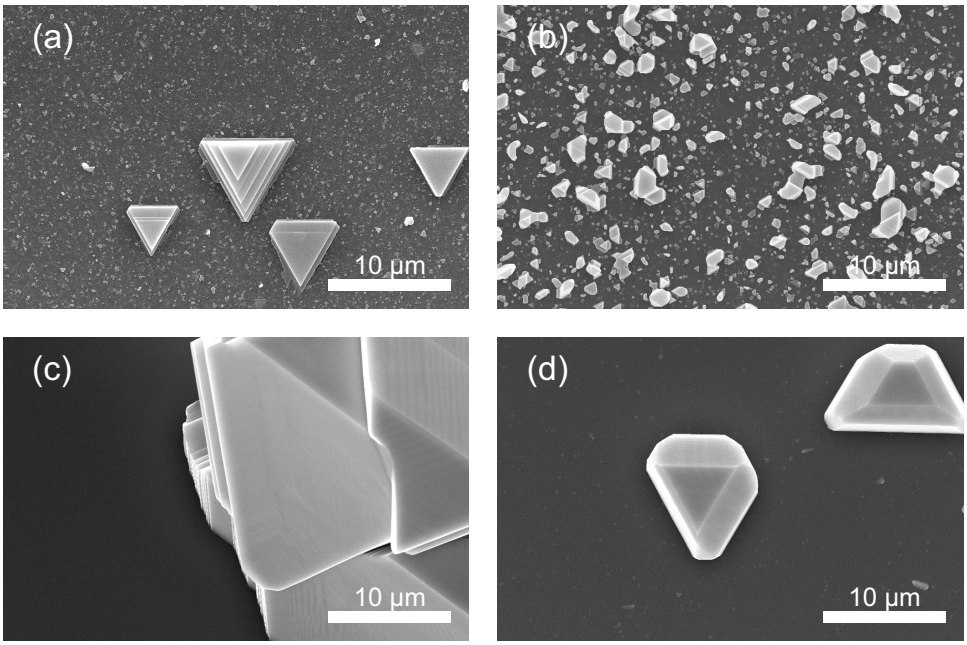

Figure 4.40: SEM pictures of GeTe grown on Si(111) at various temperatures: (a)-(c) Sb-doped with TESb/Ge_2H_6 ratio of 0.2 and at temperature of (a) 475 °C, (b) 450 °C, and (c) 425 °C; (d) undoped GeTe grown at 450 °C. All sample were grown with DETe/Ge_2H_6 partial pressure ratio of 10.

in Fig. 4.40 (a), (b), and (c), respectively. First, when the temperature is reduced from 475 °C to 450 °C, the size of deposited grains decreases but their density on the surface increases. A further reduction of the temperature to 425 °C leads to growth of relatively large crystals, compared to those formed at higher temperatures.

In the investigated range of temperatures, for the precursors (TESb and DETe) the growth proceeds in the kinetic-controlled regime, as described earlier in subsection 4.1.2. Therefore, it is expected that the reduction of the growth temperature affects the composition of the deposited crystals here as well. This assumption is confirmed with EDX characterization of the samples, presented in Fig. 4.41 (a). While the growth temperature is decreased to 450 °C, the incorporation of Sb in the deposited material drops drastically to $\sim 2.8\%$. Subsequently, lowering of the temperature reduces the content of Sb even more.

Since at the temperature of 450 °C Sb is not effectively incorporated in the grown crystals and the nucleation density is relatively high, the epitaxy was repeated without TESb in the reactor during the deposition. The VI/IV ratio was unchanged and equal to $R_{VI/IV} = 10$. The SEM image of the obtained sample is shown in Fig. 4.40 (d). Islands are found on the Si(111) surface. They are larger than in case of the deposition under TESb ambient, Fig. 4.40 (b), and the nucleation density is lower. The EDX analysis indicates the composition of the grown crystals is $Ge_{0.53}Te_{0.47}$. In addition, XRD 2θ-θ scan reveals the GeTe composition of the material. Moreover, 2θ-θ diffractogram exhibits that the deposited GeTe is a mixture of hexagonal and cubic phases – the pertinent reflexes are

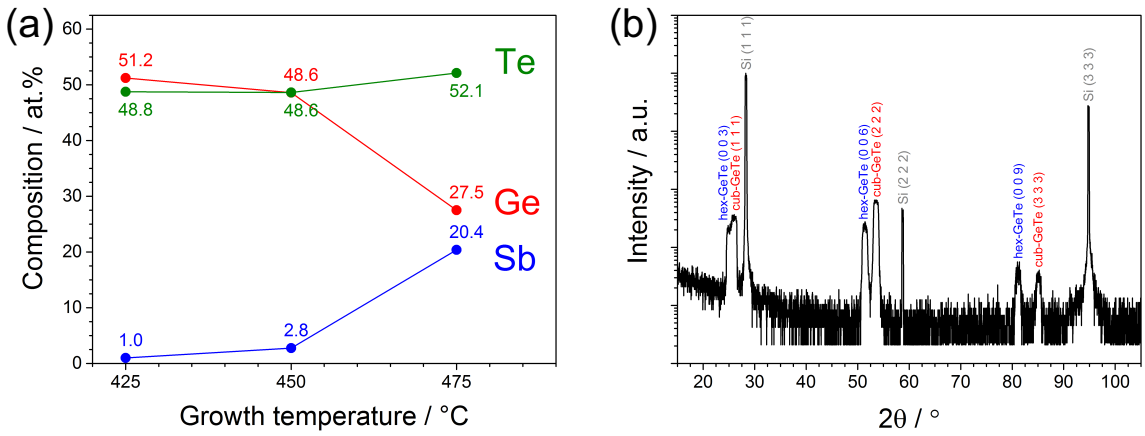

Figure 4.41: EDX and XRD characterization of GeTe samples grown at various temperatures: (a) EDX compositional analysis of the samples grown with Sb addition – TESb/Ge_2H_6 ratio of 0.2; (b) 2θ-θ diffractogram for the sample grown at 450 °C without TESb in the reactor. Blue and red labels with *hex* and *cub* prefix mark reflections of hexagonal and cubic GeTe, respectively.

marked in Fig. 4.41 (b) with blue and red labels, respectively. The reflexes of hexagonal an cubic GeTe were found in 2θ-θ curves measured for GeTe sample grown at 450 °C with addition of TESb too.

4.4.3 Total gas flow

To this point, the adjustment of the growth temperatures allowed for the deposition of GeTe islands. However, the nucleation density and Si surface coverage are quite low. Since the growth is kinetically-controlled, a series of samples grown with various values of TGF in the reactor was prepared and examined. A reduction of TGF causes an elongation of the precursors residence time in the reactor, hence higher fraction of the source gases decomposes. The TGF value was decreased stepwise form 3000 sccm to 1000 sccm. The temperature of 450 °C and the ratio $R_{VI/IV} = 10$ were unchanged between samples.

SEM images of specimens grown with TGFs of 1000-2500 sccm are presented in Fig. 4.42. The sample grown with the flow of 3000 sccm is the one depicted in Fig. 4.40 (d). As revealed by the SEM images, the density of crystals nucleated on the Si(111) surface increases significantly when the TGF value is reduced from 3000 sccm to 1500 sccm. Further decrease of the flow to 1000 sccm lowers the surface coverage, which suggests that the deposition rate is reduced. In the kinetic-controlled regime, the growth rate can be influenced by gas-phase reactions of precursors, which can change the molecules delivered to the surface and modify the surface reaction rate constant, as described in subsection 3.1.1. Here, the kinetic-controlled growth is a consequence of an incomplete decomposition of the Te precursors. At given conditions, Ge_2H_6 is expected to be fully decomposed on the surface. On the one hand, if the TGF is lowered, the growth rate is boosted due to more effective decomposition of DETe. On the other hand, the reduction of the TGF value

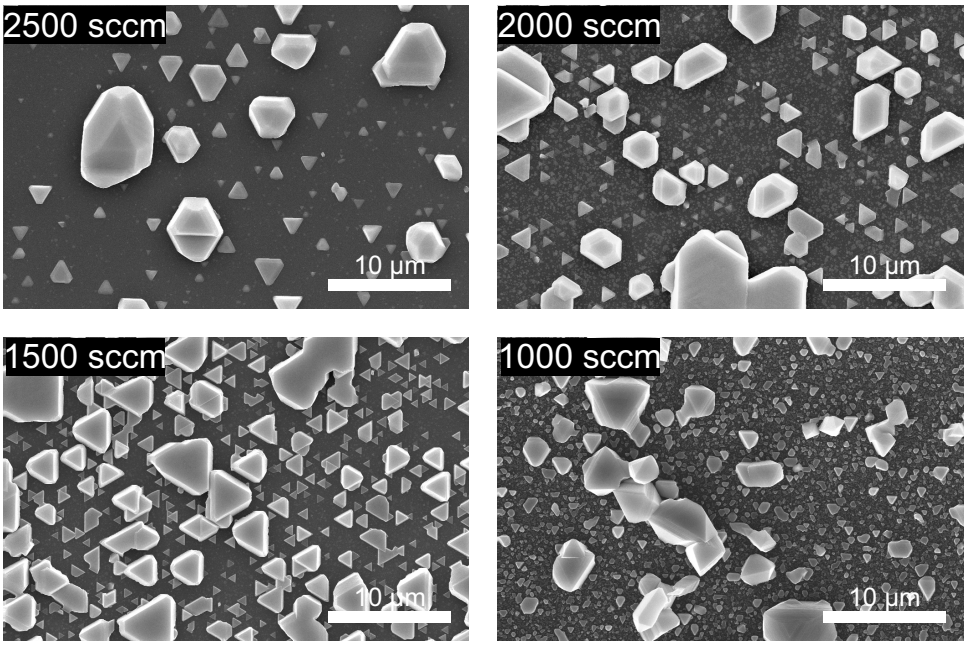

Figure 4.42: SEM micrographs of GeTe deposited on the Si(111) substrate under different TGFs in the reactor. The TGF was varied in the range of 1000-3000 sccm. The value of the flow of each sample is specified in the top-left corner of every image. The picture of the sample grown with TGF of 3000 sccm is presented in Fig. 4.40 (d).

causes an increase of the boundary layer thickness, which controls the transport of reactants from gas phase towards the substrate, according to Eq. 3.9. A rise of the boundary layer thickness could limit the amount of Ge accessed on the Si surface and consequently reduces the growth rate, which is typical for diffusion-controlled growth. Overall deposition regime, kinetic- or diffusion-controlled, is hard to defined and Grove model, introduced in subsection 3.2, is too simple for this case.

Experiments do not indicate significant compositional difference between the samples deposited with various values of TGF in the reactor during epitaxy. EDX analysis exhibits that all samples are GeTe with slightly higher Ge content compared to Te, as revealed in Fig. 4.43 (a). Also, XRD 2θ-θ scans validate the GeTe composition of the deposited materials, with mixed hexagonal and cubic phases revealed with reflexes marked in Fig. 4.43 (b) with blue and red labels, respectively. The graph presents the 2θ-θ scan measured for the sample grown with the TGF value of 1500 sccm. No difference was observed between 2θ-θ diffractograms measured for samples deposited with various values of TGF. All scans display peaks corresponding to reflections of hexagonal and cubic GeTe.

The study of the TGF influence on deposition of GeTe on Si(111) substrate showed that the highest crystal density and coverage of the Si(111) surface is received when the growth proceeds under the TGF value of 1500 sccm. No variation of the deposited crystals composition was observed with the change of the flow. However, two crystallographic structures were measured by means of XRD – hexagonal and cubic GeTe.

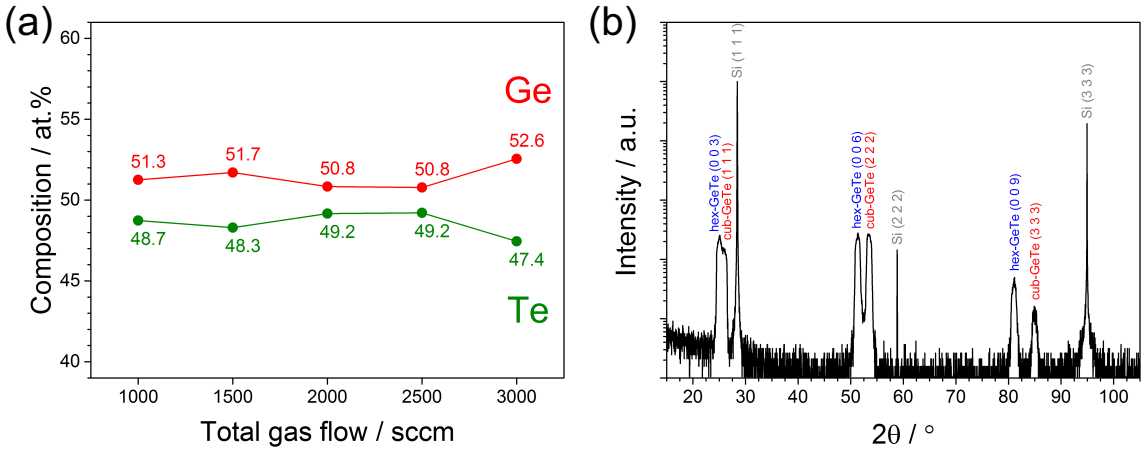

Figure 4.43: EDX and XRD characterization of GeTe samples grown with various values of TGF: (a) EDX compositional analysis of samples grown with different TGFs values; (b) 2θ-θ scan for the sample grown with TGF value of 1500 sccm. Blue and red labels with *hex* and *cub* prefix mark the reflections of hexagonal and cubic GeTe, respectively.

4.4.4 Partial pressure ratio

So far, high overpressure of DETe in relation to the Ge_2H_6 partial pressure was utilized for the deposition of GeTe – $R_{VI/IV} = 10$. In the next experiment, the partial pressure of DETe, and consequently the ratio $R_{VI/IV}$, was gradually reduced and its effect on the deposition was analyzed. All samples were deposited at 450 °C under the TGF value of 2000 sccm.

SEM micrographs of the samples grown with $R_{VI/IV}$ value stepwise reduced from 10.0 to 1.0 are shown in Fig. 4.44. For high overpressure of DETe the epitaxy results in the deposition of crystal grains. A reduction of the $R_{VI/IV}$ ratio to the range of 4.0-5.0 leads to an increase of the islands size above the length of 10 µm. With further decrease of the DETe partial pressure, layer growth is achieved, however single crystal grains can be found on the surface of the sample grown with $R_{VI/IV} = 2.5$. The transition from island-type to layer-type of growth, while the $R_{VI/IV}$ ratio is reduced from 4.0 to 2.5, looks quite abrupt. A closer look at the areas on the samples between the micrometer-size grains of material reveals that the layer forms progressively, but the contrast of Fig. 4.44 is not sufficient to completely resolve this issue. SEM pictures taken with higher magnification and better contrast for specimens deposited with $R_{VI/IV} = 10.0$ and $R_{VI/IV} = 4.0$ are depicted in Fig. 4.45 (a). Even for the ratio of 10.0, smaller material flakes are deposited between bigger crystalline islands. In the case of the sample grown with VI/IV ratio of 4.0, a non-coalesced layer is found on the Si surface. When the ratio is reduced to the value of 2.5 or lower, the island growth is suppressed and the layer fully coalesces.

The composition of larger crystals and layers (or flakes formed between these crystals that will eventually become layer) was analyzed with EDX. The compositional characterization is illustrated by means of chart in Fig. 4.45 (b). The atomic content of crystals

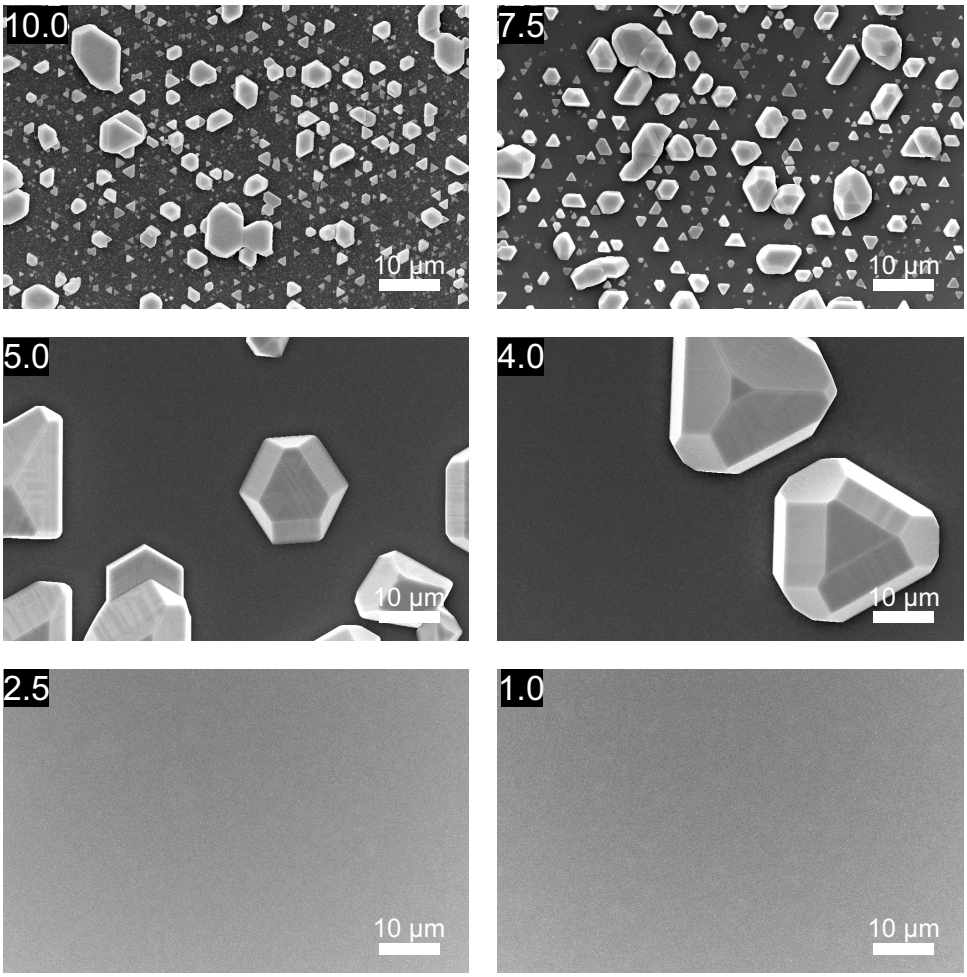

Figure 4.44: SEM images of samples deposited with various DETe/Ge_2H_6 partial pressure ratios. The value of the ratio for each sample is indicated in the top-left corner of every micrograph.

visible in SEM images in Fig. 4.44 is marked with diamonds and labeled as *crystals* in the graph. The atomic content does not change much with the variation of $R_{VI/IV}$ ratio and EDX measurements indicate crystals composition of GeTe. The situation is different in the case of the layers formed on the Si surface, which content is marked with bullets and *layer* label in Fig. 4.45 (b). Here, the composition is GeTe for $R_{VI/IV} = 10$, but the amount of Te incorporated in the material is gradually reduced, when the $R_{VI/IV}$ ratio drops. For the ratio $R_{VI/IV} \leqslant 5.0$ the atomic percentage of Te in the layer is in the range of few percent. The film deposited with the ratio $R_{VI/IV} = 1$ is basically Ge layer doped with Te at the level of $\sim 8‰$. Details about Te incorporation in the layer are given in Tab. 4.10.

The XRD characterization is consistent with EDX measurements. 2θ-θ diffractograms measured for the samples from the discussed series are presented in Fig. 4.46. Only reflexes corresponding to Si and GeTe (in hexagonal and cubic phase) are found in the curves recorded for samples grown with $R_{VI/IV}$ ratio of 10.0 and 7.5. First indication for the

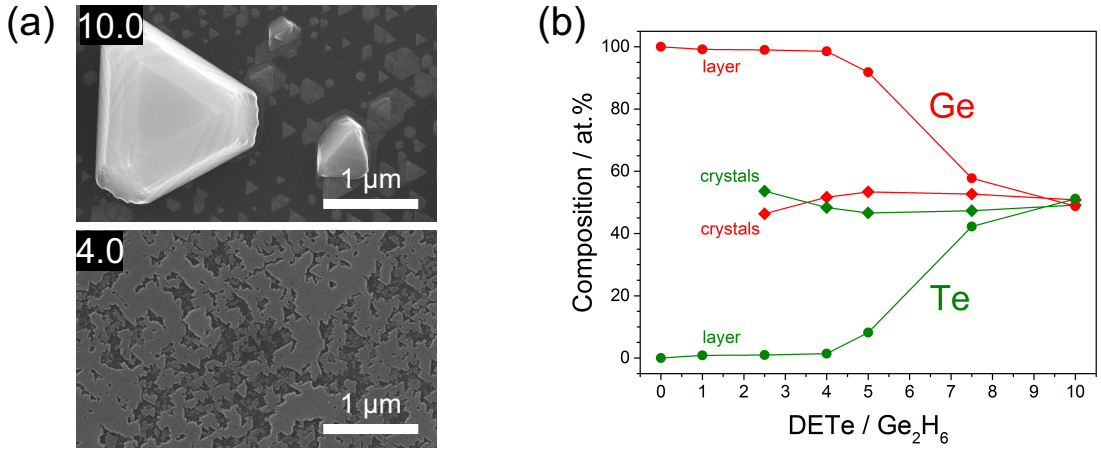

Figure 4.45: EDX analysis of GeTe samples grown with different ratios of DETe to Ge_2H_6 partial pressure: (a) SEM images of samples deposited with $R_{VI/IV} = 10$ and $R_{VI/IV} = 4$ (indicated in the top-left corner) showing the formation of a layer between GeTe crystals; (b) EDX measured composition of grown crystals (diamonds) and the subsequently formed layers (bullets).

Table 4.10: EDX-measured statistical composition of GeTe samples grown with various DETe/Ge_2H_6 ratio. Columns **Crystals** and **Layer** list compositions extracted for crystals and layers formed between them, respectively.

$R_{VI/IV}$	p_{DETe} / mbar	Crystals	Layer
10.0	$1.33 \cdot 10^{-1}$	$Ge_{0.508}Te_{0.492}$	$Ge_{0.488}Te_{0.512}$
7.5	$9.98 \cdot 10^{-2}$	$Ge_{0.527}Te_{0.473}$	$Ge_{0.578}Te_{0.422}$
5.0	$6.65 \cdot 10^{-2}$	$Ge_{0.534}Te_{0.466}$	$Ge_{0.918}Te_{0.082}$
4.0	$5.32 \cdot 10^{-2}$	$Ge_{0.517}Te_{0.483}$	$Ge_{0.986}Te_{0.014}$
2.5	$3.33 \cdot 10^{-2}$	$Ge_{0.464}Te_{0.536}$	$Ge_{0.990}Te_{0.010}$
1.0	$1.33 \cdot 10^{-2}$	–	$Ge_{0.992}Te_{0.008}$

presence of cubic Ge in a sample is observed in diffractogram of the specimen deposited with $R_{VI/IV} = 5$, where Ge(111) and Ge(333) reflexes rise over the noise level. For even lower $R_{VI/IV}$ ratios, GeTe reflections are progressively suppressed and the intensity of Ge peak grows. For the samples deposited with $R_{VI/IV}$ value of 2.5 and 1.0 only Ge (and Si) reflexes are recognized in the 2θ-θ diffractograms.

Gradual reduction of DETe partial pressure during GeTe deposition did not lead to the growth of the desired GeTe layers, but smooth Ge films are grown instead. Therefore in the next subsection, the epitaxy of Te-doped and pure Ge is investigated in detail.

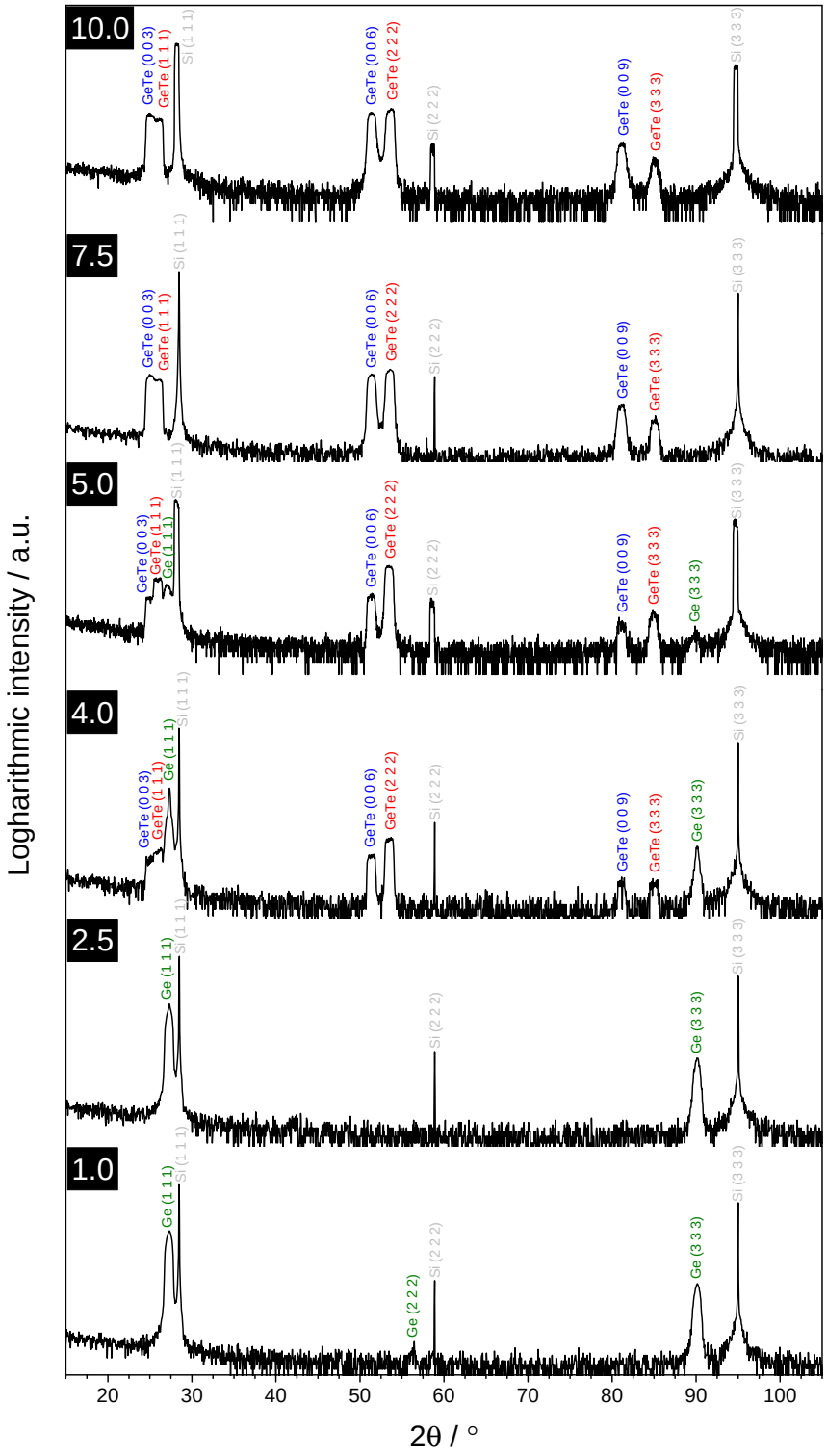

Figure 4.46: XRD 2θ-θ scans of GeTe samples grown with various DETe/Ge_2H_6 partial pressure ratios (indicated in black labels on the left-hand side). All observable reflections are signed in the chart.

4.4.5 Growth of Te-doped Ge

Earlier reported studies showed that MOVPE of Ge on TiAlN surface is possible utilizing catalytic role of Sb [100]. The growth of Ge has been observed only in presence of Sb precursor in the reactor. Here in contrast, the growth of Ge proceeds in the presence of Te precursor. Te have been used as catalyst in the growth of Ge films on Si(100) via MBE [101, 102]. It was found that layer-by-layer growth of Ge on Si substrate is achieved instead of Stranski-Krastanov growth, if the substrate surface is covered with a monolayer of Te prior to Ge growth. The presence of Te does not only support the deposition of the Ge layer, but at the same time also improves its crystallinity. Moreover, Te atoms do not incorporate in MBE-grown Ge layers, but rather accumulate on the surface of the specimen. Similar effects are observed in this work for MOVPE-grown Ge films doped with Te.

The deposition of Ge and Te via MOVPE with DETe/Ge_2H_6 partial pressure ratio $R_{VI/IV} = 1.0$ results in growth of fully coalesced Ge layer contaminated with Te atoms at the level of $\sim 8‰$. In order to investigate the effect of Te on the growth, another sample was deposited with the ratio $R_{VI/IV} = 0.0$, which means that only Ge_2H_6 was injected into the reactor and pure Ge was grown. As expected, the composition of deposited material is Ge, indicated with EDX – the result is marked in presented earlier Fig. 4.45 (b). The presence of other elements in the layer (i.e., Sb or Te) is not resolved with the EDX analysis. Removing DETe from the growth atmosphere has enormous influence on deposited sample morphology. Although the Si(111) substrate is still fully covered with Ge, the roughness of the layer increases significantly, which is depicted in SEM pictures presented in Fig. 4.47. Image (a) shows the surface of layer grown with $R_{VI/IV} = 1.0$, the same specimen is depicted in Fig. 4.44 (f) with lower magnification. The sample surface is flat and covered uniformly with nanometer-size dots. Subsequently, micrograph (b) presents the surface of pure Ge layer grown the without addition of DETe – $R_{VI/IV} = 0.0$. The layer appears rough in contrast to the sample deposited under Te ambient. The change of roughness is confirmed with AFM characterization of the specimens, shown in Fig. 4.48.

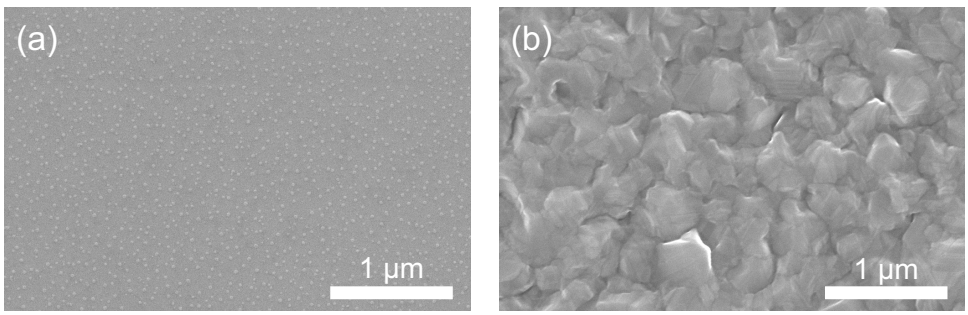

Figure 4.47: SEM micrographs of Ge/Si(111) grown with and without the addition of Te: (a) deposition with DETe/Ge_2H_6 partial pressure ratio of 1.0; and (b) deposition of pure Ge, no DETe injected during growth.

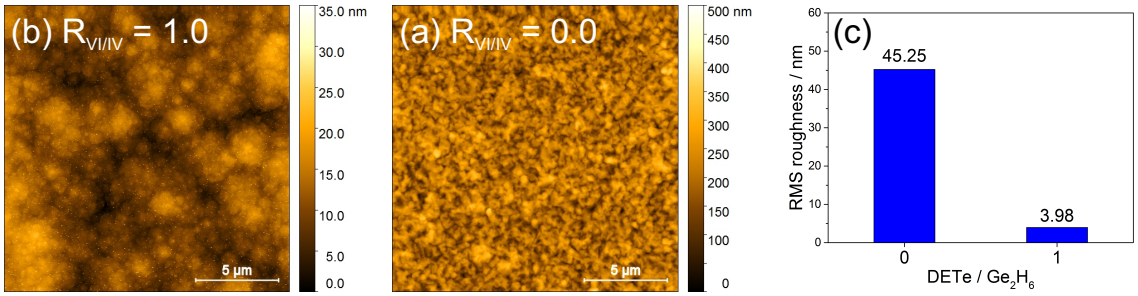

Figure 4.48: AFM characterization of Ge deposited on Si(111) with and without the addition of Te: (a) image of sample grown with DETe/Ge_2H_6 ratio of 1.0; (b) image of pure Ge layer surface; and (c) RMS roughness calculated for specimens presented in (a) and (b) – mean value from 3-4 measurements.

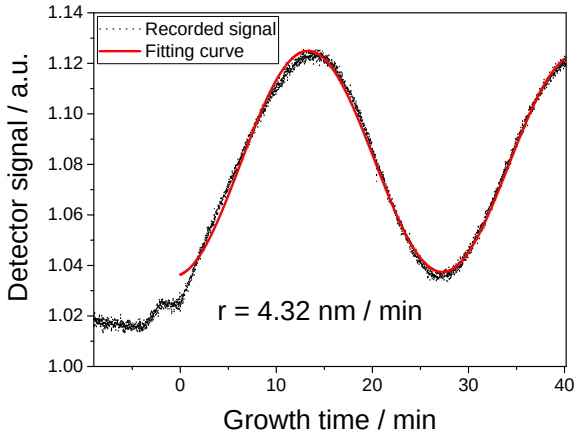

Figure 4.49: Time-resolved reflectance measured *in situ* for the Ge layer grown under Te ambient – DETe/Ge_2H_6 partial pressure ratio of 1.0. Black dots mark recorded signal and the red line shows the fitting curve. The layer grown for 40 min is around 173 nm thick, which corresponds to the growth rate of 4.32 nm·min^{-1}.

AFM images in Fig. 4.48 (a) and (b) show the surface of the samples grown with and without DETe, respectively. Fig. 4.48 (c) illustrates the chart which compares the RMS roughness extracted from the AFM measurements for both samples. The change in the morphology is clearly revealed. Injection of DETe (with DETe/Ge_2H_6 ratio of 1.0) into the reactor during Ge deposition reduces the surface roughness by the factor of ~ 11. The deposited Te-doped Ge film is characterized with the RMS roughness of 3.98 nm. This is value comparable with the one reported for Ge films grown in the presence of Sb on TiAlN substrate [100]. However, the deposition rate for Sb-doped Ge was indicated to be below 0.4 nm·min^{-1}. Here, the growth rate is more than 10 times higher. The *in situ* recorded time-resolved reflectance was used to determine the rate. The refractive index and extinction coefficient for Ge were assumed to be $n = 4.661$ and $\kappa = 0.279$ [103], respectively. The measurement curve and the simulation fitted with the LayTec software are plotted in Fig. 4.49. The layer was deposited for 40 min and its thickness amounts to 173 nm, which results in the growth rate of 4.32 nm·min^{-1}.

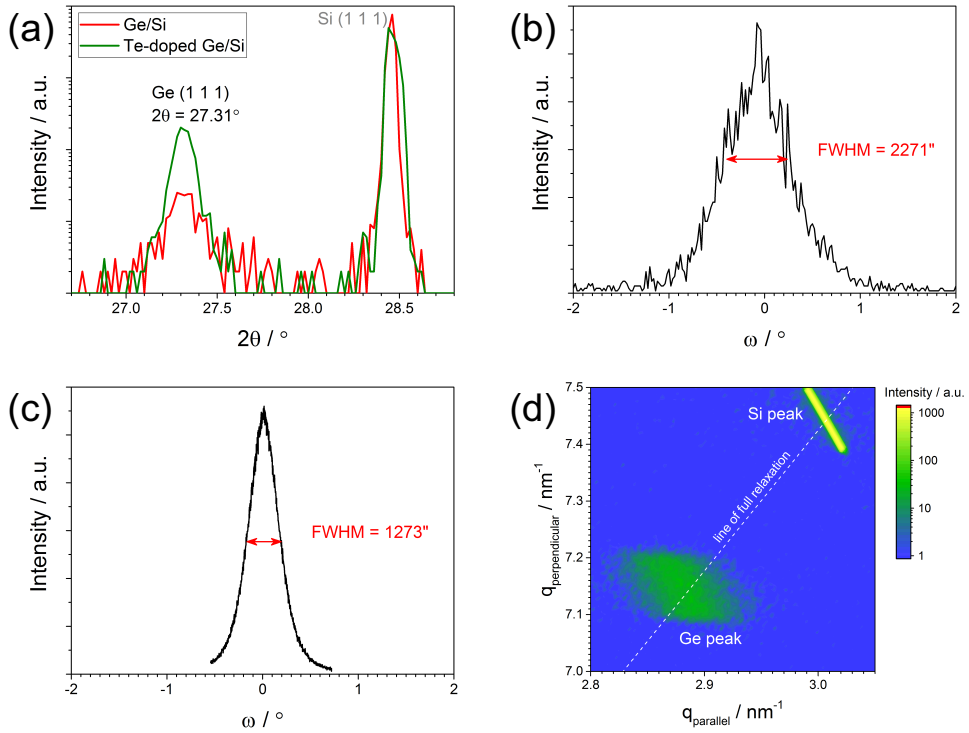

Figure 4.50: XRD characterization of Ge layers on Si(111) substrate grown with and without addition of DETe: (a) 2θ-θ scan for pure Ge (red) and Te-doped Ge layer (green); (b) and (c) rocking curve (ω-scan) measurements around Ge(111) reflex for sample grown without and with addition of Te, respectively; and (d) RSM recorded around Ge(133) reflection for Ge sample grown in presence of DETe.

The deposited Ge layers were characterized extensively with XRD. For MBE-grown Ge on Te-saturated Si surface, it has been found that the presence of Te improves the crystalline quality of the deposited layer [101, 102]. The quality of Ge film is also improved in the case of MOVPE, when the epitaxy proceeds in the presence of Te precursor. Fig. 4.50 demonstrates XRD measurements carried out on the Ge samples. Fig. 4.50 (a) illustrates short 2θ-θ scans of pure Ge and Te-doped Ge films – red and green line, respectively. The intensity of Ge(111) peak is an order of magnitude higher in the case of Ge layer grown with addition of Te, while both Si(111) peaks have comparable hight. It is first indication of higher crystalline quality of Ge:Te sample. For both samples rocking curve measurement was taken around Ge(111) reflection. The results are depicted in Fig. 4.50 (b) and (c), for pure Ge film and for the layer grown with addition of Te, respectively. In rocking curve, the full width at half maximum (FWHM) of recorded peak reflects the structural quality, i.e., the amount of extended defects in measured specimen. The higher is the quality of the examined crystal, the sharper is the peak. For pure Ge layer grown on Si(111), the FWHM of recorded peak has value of 2271 arcsec. While Ge is grown in the presence of DETe, the FWHM of Ge(111) peak is reduced to 1273 arcsec – nearly to the half of the initial value. The experiment clearly reveals the improvement in crystallinity of the Ge film, caused by

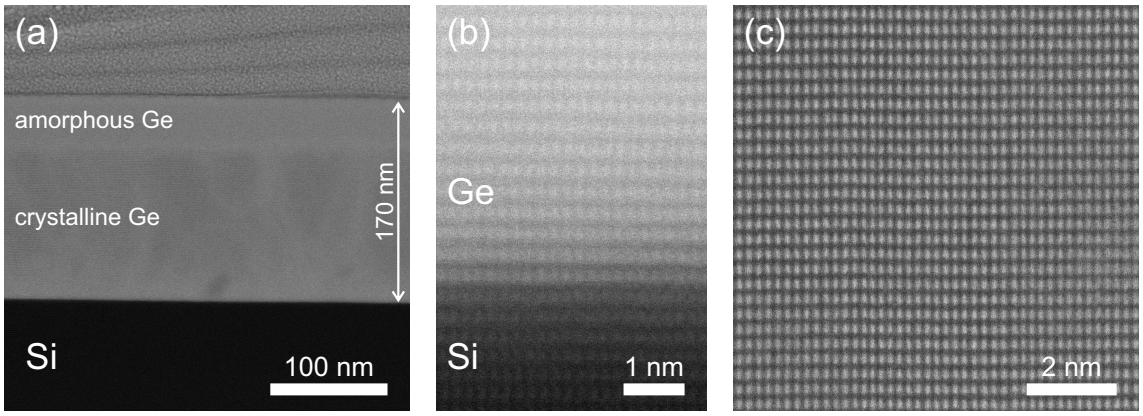

Figure 4.51: HAADF-STEM micrographs of Ge grown in the presence of DETe on Si(111): (a) broad-view image of the layer; (b) close-up of Ge/Si interface; and (c) crystalline Ge layer. Projection is along $[211]_{\mathrm{Si}}$.

the presence of Te precursor in the reactor during the growth. Also, RSM was recorded for Ge:Te layer around Ge(133) reflection. Presented in Fig. 4.50 (d) map indicates that grown layer is fully relaxed, as the Ge peak coincides with the line of full relaxation. The coordinates of Ge(133) peak center are $(q_{\parallel},\ q_{\perp}) = (2.885137\ \mathrm{nm}^{-1},\ 7.140519\ \mathrm{nm}^{-1})$ in reciprocal space – $q_{\parallel}$ and $q_{\perp}$ represent the parallel and perpendicular component, respectively. The Ge layer is grown in cubic crystal structure, therefore the lattice constant of the material can be calculated according to the equation

$$a = \sqrt{\frac{h^2 + k^2 + l^2}{q_{\parallel}^2 + q_{\perp}^2}}, \tag{4.8}$$

where h, k, and l denote Miller indexes of the reflection, (133) in discussed case. Then, the lattice constant of the deposited Ge, determined from analyses of RSM, takes the value of $a \approxeq 5.6599$ Å. The measured lattice parameter is in the agreement with the values reported earlier in the literature, e.g., $a \approxeq 5.6575$ Å [104] or $a \approxeq 5.6460$ Å [105], .

The crystallinity of Ge:Te sample was also investigated with HAADF-STEM. Obtained images are shown in Fig. 4.51. Micrograph (a) reveals that Ge film consists of ~ 130 nm crystalline and ~ 40 nm amorphous layer on the top. The total thickness of the film is measured to be ~ 170 nm, which is consistent with the value obtained from *in situ* time-resolved reflectance signal analysis. Fig. 4.51 (b) depicts a close-up of the interface between Si substrate and Ge layer. Since there is $\sim 4.2\%$ mismatch between Si and Ge lattice constants ($a_{\mathrm{Si}} \approxeq 5.431$ Å and $a_{\mathrm{Ge}} \approxeq 5.658$ Å), one could expect to find defects at the interface, such as misfit dislocations, which would lead to strain relaxation. However, HAADF-STEM images do not resolve crystal defects close to the interface. The crystalline part of Ge layer shows high degree of crystallinity, as revealed in Fig. 4.51 (c).

So far, the crystallinity of Ge:Te layer grown on Si(111) has been examined and discussed extensively. Also, the composition of the material was indicated with EDX and

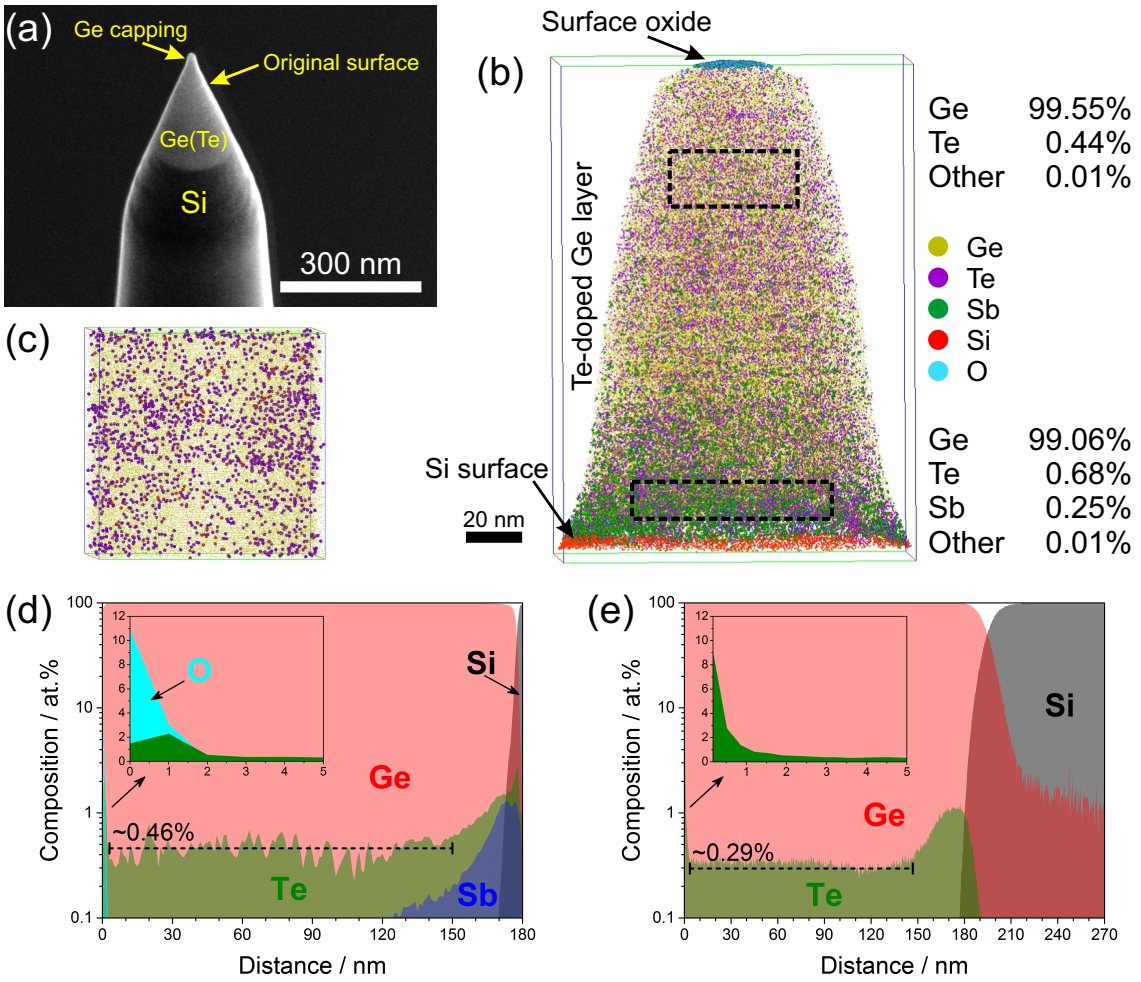

Figure 4.52: APT and SIMS characterization of Ge layer grown in presence of DETe: (a) SEM image of analyzed conical specimen; (b) APT recorded three-dimensional atom map of the specimen – not all recorded elements are shown. Local mass spectra of regions marked with dashed-line rectangles were analyzed, extracted atomic content for the regions is written on the right-hand side of the image; (c) 30-nm-edge-cube atom map from the middle of the Ge film – all elements are shown; (d) composition profile of the layer extracted from APT data; and (e) SIMS-measured composition profile of the sample. Insets in (d) and (e) show close-ups of the profiles near to the Ge surface.

XRD 2θ-θ scan. Here, the atomic content of the layer is analyzed using SIMS and APT. Fig. 4.52 summarizes the results of the performed measurements. A conical specimen was prepared from a piece of Ge/Si sample grown in the presence of the Te precursor in the reactor during epitaxy. The cone is shown in SEM picture in Fig. 4.52 (a). The composition of the specimen was explored with APT. The result of the experiment is illustrated in Fig. 4.52 (b). The mass spectrum was analyzed in two regions marked in the image (b) with dashed-line rectangles. In the region closer to the surface of the sample the material is 99.55 at.% Ge with Te at the level of 0.44 at.%. Deeper in the film, close to Si/Ge interface, content of Ge is 99.06 at.%, the concentration of Te atoms is slightly higher at the level

of 0.68 at.%, and also Sb is detected with an amount of 0.25 at.%. Higher concentrations of Te and the presence of Sb near to the interface between Si and Ge is caused by the substrate treatment prior to the growth: first a high-temperature annealing with DETe in the reactor and later a pretreatment with Ge_2H_6 and TESb. The contamination with Sb can be reduced by skipping the pretreatment step, which involved TESb. Experiments show that the pretreatment is not relevant for deposition of fully coalesced Ge layers.

The distribution of Te atoms in Ge layer is not uniform, as resolved in spatial atom map depicted in Fig. 4.52 (c), which shows all recorded atoms in a 30-nm-edge cube analyzed from the middle of the film. In Fig. 4.52 (d) the concentration profile of the layer extracted from APT measurement is plotted. The averaged concentration of Te atoms in the material is calculated to be around 4.6‰, in the distance range market in the graph. As noticed earlier, the content of Te is higher close to Ge/Si interface, where also Sb is found. The surface of the specimen is oxidized, as revealed in the inset in the chart presented in Fig. 4.52 (d). Also, a slightly higher concentration of Te is observed on the surface. The composition profile obtained from the APT data is compared with SIMS analysis of the film, shown in Fig. 4.52 (e). SIMS indicates a bit lower concentration of Te in the layer (compared to APT data) at the level of $\sim$ 2.9‰. As in APT, higher concentrations of Te at the interface between Si and Ge is also resolved with SIMS – recorded peaks in the profiles are at comparable levels. In contrast to the APT analysis, SIMS exposes higher concentration of Te on the surface of the Ge film, see inset in Fig. 4.52 (e). The difference could be due to the fact that lower number of elements is analyzed in SIMS experiment with respect to the APT measurement. In APT, additionally oxygen and antimony atoms are measured, which causes the change in the recorded relative concentration of elements in the film. Nevertheless, the values of Te concentration measured with EDX ($\sim$ 8.0‰), APT ($\sim$ 4.6‰), and SIMS ($\sim$ 2.9‰) are all in the same order of magnitude and can be considered as consistent. All experiments indicate very high doping concentration of Te donors at the level of $\sim 10^{20}$ cm^{-3}.

Reduced total gas flow

As described above, the Ge:Te sample was grown with the TGF value of 2000 sccm. However, in case of GeTe samples grown on Si(111) substrate, reduction of the TGF value down to 1500 sccm resulted in an increase of the substrate coverage, as revealed in Fig. 4.42. The reduction of the TGF value most likely influences the fraction of the decomposed DETe, as it has already been discussed in earlier chapters – see subsection 4.1.2. The effect of the TGF value decrease on the deposition of Ge on Si(111) in presence of Te precursor was also examined. A sample grown with TGF value of 1500 sccm was prepared and compared to the one deposited with the flow of 2000 sccm. The TESb/Ge_2H_6 pretreatment step was not utilized prior to the deposition of the Ge sample grown with TGF value of 1500 sccm. The VI/IV ratio of $R_{VI/IV} = 1.0$ was applied. The substrate temperature of 450 °C and other growth parameter were unchanged.

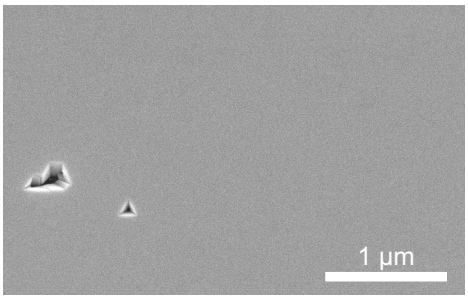

Figure 4.53: SEM image of Ge:Te layer grown with TGF value of 1500 sccm on Si(111).

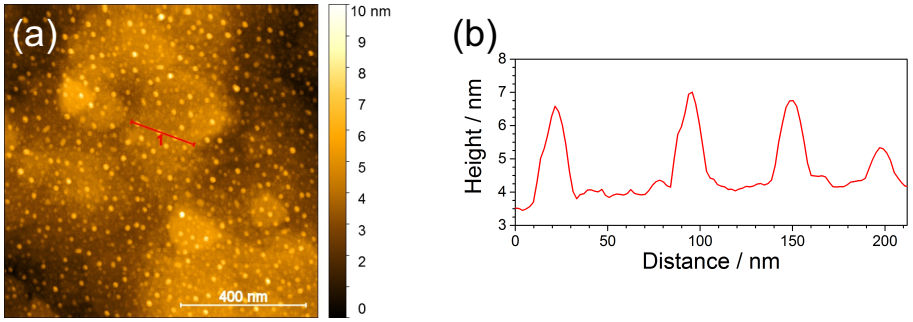

Figure 4.54: AFM characterization of the Ge:Te sample grown with the TGF of 1500 sccm: (a) 1 µm × 1 µm image of the sample surface; and (b) height profile extracted along red line marked in (a).

SEM micrograph of Ge film grown with the TGF value of 1500 sccm in the presence of DETe is presented Fig. 4.53. The layer is coalesced and looks smooth, however nanometer-size opening can be found in the surface, as visible in the picture. AFM-measured RMS roughness takes a value of 3.37 nm. AFM image shown in Fig. 4.54 (a) exhibits the presence of small droplets on the sample surface. The droplets were also found on the surface of Ge:Te specimen grown with the TGF value of 2000 sccm, resolved in Fig. 4.47 and Fig. 4.48. The height profile over few droplets is drawn in Fig. 4.54 (b). Observed drops are up to $\sim$ 3.5 nm high and around 13 nm in diameter – measured as FWHM of peaks from height profile. Using the *in situ* reflectance, the thickness of grown Ge film is estimated to be about 200 nm, which is 30 nm more than in the case of the sample grown with the TGF of 2000 sccm.

XRD was utilized for characterization of Ge:Te sample grown with the TGF value of 1500 sccm. The results are displayed in Fig. 4.55. The graph in (a) shows a rocking curve scan recorded around the (111) reflection of Ge. The measurement shows a sharp peak with a FWHM of only 91.69 arcsec, which is almost 14 times less than in the case of Te-doped Ge grown with the TGF value of 2000 sccm. Shown in Fig. 4.55 (b), the RSM measured around Ge(133) reflex indicates that the deposited layer is fully relaxed. The position of the Ge(133) peak in the reciprocal coordinates is $(q_{\parallel},\ q_{\perp}) = (2.885258\ \mathrm{nm}^{-1},\ 7.140068\ \mathrm{nm}^{-1})$, which corresponds to the lattice constant of $a \approxeq 5.6602$ Å, calculated according to the Eq. 4.8.

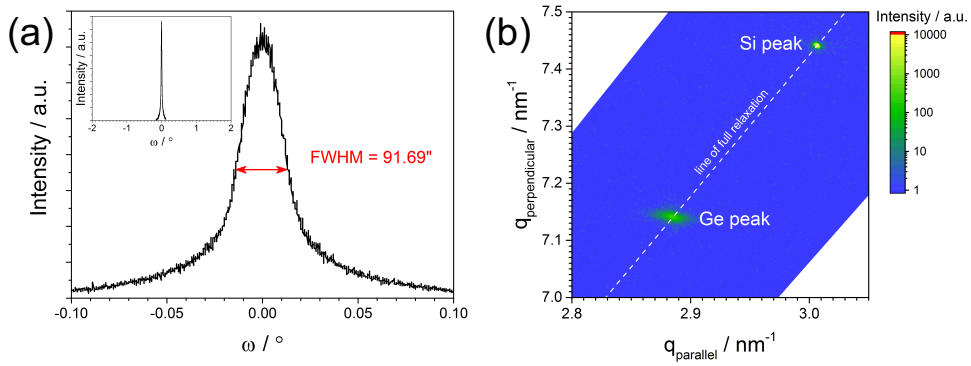

Figure 4.55: XRD characterization of the Ge:Te sample grown with the TGF of 1500 sccm: (a) rocking curve (ω-scan) measurements around Ge(111) reflex – inset shows the same data plotted in the scale used in Fig. 4.50 (b) and (c), for direct comparison; and (b) RSM recorded around (133) reflection of Ge.

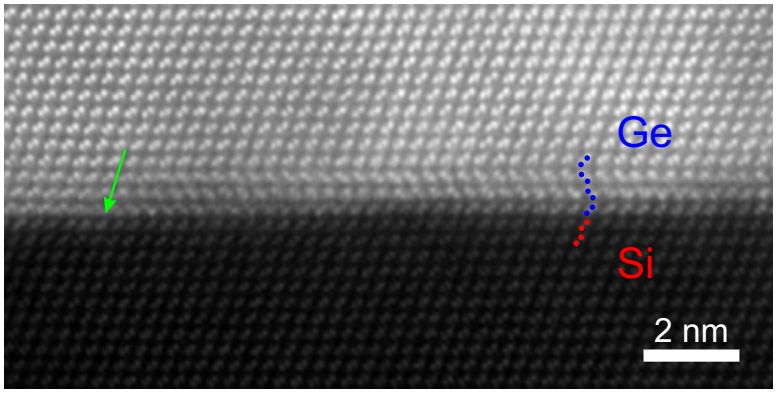

Figure 4.56: HAADF-STEM micrograph of the Ge/Si interface in the Ge:Te layer grown on Si(111) substrate with TGF value of 1500 sccm. The green arrow marks the edge dislocation at the interface. Blue and red dots denote stacking faults by marking the positions of Ge and Si atoms, respectively. Image is projected along $[0\bar{1}1]_{\mathrm{Si}}$.

Also, HAADF-STEM characterization of the sample was carried out. The micrograph projected along $[0\bar{1}1]_{\mathrm{Si}}$ direction around the Ge/Si interface is depicted in Fig. 4.56. Noise reduction in the image was proceeded using a nonlinear filtering algorithm [106]. The measurement resolves edge dislocations at the Ge/Si interface, as marked with a green arrow in the picture. An average dislocation separation was obtained after study of axial strain field map using GPA - geometrical phase analysis software [107], which utilizes the model published in [108]. The separation is found to be ~ 8.3 nm, which is consistent with a theoretical estimation. The atomic columns spacings in (111) crystallographic plane along the $\langle 211 \rangle$ direction equals $d_{Si} \approx 0.3326$ nm and $d_{Ge} \approx 0.3465$ nm for Si and Ge, respectively. Therefore, assuming that for strain relaxation each n planes of Ge there has to be one extra plane of Si

$$n \cdot d_{Ge} = (n+1) \cdot d_{Si}, \tag{4.9}$$

one finds that $n \cong 24$, and $n \cdot d_{Ge} \approx 8.32$ nm.

The presence of stacking faults in Ge:Te layer deposited with the TGF value of 1500 sccm is also resolved in the HAADF-STEM image. The stacking faults are often found in the first three layers of Ge-Ge dumbbells (bilayers of Ge). An example of stacking faults is displayed in Fig. 4.56 with blue and red dots, representing Ge and Si atoms. However, the blue and green dots solely represent one stacking fault as an example, and the HAADF-STEM image contains quite a number of these defects.

This study on the deposition of GeTe and Te-doped Ge via MOVPE made it possible to grow coalesced and highly crystalline Ge:Te layers on the Si(111) substrate. Te atoms are incorporated in the grown Ge at the concentration level below one atomic percent (determined with EDX, SIMS, and APT), which correspond to a doping level of $\sim 10^{20}$ cm^{-3}. Detailed XRD characterization reveals full relaxation of the Ge films with the lattice constant of about 5.66 Å. Reduction of the TGF value in the reactor during deposition results in an improvement of the epitaxial material crystallinity, however at the same time nanometer-size openings in the film are formed. Moreover, small droplets of a material are found on the sample surface, resolved in SEM and AFM images, regardless of the applied TGF value in the reactor during deposition. The grown material is mostly crystalline, but an amorphous region was observed with HAADF-STEM directly under the top surface of the specimen grown with the TGF value of 2000 sccm. HAADF-STEM characterization of Ge:Te sample grown with the TGF value of 1500 sccm exhibits the presence of edge dislocations and stacking faults close to the Ge/Si interface.

4.5 Electrical characterization

Layer-growth conditions for $Ge_1Sb_2Te_4$, Sb_2Te_3, and Te-doped Ge were established and discussed in the previous sections. Electrical characteristics of those materials were determined utilizing Hall effect measurements, conducted with LakeShore Cryotronics 8400 Series setup. For the experiment, 10 nm Ti followed by 200 nm Al contacts were evaporated in the corners of 7×7 mm^2 samples – van der Pauw geometry. Each single contact was triangular in shape, with the area of approximately 0.5 mm^2.

All investigated films were grown on a highly-resistive Si(111) substrate ($\rho > 1000\ \Omega \cdot$ cm) using optimized growth conditions for each of the materials. A quarter of 2 inch wafer used for deposition was cleaned chemically prior to the epitaxy according to the procedure described in subsection 3.1.4. Every growth run started with annealing of the substrate for 30 min at 690 °C in H_2 atmosphere. DETe was injected into the reactor in the last 2 min of the annealing step. For all samples, the reactor total pressure was kept at 50 mbar over the whole epitaxy run. Further growth details of the examined materials are given below, at the beginning of each adequate subsection.

4.5.1 $Ge_1Sb_2Te_4$

The characterized sample was grown for 60 min, which resulted in a ∼ 80 nm thick film. Right before the deposition of the $Ge_1Sb_2Te_4$ layer, the Si(111) substrate was pretreated for 2 min with Ge_2H_6 and TESb. The growth temperature was set to 475 °C and the TGF value to 3000 sccm. The partial pressures used for precursors were those listed in Tab. 4.1.

The material is deposited in a stable hexagonal phase. The temperature dependence of resistivity measured in the range of 15-300 K is displayed in Fig. 4.57 (a). The dependence reveals a metallic behavior of the grown $Ge_1Sb_2Te_4$ film with a residual resistivity at zero temperature. Experimental results were fitted with the Bloch-Grüneisen formula [109]

$$\rho(T) = \rho(0) + A\left(\frac{T}{\Theta_D}\right)^5 \int_0^{T/\Theta_D} \frac{t^5}{(e^t-1)(1-e^{-t})}dt, \tag{4.10}$$

where ρ stays for resistivity, T for temperature, Θ_D for Debye temperature, and A is material characteristic constant. The fit exposes increase of the resistivity due to electron-phonon scattering. Extracted from the Bloch-Grüneisen expression residual resistivity takes a value of 64.1 μΩ·cm, the constant A is 225 μΩ·cm, and the Debye temperature Θ_D = 155 K, which is comparable with values measured for sputtered $Ge_1Sb_2Te_4$ films [110].

The Hall effect measurement indicates p-type conductivity, which is due to the high number of Ge/Sb vacancies in the material, see Tab. 2.2. The measured Hall voltage changes linearly with applied magnetic field in the range of ±1 T at all tested temperatures from 15 K to 300 K. The Hall coefficient R_H and carrier concentration $p = 1/(qR_H)$, where q is elementary charge, are plotted in Fig. 4.57 (b) – blue and red curve, respectively. The experiment was carried out in a magnetic field of 1 T and with an electrical current of 1 mA. The Hall coefficient exhibits an unusual tendency – it is increasing with the temperature, in the range of 15-230 K. This results in unexpected decrease of carrier

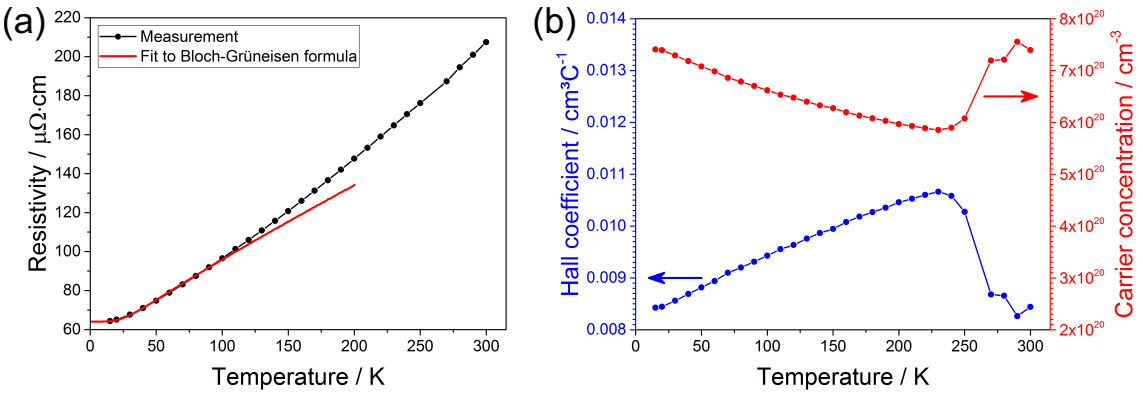

Figure 4.57: Electrical characterization of $Ge_1Sb_2Te_4$ layer: (a) measured resistivity and fit to the Bloch-Grüneisen formula (red line); and (b) the Hall coefficient (blue) and carrier concentration (red).

concentration with the increase of the temperature. However, the change of carrier density is not significant and its order of magnitude does not change over the whole examined temperature range. Alike behavior has been reported for Sb_2Te_3 films and explained by a temperature-dependent Hall-scattering factor [111]. A similar dependence of the Hall coefficient (carrier concentration) on the measurement temperature has also been published for GST compounds [110, 112] and highly doped Ge [113]. Taking into account the temperature-dependent Hall-scattering factor, the relation between Hall coefficient and carrier concentration is expressed with

$$R_H(p(T)) = \frac{r(T)}{qp(T)}, \tag{4.11}$$

where $r(T)$ represents the temperature-dependent Hall-scattering factor, which in discussed measurement was assumed to be equal to 1. Thus, it is believed that the carrier concentration is rather constant over the considered temperatures. Also, no freeze-out region is observed in the graph presenting carrier density dependence on the temperature, Fig. 4.57 (b). This is because $Ge_1Sb_2Te_4$ is an alloy with a narrow band gap [19–21] and the deposited material is degenerated, having a high hole concentration of $7.4{\cdot}10^{20}$ cm^{-3} at room temperature. Even at low temperatures approaching 0 K, the Fermi level is situated in the valance band, and there are free carriers present in the system. It stays discursive, whether the increase of the carrier density for temperatures over 230 K is due to the temperature-dependence of the Hall-scattering factor or, perhaps, thermal generation of intrinsic carriers starts to prevail in this region.

Fig. 4.58 (a) shows the measured Hall mobility $\mu_H = R_H/\rho$ (black curve) in a function of the temperature – both axes of the graph are in logarithmic scale. For temperatures higher than 230 K, the mobility follows a $T^{-1.96}$ dependence – red line in the plot. Below 230 K, the change in mobility is proportional to $T^{-0.49}$ – blue line. At low temperatures of 30 K and less, the reduction of the Hall mobility is not observed, but rather stabilization at certain level. The mobility is nearly temperature independent in this region, which suggests that the scattering from lattice defect predominates [109]. All in all, a mixed scattering mechanism for charge carriers is presumed, which can be described with formula

$$\mu^{-1} = \mu_d^{-1} + \mu_{ph}^{-1}, \tag{4.12}$$

where μ_d and μ_{ph} are the mobilities corresponding to scattering of carriers with lattice defects and acoustic phonons, respectively. Scattering from lattice defects is temperature independent and results in residual resistivity, which was found by fitting the temperature dependence of the resistivity with the Bloch-Grüneisen formula. Therefore, by subtracting the residual resistivity from the experimental data, one can determine the temperature-dependent part of the mobility contribution $\mu_{ph}(T)$. Moreover, since the unusual decrease of the carrier concentration with the temperature was connected to the variation of the

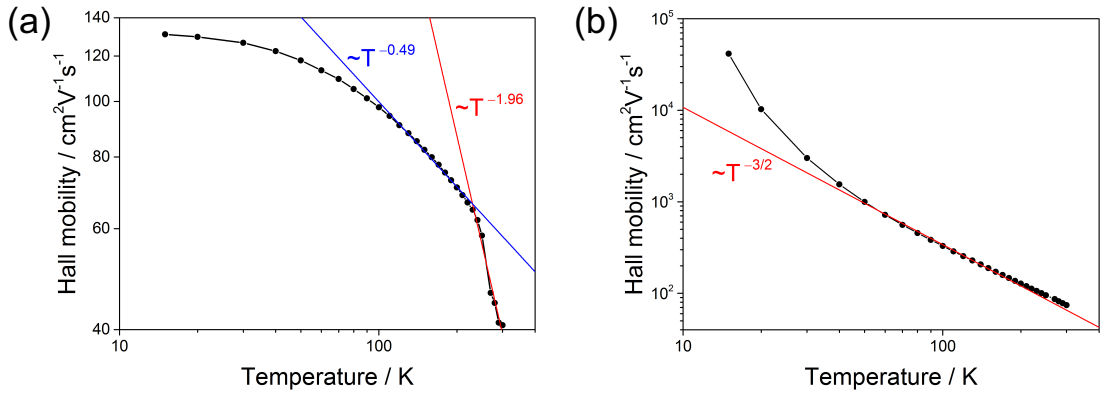

Figure 4.58: Hall mobility of holes in $Ge_1Sb_2Te_4$: (a) as measured, blue and red lines show fits to experimental points in the ranges of 110-220 K and 230-300 K, respectively; (b) temperature-dependent part of mobility μ_{ph} calculated assuming constant hole concentration $p(T = 230K) \approxeq 5.85 \cdot 10^{20}$ cm^{-3}, red line shows the theoretical dependence indicating scattering from acoustic phonons.

Table 4.11: Carrier concentration, resistivity, and Hall mobility of holes in $Ge_1Sb_2Te_4$ at 300 K. Results from this work are compared with values from the literature.

Method	p / cm^{-3}	ρ / μΩ·cm	μ_H / cm^{2}V^{-1}s^{-1}	**Ref.**
MOVPE	$7.4 \cdot 10^{20}$	207	40.7	This work
Sputtering	$2.2 \cdot 10^{20}$	1040	27.5	[26]
Sputtering	$1.9 \cdot 10^{20}$	557	59.0	[110]
Melt. el. mix.	$2.6 \cdot 10^{20}$	444	54.0	[115]

Hall-scattering factor, the mobility should be corrected and calculated for a constant carrier density. The final equation describing the temperature-dependent part of the mobility has a form

$$\mu_{ph}(T) = \frac{1}{qp[\rho(T) - \rho(0)]}. \tag{4.13}$$

The mobility was recalculated assuming constant $p(T = 230K) \approxeq 5.85 \cdot 10^{20}$ cm^{-3} – the minimal value reached by the carrier concentration, before it changes the trend and starts to grow with the temperature. The result is plotted in Fig. 4.58 (b). Above 50 K, the curve follows the theoretically-predicted reduction of mobility with temperature due to scattering from acoustic phonons, which is described by a $T^{-3/2}$ rule [114] and drawn with red line in the figure. Thus, it is expected that scattering from phonons dominates in the material in this temperature range.

Tab. 4.11 presents the carrier concentration, the resistivity, and the Hall mobility measured within the scope of this thesis for MOVPE-grown $Ge_1Sb_2Te_4$ layers, and compares the results with values reported in the literature for samples deposited via sputter-

ing [26, 110] and prepared by melting elemental mixture [115]. The MOVPE specimen exhibits the highest carrier density and the lowest resistivity. Nevertheless, the carrier concentration is in the same order of magnitude as for specimens produced with other methods. The measured Hall mobility of 40.7 $cm^2V^{-1}s^{-1}$ is a middle value between results taken from references, which differ by a factor of ~ 2.

4.5.2 Sb_2Te_3

The examined Sb_2Te_3 layer was deposited for 40 min on the Si(111) substrate pretreated for 2 min with Ge_2H_6 and TESb before the growth. The thickness of the grown film is around 300 nm. The growth temperature was set to 475 °C and the TGF value to 3000 sccm – the same as in the case of $Ge_1Sb_2Te_4$ samples. The VI/V precursors partial pressures ratio of 6 was applied, and partial pressures as given in Tab. 4.6 were utilized during the growth.

The Hall effect reveals linear dependence of Hall voltage in examined Sb_2Te_3 film on magnetic field in the range of ±1 T, and *p*-type conductivity, which is due to intrinsic defects – Sb vacancies and Sb_{Te} antisites [116, 117]. The experiments were carried out at temperatures from 10 K to 300 K. The results discussed below were received utilizing 500 µA excitation current and a magnetic field of 1 T.

The variation of the resistivity with the temperature is presented in Fig. 4.59 (a) and exhibits metallic behavior. The experimental points were fitted with the Bloch-Grüneisen function (Eq. 4.10) plotted with red line in the chart. The fit resolves a residual resistivity of 51.3 µΩ·cm and a Debye temperature $\Theta_D = 160$ K, consistent with values reported in the literature [118, 119]. The factor A is found to be 300 µΩ·cm.

Similarly like for $Ge_1Sb_2Te_4$, the measured Hall coefficient increases and the carrier concentration decreases with temperature – the dependencies are exposed in Fig. 4.59 (b). Such variation of the parameters has been reported earlier for Sb_2Te_3 [111], and as al-

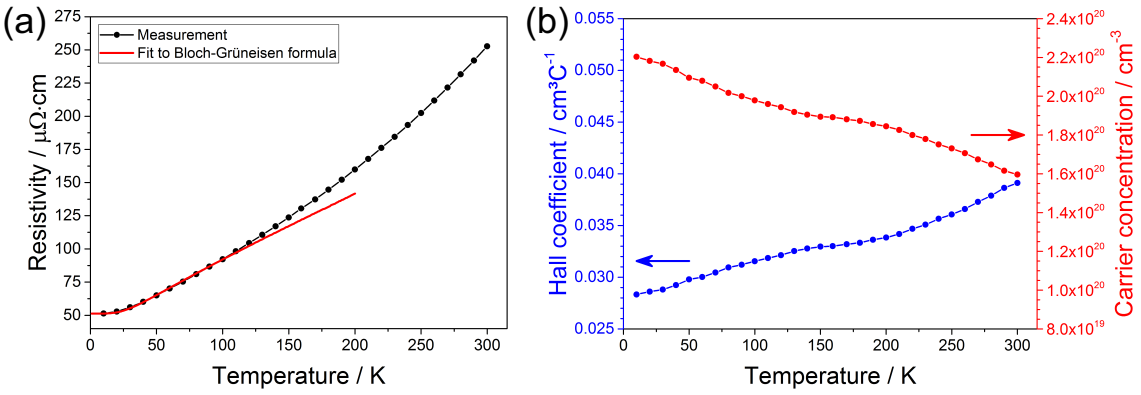

Figure 4.59: Electrical characterization of Sb_2Te_3 film: (a) measured resistivity and fit to the Bloch-Grüneisen formula (red line); and (b) the Hall coefficient (blue) and carrier concentration (red).

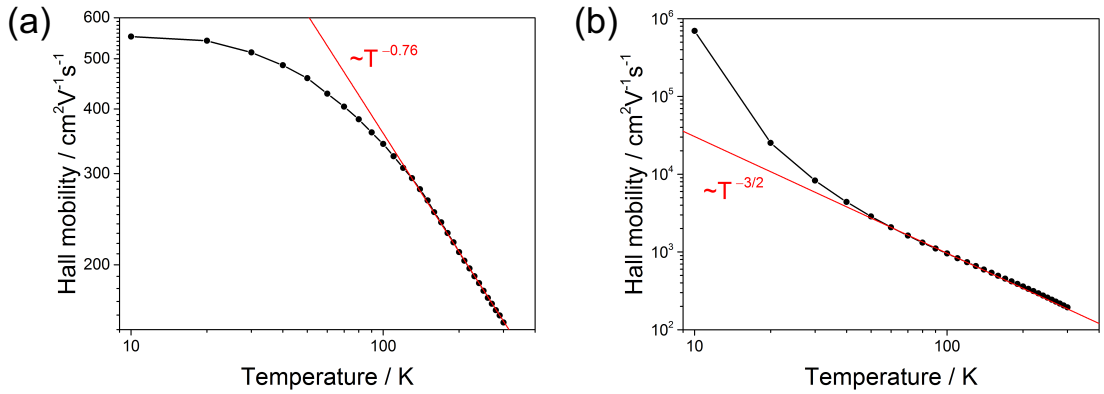

Figure 4.60: Hall mobility of holes in Sb_2Te_3: (a) as measured, red line shows fit to experimental points in the range of 110-220 K; (b) temperature-dependent part of mobility μ_{ph} calculated assuming constant hole concentration $p(T = 300K) \approxeq 5.85 \cdot 10^{20}$ cm^{-3}, red line shows the theoretical dependence indicating scattering from acoustic phonons.

Table 4.12: Carrier concentration, resistivity, and Hall mobility of holes in Sb_2Te_3 at 300 K. Results reported in this work are compared with values from the literature.

Method	p / cm^{-3}	ρ / μΩ·cm	μ_H / cm^{2}V^{-1}s^{-1}	**Ref.**
MOVPE	$1.6 \cdot 10^{20}$	253	154.8	This work
MOVPE	$2.0 \cdot 10^{20}$	250	130.0	[65]
MBE	$2.6 \cdot 10^{19}$	590	402.0	[120]
ALD	$2.4 \cdot 10^{18}$	96	270.5	[111]

ready mentioned, this is due to the temperature-dependent Hall-scattering factor. Therefore, while analyzing the Hall mobility and determining the scattering mechanism, analogous calculations and steps were utilized as described in the previous subsection about $Ge_1Sb_2Te_4$. The measured mobility is shown in Fig. 4.60 (a). The mobility is nearly temperature-independent at 10-20 K. At higher temperatures, the variation $\sim T^{-0.76}$ (red line in the graph) suggests a mixed scattering mechanism. Fig. 4.60 (b) presents the temperature-dependent part of the Hall mobility calculated according to the Eq. 4.13 for constant $p(T = 300K) \approxeq 1.6 \cdot 10^{20}$ cm^{-3} and $\rho(0) = 51.3$ μΩ·cm, as indicated from fit to the Bloch-Grüneisen formula. From 50 K up, the mobility μ_{ph} is proportional to $T^{-3/2}$, which reveals that scattering from acoustic phonons predominates in this temperature region.

In Tab. 4.12, the electrical characteristics of Sb_2Te_3 obtained in the frame of this work are compared with values published in the literature for material deposited via MOVPE [65], MBE [120], and atomic layer deposition (ALD) [111]. The electrical properties of MOVPE-grown Sb_2Te_3 reported here are comparable with values given in the literature for films produced with the same method. The material deposited by MBE at

room temperature is characterized with an order of magnitude lower carrier density, higher resistivity, and with also higher mobility. The ALD sample exhibits the lowest carrier concentration and resistivity, out of compared here, and a relatively high mobility. High hole density in MOVPE deposited Sb_2Te_3 indicates higher concentration of point defects, Sb vacancies or Sb_{Te} antisites, compared to samples obtained with other methods. In case of the specimen described in this thesis, the carrier density could also be increased by contamination with Ge acceptors, since Ge_2H_6 is used in the Si(111) substrate pretreatment step prior to the Sb_2Te_3 layer epitaxy.

4.5.3 Te-doped Ge

For Te-doped Ge, the Hall effect was measured on a $\sim$ 173 nm thick film grown in 40 min. No additional substrate pretreatment was applied prior to the growth except for the high-temperature annealing. The temperature of 450 °C was set for the substrate during the growth, and the TGF was kept at 1500 sccm. Partial pressures of $1.33 \cdot 10^{-2}$ were utilized for Ge_2H_6 and DETe during the deposition, resulting in the VI/IV ratio of 1.0.

The electrical characterization of the Ge:Te film was done at room temperature. The Hall effect measurement was proceeded in a magnetic field of 1 T utilizing an electrical current of 100 µA. The Hall voltage was checked to be linearly dependent on a magnetic field varying in the range of ±1 T. The experiment reveals *n*-type conductivity of the material. The conductivity type is consistent with the expectation since Ge is highly doped with Te, which acts as a donor with two extra valence electrons while compared to the Ge atom. The Te doping concentration is estimated to be at the level of $\sim 10^{20}$ cm^{-3}, however the measured carrier concentration is equal to $n \approxeq 3.8 \cdot 10^{18}$ cm^{-3} – two order of magnitude less. Therefore, not all donors are electrically active. The observed effect of the reduced electrical activation of donors in Ge is known and has already been reported for doping with group-V elements [121]. Donors with vacancies in Ge crystal can create electrically inactive pairs, which results in the removal of electrons from the conduction

Table 4.13: Carrier concentration, resistivity, and mobility of charge carriers in Ge at 300 K. Results from this work are compared with values reported in the literature for *n*-type Ge(100) [121, 124] and for intrinsic Ge crystal [113] (crystal orientation not specified in the reference).

Dopant	**n / cm^{-3}**	**ρ / mΩ·cm**	**μ / cm^{2}V^{-1}s^{-1}**	**Ref.**
Te (*n*-type)	$3.8 \cdot 10^{18}$	15.4	107.2	This work
Sb (*n*-type)	$6.5 \cdot 10^{17}$	8.8	1103.8	[121, 124]
P (*n*-type)	$4.0 \cdot 10^{19}$	0.7	224.8	[121, 124]
Intrinsic (*p*-type)	$2.5 \cdot 10^{13}$	47000.0	5312.5	[113]

band [122, 123]. The effect could occur in Te-doped Ge.

The resistivity of the examined Ge:Te layer was found to be 15.4 mΩ·cm at room temperature. The measurement resulted in an electron Hall mobility of 107.2 $cm^2V^{-1}s^{-1}$. The electrical characteristics are presented in Tab. 4.13, which also compares the result with parameters published in the literature for *n*-type Ge(100) [121, 124] and for intrinsic Ge crystal [113]. MOVPE-grown Ge:Te is characterized by a relatively low resistivity, and at the same time with the lowest charge carrier mobility, out of compared here results. The carrier concentration is rather high, however higher values have earlier been reported in the literature.

Chapter 5

Conclusion and outlook

5.1 Conclusion

Alloys along the GeTe-Sb_2Te_3 pseudo-binary line possess unique properties classifying them as a PCMs and promising candidate for next generation of PRAM: reversible transition between amorphous and crystalline state, contrast in the optical and electrical characteristics of these two phases, and long-term stability of states. Moreover, many of the GST alloys in their stable phase show significant structural similarities to so-called iPCMs – GeTe/Sb_2Te_3 superlattices characterized by energy-efficient phase switching, of which mechanism stays under discussion. Therefore, it is expected that the alloys from the pseudo-binary GeTe-Sb_2Te_3 line could exhibit similar behavior, and except technological applications, serve as a model material for better understanding of the physics behind the iPCM switching. The work presented in this thesis focuses on the optimization of MOVPE growth conditions towards deposition of highly crystalline layers of the materials from the GST system.

At first, the epitaxy process of $Ge_1Sb_2Te_4$ was explored extensively with respect to pre-annealing conditions of the Si(111) substrate, TGF value in the reactor during growth, and deposition temperature. It is found, that the presence of Te in high-temperature annealing step prior to GST growth is essential for the deposition of fully coalesced and uniform layers of the material. Te seems to saturate Si dangling bonds and support the vdW epitaxy. The deposition of the GST compounds proceeds in the kinetic-controlled growth regime, while utilizing Ge_2H_6, TESb, and DETe as sources. The kinetic-controlled growth regime is the consequence of TESb and DETe decomposition processes. Therefore, variation of the TGF value during epitaxy leads to a change of the growth rate, which subsequently affects the layer crystallinity. XRD ϕ-scan characterization reveals presence of rotational twin domains in films deposited with higher rates (lower TGF values). Increase of the TGF value and reduction of the growth rate suppresses one of the twin domains. The (107) reflections of remaining $Ge_1Sb_2Te_4$ domain are collinear with Si(220) reflexes. The observation is opposite to MBE-grown samples, where collinearity with Si(311) reflexes is preferred [94,

95]. The contrast between MOVPE and MBE samples is possible to be explained with a simple model treating elements of GST layer and Si substrate as indistinguishable points interacting via vdW forces. The model suggests that the difference between the samples grown via MOVPE and MBE is due to various position of the nucleation centers for GST twins on the Si(111) substrate. The substrate temperature during the deposition of GST influences mainly the composition and slightly the morphology of grown layer. Since the growth proceeds in the kinetic-controlled regime, the decrease of the temperature reduces the amount of Te and Sb on the substrate. This has an effect on the layer coalescence and increases Ge incorporation in the film. On the other hand, increase of the growth temperature reduces the Ge content. All in all, the temperature of 475 °C is found to be the optimal for the deposition of $Ge_1Sb_2Te_4$ layers on the Si(111) substrate.

The second part of the thesis is focused on the deposition of Sb_2Te_3, GeTe, and Te-doped Ge. The VI/V ratio $R_{VI/V} = 6.0$ is found to be optimal for deposition of fully coalesced and uniform Sb_2Te_3 layers. The ratio is lower compared to the one used for the growth of $Ge_1Sb_2Te_4$ and is achieved by the increase of TESb partial pressure. Therefore, the growth rate of Sb_2Te_3 is higher and 40 min deposition results in around 300 nm thick layer. The adjustment of the substrate temperature once again reveals the kinetic-controlled nature of the epitaxy. The growth rate of the material changes with the temperature and varies proportionally to the calculated change of the decomposed precursors fraction. The temperature of 475 °C seems to be optimal for the growth of Sb_2Te_3. At lower temperatures the layer loses coalescence, while at higher it cracks. Also, 2 min Si(111) substrate pretreatment with Ge_2H_6 and TESb is mandatory for the deposition of coalesced and uniform layers, as in the case of $Ge_1Sb_2Te_4$. Digermane seems to affect the substrate coverage while DETe improves the deposited layer morphology and uniformity.

Layer deposition of GeTe by MOVPE, using Ge_2H_6 and DETe as precursors, remains a challenge. Only islands growth is achieved, although many growth parameters were investigated. Approach to use catalytic properties of Sb, leads to deposition of GST alloys, already at low partial pressure of TESb applied. The growth temperature of 450 °C and the TGF value of 1500 sccm give the highest density of GeTe crystals deposited on Si substrate. Reduction of the VI/IV ratio $R_{VI/IV}$, from the value of 10.0 to 1.0, resulted in the conversion of deposited material from GeTe islands to Te-doped coalesced Ge layer. Utilizing the ratio $R_{VI/IV} = 1.0$, the Te content in Ge layer is on the level of 3-8 ‰. After 40 min deposition the film is about 173 nm thick and fully relaxed, as indicated with XRD measurements. The doping with Te strongly improves the Ge layer morphology, reducing RMS roughness more than 10 times. However, nanometer-size droplets are resolved on the surface of the Ge:Te layer in AFM micrographs.

In the end, the electrical characteristics of coalesced $Ge_1Sb_2Te_4$, Sb_2Te_3, and Ge:Te layers deposited via MOVPE were determined with the Hall effect measurement. $Ge_1Sb_2Te_4$ and Sb_2Te_3 are showing metallic behavior of resistivity with the temperature and p-type conductivity. The materials are degenerated semiconductors and the carrier concentration

seems to be independent on the temperature in the range of 10-300 K. The scattering of charge carriers is dominated with crystal defects at low temperatures and with acoustic phonons at temperatures above $\sim$ 50 K. The third material, Te-doped Ge was characterized only at room temperature. As expected, the layer exhibits n-type conductivity, since Te acts as a donor in Ge. However, the doping is estimated at the level of $\sim 10^{20}$ cm^{-3} and the measured carrier density is two orders of magnitude lower, $n = 3.8 \cdot 10^{18}$ cm^{-3}. The discrepancy is probably due to electrically inactive pairs of vacancies and donors, which are known to be created in n-type Ge [121].

5.2 Outlook

The beauty of science is that it is a never-ending journey. Presented in this thesis results give significant input into the field of PCMs and understanding of GST compounds deposition via MOVPE. Nevertheless, there is still plenty to do for the future generations of doctoral researchers and scientists. Some of the steps towards further development of the research area have already been done and are shortly presented below, together with the author's perspective for the future.

The optimal growth conditions for Sb_2Te_3 and GeTe layer were searched for the purpose of heterostructure deposition, motivated by the unique phase-switching properties of the iPCM superlattices. Possibility to grow iPCM structures via MOVPE would be attractive for technology due to the industrial relevance of the method. While layer-growth conditions for Sb_2Te_3 were established, the deposition of GeTe in layer mode remains a challenge. Nevertheless, the first try for MOVPE deposition of Sb_2Te_3/GeTe heterostructure was given. Around 300 nm thick Sb_2Te_3 layer was grown in 40 min on the Si(111) substrate utilizing the optimal growth conditions discussed in section 4.3. Next, a 2 min interruption in precursors supply was introduced and the substrate temperature was reduced from 475 °C to 450 °C. The carrier gas flow was preserved during the temperature reduction step. After 2 min, when the temperature stabilized, GeTe was deposited for 40 min. The precursor partial pressures of $1.33 \cdot 10^{-2}$ mbar and $1.33 \cdot 10^{-1}$ mbar were used for Ge_2H_6 and DETe, respectively. During GeTe growth, the TGF value in the reactor was set to 1500 sccm.

The result of epitaxial run aiming to deposit the GeTe/Sb_2Te_3 heterostructure is presented in Fig. 5.1. Image (a) shows SEM micrograph of the sample surface. A lot of cracks and opening is found in the deposited layer. Fig. 5.1 (b) presents XRD 2θ-θ scan of the specimen. The measurement reveals intermixing of the deposited materials since the reflexes of Sb_2Te_3, $Ge_1Sb_2Te_4$, and $Ge_2Sb_2Te_5$ are resolved in the graph. The GeTe-Sb_2Te_3 intermixing might be a bottleneck for the deposition of iPCM superlattices via MOVPE. A lot of effort has to be put, if one wants to achieve growth of high-quality structures with a sharp interfaces between the GeTe and Sb_2Te_3 layers. One of intuitive ways to go is a reduction of the growth temperature for GeTe. However, recent experiments do not

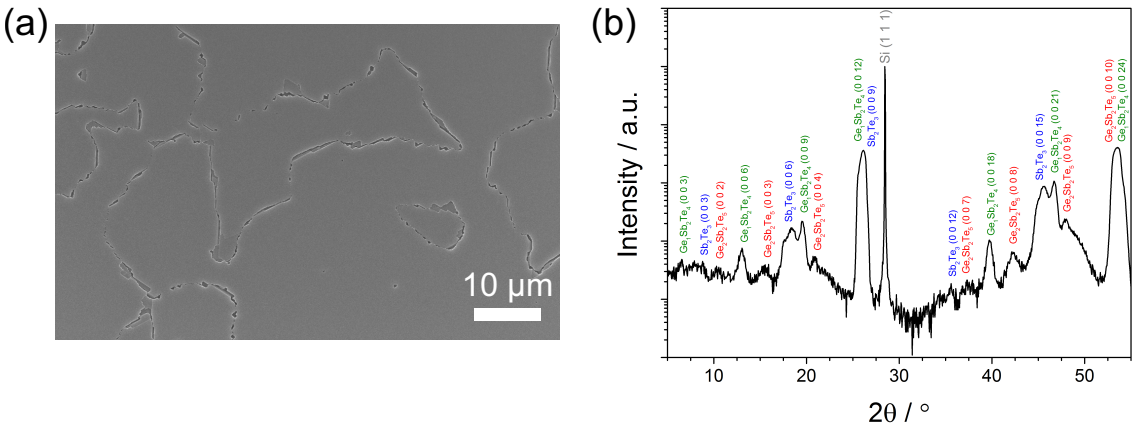

Figure 5.1: Characterization of MOVPE-grown GeTe/Sb_2Te_3 heterostructure: (a) SEM micrograph of the sample surface; and (b) XRD 2θ-θ scan of the specimen – reflections corresponding to Sb_2Te_3, $Ge_1Sb_2Te_4$, and $Ge_2Sb_2Te_5$ are marked with blue, green, and red labels, respectively.

give satisfying results and the materials mix even when the temperature is reduced to 400 °C. Further reduction of the temperature will slow down the growth rate or even stop the deposition since the epitaxy proceeds in the kinetic-controlled growth regime and only a fraction of precursors is decomposed at applied temperatures. Therefore, it seems that better and more reasonable direction for research in the field of PCMs is further work on the deposition of GST alloys. This thesis reported growth condition ensuring repeatable epitaxy of fully coalesced and uniform $Ge_1Sb_2Te_4$ layers. Growth conditions for other compounds from the pseudo-binary GeTe-Sb_2Te_3 line are still to be found. Various GST alloys should be investigated with respect to their switching properties. Perhaps one day, with a bit of luck and a lot of work done in laboratories, energy-efficient field-induced switching will be observed in MOVPE-deposited GST alloys.

Bibliography

[1] https://www.domo.com/learn/data-never-sleeps-6, "Data Never Sleeps 6.0," accessed May 27, 2018.

[2] T. Ohta, K. Nishiuchi, K. Narumi, Y. Kitaoka, H. Ishibashi, N. Yamada, and T. Kozaki, "Overview and the Future of Phase-Change Optical Disk Technology," *Japanese Journal of Applied Physics*, vol. 39, no. 2B, p. 770, 2000.

[3] R. E. Simpson, P. Fons, a. V. Kolobov, T. Fukaya, M. Krbal, T. Yagi, and J. Tominaga, "Interfacial phase-change memory," *Nature Nanotechnology*, vol. 6, p. 501, jul 2011.

[4] M. Schuck, S. Rieß, M. Schreiber, G. Mussler, D. Grützmacher, and H. Hardtdegen, "Metal organic vapor phase epitaxy of hexagonal Ge-Sb-Te (GST)," *Journal of Crystal Growth*, vol. 420, p. 37, 2015.

[5] A. Ratajczak, M. von der Ahe, H. Du, G. Mussler, and D. Grützmacher, "Metal organic vapor phase epitaxy of $Ge_1Sb_2Te_4$ thin films on Si(111) substrate," *Applied Physics A*, vol. 125, p. 163, 2019.

[6] M. Wuttig and N. Yamada, "Phase-change materials for rewriteable data storage," *Nature Materials*, vol. 6, no. 11, p. 824, 2007.

[7] D. Lencer, M. Salinga, B. Grabowski, T. Hickel, J. Neugebauer, and M. Wuttig, "A map for phase-change materials," *Nature Materials*, vol. 7, no. 12, p. 972, 2008.

[8] C. N. Afonso, J. Solis, F. Catalina, and C. Kalpouzos, "Ultrafast reversible phase change in GeSb films for erasable optical storage," *Applied Physics Letters*, vol. 60, no. 25, p. 3123, 1992.

[9] H. Iwasaki, Y. Ide, M. Harigaya, Y. Kageyama, and I. Fujimura, "Completely erasable phase change optical disk," *Japanese Journal of Applied Physics*, vol. 31, no. 2B, p. 461, 1992.

[10] H. Iwasaki, M. Harigaya, O. Nonoyama, Y. Kageyama, M. Takahashi, K. Yamada, H. Deguchi, and Y. Ide, "Completely Erasable Phase Change Optical Disc II: Application of Ag-In-Sb-Te Mixed-Phase System for Rewritable Compact Disc Com-

patible with CD-Velocity and Double CD-Velocity," *Japanese Journal of Applied Physics*, vol. 32, no. 11B, p. 5241, 1993.

[11] T. Kato, H. Hirata, T. Komaki, H. Inoue, H. Shingai, N. Hayashida, and H. Utsunomiya, "The phase change optical disc with the data recording rate of 140 Mbps," *Japanese Journal of Applied Physics*, vol. 41, no. 3B, p. 1664, 2002.

[12] T. Nonaka, G. Ohbayashi, Y. Toriumi, Y. Mori, and H. Hashimoto, "Crystal structure of GeTe and $Ge_2Sb_2Te_5$ meta-stable phase," *Thin Solid Films*, vol. 370, no. 1, p. 258, 2000.

[13] T. Matsunaga and N. Yamada, "Structural investigation of $GeSb_2Te_4$: A high-speed phase-change material," *Physical Review B*, vol. 69, no. 10, p. 104111, 2004.

[14] J. L. F. Da Silva, A. Walsh, and H. Lee, "Insights into the structure of the stable and metastable $(GeTe)_m(Sb_2Te_3)_n$ compounds," *Physical Review B*, vol. 78, no. 22, p. 224111, 2008.

[15] J. E. Boschker and R. Calarco, "Growth of crystalline phase change materials by physical deposition methods," *Advances in Physics: X*, vol. 2, no. 3, p. 675, 2017.

[16] M. Luo and M. Wuttig, "The Dependence of Crystal Structure of Te-Based Phase-Change Materials on the Number of Valence Electrons," *Advanced Materials*, vol. 16, no. 5, p. 439, 2004.

[17] G. Lucovsky and R. M. White, "Effects of Resonance Bonding on the Properties of Crystalline and Amorphous Semiconductors," *Physical Review B*, vol. 8, no. 2, p. 660, 1973.

[18] E. Talebian and M. Talebian, "A general review on the derivation of Clausius-Mossotti relation," *Optik*, vol. 124, no. 16, p. 2324, 2013.

[19] J. W. Park, S. H. Baek, T. D. Kang, H. Lee, Y. S. Kang, T. Y. Lee, D. S. Suh, K. J. Kim, C. K. Kim, Y. H. Khang, J. L. F. Da Silva, and S. H. Wei, "Optical properties of (GeTe, Sb_2Te_3) pseudobinary thin films studied with spectroscopic ellipsometry," *Applied Physics Letters*, vol. 93, no. 2, p. 021914, 2008.

[20] K. Shportko, S. Kremers, M. Woda, D. Lencer, J. Robertson, and M. Wuttig, "Resonant bonding in crystalline phase-change materials," *Nature Materials*, vol. 7, no. 8, p. 653, 2008.

[21] D. Subramaniam, C. Pauly, M. Liebmann, M. Woda, P. Rausch, P. Merkelbach, M. Wuttig, and M. Morgenstern, "Scanning tunneling microscopy and spectroscopy of the phase change alloy $Ge_1Sb_2Te_4$," *Applied Physics Letters*, vol. 95, no. 10, p. 103110, 2009.

[22] T. Kato and K. Tanaka, "Electronic Properties of Amorphous and Crystalline $Ge_2Sb_2Te_5$ Films," *Japanese Journal of Applied Physics*, vol. 44, no. 10, p. 7340, 2005.

[23] Y. Kim, K. Jeong, M. H. Cho, U. Hwang, H. S. Jeong, and K. Kim, "Changes in the electronic structures and optical band gap of $Ge_2Sb_2Te_5$ and N-doped $Ge_2Sb_2Te_5$ during phase transition," *Applied Physics Letters*, vol. 90, no. 17, p. 171920, 2007.

[24] J. Orava, T. Wágner, J. Šik, J. Přikryl, M. Frumar, and L. Beneš, "Optical properties and phase change transition in $Ge_2Sb_2Te_5$ flash evaporated thin films studied by temperature dependent spectroscopic ellipsometry," *Journal of Applied Physics*, vol. 104, no. 4, p. 043523, 2008.

[25] A. Mendoza-Galván and J. González-Hernández, "Drude-like behavior of Ge:Sb:Te alloys in the infrared," *Journal of Applied Physics*, vol. 87, no. 2, p. 760, 2000.

[26] T. Siegrist, P. Jost, H. Volker, M. Woda, P. Merkelbach, C. Schlockermann, and M. Wuttig, "Disorder-induced localization in crystalline phase-change materials," *Nature Materials*, vol. 10, no. 3, p. 202, 2011.

[27] N. Yamada and T. Matsunaga, "Structure of laser-crystallized $Ge_2Sb_{2+x}Te_5$ sputtered thin films for use in optical memory," *Journal of Applied Physics*, vol. 88, no. 12, p. 7020, 2000.

[28] V. Bragaglia, B. Jenichen, A. Giussani, K. Perumal, H. Riechert, and R. Calarco, "Structural change upon annealing of amorphous GeSbTe grown on Si(111)," *Journal of Applied Physics*, vol. 116, no. 5, p. 054913, 2014.

[29] F. Katmis, R. Calarco, K. Perumal, P. Rodenbach, A. Giussani, M. Hanke, A. Proessdorf, A. Trampert, F. Grosse, R. Shayduk, R. Campion, W. Braun, and H. Riechert, "Insight into the growth and control of single-crystal layers of Ge-Sb-Te phase-change material," *Crystal Growth and Design*, vol. 11, no. 10, p. 4606, 2011.

[30] T. Matsunaga, N. Yamada, and Y. Kubota, "Structures of stable and metastable $Ge_2Sb_2Te_5$, an intermetallic compound in GeTe–Sb_2Te_3 pseudobinary systems," *Acta Crystallographica*, vol. B60, no. 6, p. 685, 2004.

[31] H. Hardtdegen, S. Rieß, M. Schuck, K. Keller, P. Jost, H. Du, M. Bornhöfft, A. Schwedt, G. Mussler, M. v.d. Ahe, J. Mayer, G. Roth, D. Grützmacher, and M. Mikulics, "A model structure for interfacial phase change memories: Epitaxial trigonal $Ge_1Sb_2Te_4$," *Journal of Alloys and Compounds*, vol. 679, p. 285, 2016.

[32] http://www2.fiz karlsruhe.de/icsd_home.html, "ICSD - Inorganic Crystal Structure Database," accessed February 22, 2019.

[33] O. Karpinsky, L. Shelimova, M. Kretova, and J.-P. Fleurial, "An X-ray study of the mixed-layered compounds of $(GeTe)_n$ $(Sb_2Te_3)_m$ homologous series," *Journal of Alloys and Compounds*, vol. 268, no. 1-2, p. 112, 1998.

[34] S. R. Ovshinsky, "Reversible electrical switching phenomena in disordered structures," *Physical Review Letters*, vol. 21, no. 20, p. 1450, 1968.

[35] H.-S. Wong, S. Raoux, S. Kim, J. Liang, J. P. Reifenberg, B. Rajendran, M. Asheghi, and K. E. Goodson, "Phase Change Memory," *Proceedings of the IEEE*, vol. 98, no. 12, p. 2201, 2010.

[36] X. S. Miao, L. P. Shi, H. K. Lee, J. M. Li, R. Zhao, P. K. Tan, K. G. Lim, H. X. Yang, and T. C. Chong, "Temperature Dependence of Phase-Change Random Access Memory Cell," *Japanese Journal of Applied Physics*, vol. 45, no. 5A, p. 3955, 2006.

[37] F. Bedeschi, R. Bez, C. Boffino, E. Bonizzoni, E. Buda, G. Casagrande, L. Costa, M. Ferraro, R. Gastaldi, O. Khouri, F. Ottogalli, F. Pellizzer, A. Pirovano, C. Resta, G. Torelli, and M. Tosi, "4-Mb MOSFET-Selected μTrench Phase-Change Memory Experimental Chip," *IEEE Journal of Solid-State Circuits*, vol. 40, no. 7, p. 1557, 2005.

[38] Y. Choi, I. Song, M. H. Park, H. Chung, S. Chang, B. Cho, J. Kim, Y. Oh, D. Kwon, J. Sunwoo, J. Shin, Y. Rho, C. Lee, M. G. Kang, J. Lee, Y. Kwon, S. Kim, J. Kim, Y. J. Lee, Q. Wang, S. Cha, S. Ahn, H. Horii, J. Lee, K. Kim, H. Joo, K. Lee, Y. T. Lee, J. Yoo, and G. Jeong, "A 20nm 1.8V 8Gb PRAM with 40MB/s program bandwidth," in *2012 IEEE International Solid-State Circuits Conference*, p. 46, IEEE, 2012.

[39] V. Bragaglia, F. Arciprete, W. Zhang, A. M. Mio, E. Zallo, K. Perumal, A. Giussani, S. Cecchi, J. E. Boschker, H. Riechert, S. Privitera, E. Rimini, R. Mazzarello, and R. Calarco, "Metal - Insulator Transition Driven by Vacancy Ordering in GeSbTe Phase Change Materials.," *Scientific reports*, vol. 6, p. 23843, 2016.

[40] S. Sahu, S. K. Pandey, A. Manivannan, U. P. Deshpande, V. G. Sathe, V. R. Reddy, and M. Sevi, "Direct evidence for phase transition in thin $Ge_1Sb_4Te_7$ films using in situ UV-Vis-NIR spectroscopy and Raman scattering studies," *Physica Status Solidi B*, vol. 253, no. 6, p. 1069, 2016.

[41] T. Ohta, N. Yamada, H. Yamamoto, T. Mitsuyu, T. Kozaki, J. Qiu, and K. Hirao, "Progress of the Phase-change Optical Disk Memory," *Materials Research Society Symposium Proceedings*, vol. 674, no. 12, p. V1.1.1, 2001.

[42] S. Lee, Y. Hwang, S. Lee, K. Ryoo, S. Ahn, H. Koo, C. Jeong, Y.-T. Kim, G. Koh, G. Jeong, H. Jeong, and K. Kim, "Full integration and Cell Characteristics for

64Mb Nonvolatile PRAM," in *Digest of Technical Papers. 2004 Symposium on VLSI Technology*, p. 20, 2004.

[43] F. Pellizzer, A. Benvenuti, B. Gleixner, Y. Kim, B. Johnson, M. Magistretti, T. Marangon, A. Pirovano, R. Bez, and G. Atwood, "A 90nm Phase Change Memory Technology for Stand-Alone Non-Volatile Memory Applications," in *2006 Symposium on VLSI Technology Digest of Technical Papers*, p. 122, IEEE, 2006.

[44] G. Servalli, "A 45nm generation phase change memory technology," in *2009 International Electron Devices Meeting*, p. 5.7.1, IEEE, 2009.

[45] https://en.wikipedia.org/wiki/3D_XPoint, "3D XPoint," accessed March 19, 2019.

[46] J. Tominaga, a. V. Kolobov, P. Fons, T. Nakano, and S. Murakami, "Ferroelectric Order Control of the Dirac-Semimetal Phase in GeTe-Sb_2Te_3 Superlattices," *Advanced Materials Interfaces*, vol. 1, no. 1, p. 1300027, 2014.

[47] T. Ohyanagi, M. Kitamura, M. Araidai, S. Kato, N. Takaura, and K. Shiraishi, "GeTe sequences in superlattice phase change memories and their electrical characteristics," *Applied Physics Letters*, vol. 104, no. 25, p. 2014, 2014.

[48] X. Yu and J. Robertson, "Modeling of switching mechanism in GeSbTe chalcogenide superlattices," *Scientific Reports*, vol. 5, p. 12612, 2015.

[49] J. Momand, F. R. Lange, R. Wang, J. E. Boschker, M. A. Verheijen, R. Calarco, M. Wuttig, and B. J. Kooi, "Atomic stacking and van-der-Waals bonding in GeTe-Sb_2Te_3 superlattices," *Journal of Materials Research*, vol. 31, no. 20, p. 3115, 2016.

[50] J. Momand, R. Wang, J. E. Boschker, M. A. Verheijen, R. Calarco, and B. J. Kooi, "Interface formation of two- and three-dimensionally bonded materials in the case of GeTe–Sb_2Te_3 superlattices," *Nanoscale*, vol. 7, no. 45, p. 19136, 2015.

[51] B. J. Kooi and J. T. M. De Hosson, "Electron diffraction and high-resolution transmission electron microscopy of the high temperature crystal structures of $Ge_xSb_2Te_{3+x}$ (x=1,2,3) phase change material," *Journal of Applied Physics*, vol. 92, no. 7, p. 3584, 2002.

[52] J. Tominaga, P. Fons, A. Kolobov, T. Shima, T. C. Chong, R. Zhao, H. K. Lee, and L. Shi, "Role of ge switch in phase transition: Approach using atomically controlled GeTe/Sb_2Te_3 superlattice," *Japanese Journal of Applied Physics*, vol. 47, no. 7, p. 5763, 2008.

[53] J. Tominaga, A. V. Kolobov, P. J. Fons, X. Wang, Y. Saito, T. Nakano, M. Hase, S. Murakami, J. Herfort, and Y. Takagaki, "Giant multiferroic effects in topological GeTe-Sb_2Te_3 superlattices," *Science and Technology of Advanced Materials*, vol. 16, no. 1, p. 014402, 2015.

[54] S. Kato, M. Araidaii, K. Kamiya, T. Yamamoto, T. Ohyanagi, N. Takaura, and K. Shiraishi, "Carrier Injection Induced Switching of Supper-lattice GeTe/Sb2Te3 Phase Change Memories," in *2013 International Conference on Solid State Devices and Materials*, p. 544, 2013.

[55] A. C. Jones and M. L. Hitchman, "Overview of Chemical Vapour Deposition," in *Chemical Vapour Deposition: Precursors, Processes and Applications*, ch. 1, p. 1, Royal Society of Chemistry, 2009.

[56] B. E. Deal and A. S. Grove, "General Relationship for the Thermal Oxidation of Silicon," *Journal of Applied Physics*, vol. 36, no. 12, p. 3770, 1965.

[57] W. Wang, J. Denton, and G. W. Neudeck, "Low Temperature Silicon Selective Epitaxial Growth (SEG) and Phosphorous Doping in a Reduced-Pressure Pancake Reactor," tech. rep., 1992.

[58] K. Pu, X. Dai, D. Miao, S. Wu, T. Zhao, and Y. Hao, "A kinetics model for MOCVD deposition of AlN film based on Grove theory," *Journal of Crystal Growth*, vol. 478, p. 42, 2017.

[59] M. R. Leys and H. Veenvliet, "A study of the growth mechanism of epitaxial GaAs as grown by the technique of metal organic vapour phase epitaxy," *Journal of Crystal Growth*, vol. 55, no. 1, p. 145, 1981.

[60] G. B. Stringfellow, "A critical appraisal of growth mechanisms in MOVPE," *Journal of Crystal Growth*, vol. 68, no. 1, p. 111, 1984.

[61] C. H. Chen, H. Liu, D. Steigerwald, W. Imler, C. P. Kuo, M. G. Craford, M. Ludowise, S. Lester, and J. Amano, "A study of parasitic reactions between NH_3 and TMGa or TMAl," *Journal of Electronic Materials*, vol. 25, no. 6, p. 1004, 1996.

[62] R. A. Talalaev, E. V. Yakovlev, S. Y. Karpov, and Y. N. Makarov, "On low temperature kinetic effects in metal-organic vapor phase epitaxy of III-V compounds," *Journal of Crystal Growth*, vol. 230, no. 1-2, p. 232, 2001.

[63] H. Schlichting and K. Gersten, *Boundary-Layer Theory*. Springer, 9th ed., 2017.

[64] T. Fukui and Y. Horikoshi, "Organometallic VPE Growth of $InAs_{1-x}Sb_x$ on InAs," *Japanese Journal of Applied Physics*, vol. 19, no. 1, p. L53, 1980.

[65] P. I. Kuznetsov, B. S. Shchamkhalova, V. O. Yapaskurt, V. D. Shcherbakov, V. A. Luzanov, G. G. Yakushcheva, V. A. Jitov, and V. E. Sizov, "MOVPE deposition of Sb_2Te_3 and other phases of Sb-Te system on sapphire substrate," *Journal of Crystal Growth*, vol. 471, p. 1, 2017.

[66] M. A. Herman, W. Richter, and H. Sitter, *Epitaxy: Physical Principles and Technical Implementation.* Springer, 2004.

[67] H. Emeléus and H. Gunter Jellinek, "The pyrolysis of digermane," *Transactions of the Faraday Society*, vol. 40, p. 93, 1944.

[68] G. Lu and J. E. Crowell, "The adsorption and thermal decomposition of digermane on Ge(111)," *Journal of Chemical Physics*, vol. 98, no. 4, p. 3415, 1993.

[69] N. Bahlawane, F. Reilmann, L. C. Salameh, and K. Kohse-Höinghaus, "Mass-Spectrometric Monitoring of the Thermally Induced Decomposition of Trimethylgallium, Tris(*tert*-Butyl)Gallium, and Triethylantimony at Low Pressure Conditions," *Journal of the American Society for Mass Spectrometry*, vol. 19, no. 7, p. 947, 2008.

[70] https://atct.anl.gov/Thermochemical%20Data/version%201.122d/index.php, "Active Thermochemical Tables," accessed February 20, 2019.

[71] T. McAllister, "Chemical kinetics of telluride pyrolysis," *Journal of Crystal Growth*, vol. 96, no. 3, p. 552, 1989.

[72] H. Dumont, A. Marbeuf, J.-E. Bourée, and O. Gorochov, "Pyrolysis Pathways and Kinetics of Thermal Decomposition of Diethylzinc and Diethyltellurium studied by Mass Spectrometry," *Journal of Materials Chemistry*, vol. 3, no. 10, p. 1075, 1993.

[73] H. Dumont, A. Marbeuf, J. E. Bourée, and O. Gorochov, "Mass-spectrometric Study of Thermal Decomposition of Diethylzinc and Diethyltellurium," *Journal of Materials Chemistry*, vol. 2, no. 9, p. 923, 1992.

[74] M. Czerniak and B. Easton, "An investigation of the pyrolysis of dimethylcadium and diethyltelluride by in-situ gas sampling and analysis," *Journal of Crystal Growth*, vol. 68, no. 1, p. 128, 1984.

[75] D. Toebbens, N. Stuesser, K. Knorr, H. Mayer, and G. Lampert, "E9: The new high-resolution neutron powder diffractometer at the Berlin neutron scattering center," *Materials Science Forum*, vol. 378-381, p. 288, 2001.

[76] N. Yamada, E. Ohno, K. Nishiuchi, N. Akahira, and M. Takao, "Rapid-phase transitions of GeTe-Sb_2Te_3 pseudobinary amorphous thin films for an optical disk memory," *Journal of Applied Physics*, vol. 69, no. 5, p. 2849, 1991.

[77] J. I. Goldstein, *Scanning Electron Microscopy and X-Ray Microanalysis.* 3rd ed., 2003.

[78] L. Reimer and H. Kohl, *Transmission Electron Microscopy - Physics of Image Formation.* Springer-Verlag, 5th ed., 2008.

[79] P. D. Nellist and S. J. Pennycook, "The Principles and Interpretation of Annular Dark-Field Z-Contrast Imaging," *Advances in Imaging and Electron Physics*, vol. 113, p. 147, 2000.

[80] M. T. Otten, "High-Angle Annular Dark-Field Imaging on a TEM/STEM System," *Journal of Electron Microscopy Technique*, vol. 17, no. 2, p. 221, 1991.

[81] A. Amali and P. Rez, "Theory of Lattice Resolution in High-angle Annular Darlzfield Images," *Microscopy and Microanalysis*, vol. 3, no. 1, p. 28, 1997.

[82] H. J. Butt, B. Cappella, and M. Kappl, "Force measurements with the atomic force microscope: Technique, interpretation and applications," *Surface Science Reports*, vol. 59, no. 1-6, p. 1, 2005.

[83] Q. Zhong, D. Inniss, K. Kjoller, and V. B. Elings, "Fractured polymer/silica fiber surface studied by tapping mode atomic force microscopy," *Surface Science Letters*, vol. 290, no. 1-2, p. L688, 1993.

[84] R. Pérez and R. Garcia, "Dynamic atomic force microscopy methods," *Surface Science Reports*, vol. 47, no. 6-8, p. 197, 2002.

[85] C. Suryanarayana and M. Grant Norton, *X-Ray Diffraction. A Practical Approach.* Springer, 1998.

[86] A. Krost, G. Bauer, and J. Woitok, "High Resolution X-Ray Diffraction," in *Optical Characterization of Epitaxial Semiconductor Layers*, ch. 6, p. 287, Springer, 1996.

[87] K. Momma and F. Izumi, "VESTA 3 for three-dimensional visualization of crystal, volumetric and morphology data," *Journal of Applied Crystallography*, vol. 44, no. 6, p. 1272, 2011.

[88] https://fys.kuleuven.be/iks/nvsf/experimental-facilities/x-ray-diffraction-2013-bruker-d8 discover, "X-ray diffraction – Bruker D8 Discover," accessed February 27, 2019.

[89] D. O'Connor, B. Sexton, and R. Smart, *Surface Analysis Methodes in Material Science.* Springer, 2nd ed., 2003.

[90] M. K. Miller and R. G. Forbes, *Atom-Probe Tomography: The Local Electrode Atom Probe.* Springer, 2014.

[91] H. Hardtdegen and P. Giannouls, "MOVPE gets green signal," *III-Vs Review*, vol. 11, no. 5, p. 34, 1998.

[92] M. Longo, O. Salicio, C. Wiemer, R. Fallica, A. Molle, M. Fanciulli, C. Giesen, B. Seitzinger, P. K. Baumann, M. Heuken, and S. Rushworth, "Growth study of

$Ge_xSb_yTe_z$ deposited by MOCVD under nitrogen for non-volatile memory applications," *Journal of Crystal Growth*, vol. 310, no. 23, p. 5053, 2008.

[93] A. Koma, "Van der Waals epitaxy—a new epitaxial growth method for a highly lattice-mismatched system," *Thin Solid Films*, vol. 216, no. 1, p. 72, 1992.

[94] J. Kampmeier, S. Borisova, L. Plucinski, M. Luysberg, G. Mussler, and D. Grützmacher, "Suppressing Twin Domains in Molecular Beam Epitaxy Grown Bi_2Te_3 Topological Insulator Thin Films," *Crystal Growth & Design*, vol. 15, no. 1, p. 390, 2015.

[95] M. Lanius, J. Kampmeier, S. Kölling, G. Mussler, P. M. Koenraad, and D. Grützmacher, "Topography and structure of ultrathin topological insulator Sb_2Te_3 films on Si(111) grown by means of molecular beam epitaxy," *Journal of Crystal Growth*, vol. 453, p. 158, 2016.

[96] J. E. Boschker, J. Momand, V. Bragaglia, R. Wang, K. Perumal, A. Giussani, B. J. Kooi, and H. Riechert, "Surface Reconstruction-Induced Coincidence Lattice Formation Between Two-Dimensionally Bonded Materials and a Three- Dimensionally Bonded Substrate," *Nano Letters*, vol. 14, no. 6, p. 3534, 2014.

[97] J. R. Wiese and L. Muldawer, "Lattice constants of Bi_2Te_3-Bi_2Se_3 solid solution alloys," *Journal of Physics and Chemistry of Solids*, vol. 15, no. 1-2, p. 13, 1960.

[98] A. Giani, A. Boulouz, F. Pascal-Delannoy, A. Foucaran, E. Charles, and A. Boyer, "Growth of Bi_2Te_3 and Sb_2Te_3 thin films by MOCVD," *Materials Science and Engineering B*, vol. 64, no. 1, p. 19, 1999.

[99] G. Bendt, S. Zastrow, K. Nielsch, P. S. Mandal, J. Sánchez-Barriga, O. Rader, and S. Schulz, "Deposition of topological insulator Sb_2Te_3 films by an MOCVD process," *Journal of Materials Chemistry A*, vol. 2, no. 22, p. 8215, 2014.

[100] R. Y. Kim, H. G. Kim, and S. G. Yoon, "Ge film growth in the presence of Sb by metal organic chemical vapor deposition," *Journal of Applied Physics*, vol. 102, no. 8, p. 1, 2007.

[101] S. Higuchi and Y. Nakanishi, "The growth of Ge on a Te/Si(001) surface: surface catalytic epitaxy," *Surface Science Letters*, vol. 254, no. 1-3, p. L465, 1991.

[102] S. Higuchi and Y. Nakanishi, "Growth of Ge on a Te adsorbed Si(001) surface," *Journal of Applied Physics*, vol. 71, no. 9, p. 4277, 1992.

[103] A. Ciesielski, L. Skowronski, W. Pacuski, and T. Szoplik, "Permittivity of Ge, Te and Se thin films in the 200-1500 nm spectral range. Predicting the segregation effects in silver," *Materials Science in Semiconductor Processing*, vol. 81, p. 64, 2018.

[104] A. Smakula and J. Kalnajs, "Precision Determination of Lattice Constants with Geiger-Counter X-Ray Diffractometer," *Physical Review*, vol. 99, no. 6, p. 1737, 1955.

[105] A. S. Cooper, "Precise Lattice Constants of Germanium, Aluminum, Gallium Arsenide, Uranium, Sulphur, Quartz and Sapphire," *Acta Crystallographica*, vol. 15, no. 6, p. 578, 1962.

[106] H. Du, "A nonlinear filtering algorithm for denoising HR(S)TEM micrographs," *Ultramicroscopy*, vol. 151, p. 62, 2015.

[107] http://www.er-c.org/centre/software/gpa.htm, "pga:: geometrical phase analysis software," accessed: June 20, 2018.

[108] M. J. Hÿtch, E. Snoeck, and R. Kilaas, "Quantitative measurement of displacement and strain fields from HREM micrographs," *Ultramicroscopy*, vol. 74, no. 3, p. 131, 1998.

[109] F. J. Blatt, *Physics of Electronic Conduction in Solids*. McGraw-Hill, 1968.

[110] N. P. Breznay, H. Volker, A. Palevski, R. Mazzarello, A. Kapitulnik, and M. Wuttig, "Weak antilocalization and disorder-enhanced electron interactions in annealed films of the phase-change compound $GeSb_2Te_4$," *Physical Review B*, vol. 86, no. 20, p. 205302, 2012.

[111] S. Zastrow, J. Gooth, T. Boehnert, S. Heiderich, W. Toellner, S. Heimann, S. Schulz, and K. Nielsch, "Thermoelectric transport and Hall measurements of low defect Sb_2Te_3 thin films grown by atomic layer deposition," *Semiconductor Science and Technology*, vol. 28, no. 3, p. 035010, 2013.

[112] P. P. Konstantinov, L. E. Shelimova, E. S. Avilov, M. a. Kretova, and V. S. Zemskov, "Thermoelectric Properties of $nGeTe{\cdot}mSb_2Te_3$ Layered Compounds," *Inorganic Materials*, vol. 37, no. 7, p. 662, 2001.

[113] E. M. Conwellt, "Properties of Silicon and Germanium," *Procieedings of the I.R.E.*, vol. 40, no. 11, p. 1327, 1952.

[114] H. Ibach and H. Lüth, *Solid-State Physics. An Introduction to Principles of Materials Science*. Springer, 4th ed., 2009.

[115] L. E. Shelimova, O. G. Karpinskii, P. P. Konstantinov, M. A. Kretova, E. S. Avilov, and V. S. Zemskov, "Composition and Properties of Layered Compounds in the GeTe - Sb_2Te_3 System," *Inorganic Materials*, vol. 37, no. 4, p. 421, 2001.

[116] J. Zhang, C.-Z. Chang, Z. Zhang, J. Wen, X. Feng, K. Li, M. Liu, K. He, L. Wang, X. Chen, Q.-K. Xue, X. Ma, and Y. Wang, "Band structure engineering

in $(Bi_{1-x}Sb_x)_2Te_3$ ternary topological insulators," *Nature communications*, vol. 2, p. 574, 2011.

[117] Y. Jiang, Y. Y. Sun, M. Chen, Y. Wang, Z. Li, C. Song, K. He, L. Wang, X. Chen, Q. K. Xue, X. Ma, and S. B. Zhang, "Fermi-Level Tuning of Epitaxial Sb_2Te_3 Thin Films on Graphene by Regulating Intrinsic Defects and Substrate Transfer Doping," *Physical Review Letters*, vol. 108, no. 6, p. 066809, 2012.

[118] O. Madelung, *Semiconductors: Data Handbook*. Springer, 3rd ed., 2004.

[119] D. Bessas, I. Sergueev, H. C. Wille, J. Perßon, D. Ebling, and R. P. Hermann, "Lattice dynamics in Bi_2Te_3 and Sb_2Te_3: Te and Sb density of phonon states," *Physical Review B*, vol. 86, no. 22, p. 224301, 2012.

[120] N. Peranio, M. Winkler, Z. Aabdin, J. König, H. Böttner, and O. Eibl, "Room temperature MBE deposition of Bi_2Te_3 and Sb_2Te_3 thin films with low charge carrier densities," *Physica Status Solidii A*, vol. 209, no. 2, p. 289, 2012.

[121] J. Kim, S. W. Bedell, S. L. Maurer, R. Loesing, and D. K. Sadana, "Activation of Implanted n-Type Dopants in Ge Over the Active Concentration of 1×10^{20} cm^{-3} Using Coimplantation of Sb and P," *Electrochemical and Solid-State Letters*, vol. 13, no. 1, p. H12, 2009.

[122] V. P. Markevich, I. D. Hawkins, A. R. Peaker, K. V. Emtsev, V. V. Emtsev, V. V. Litvinov, L. I. Murin, and L. Dobaczewski, "Vacancy-group-V-impurity atom pairs in Ge crystals doped with P, As, Sb, and Bi," *Physical Review B*, vol. 70, no. 23, p. 235213, 2004.

[123] V. P. Markevich, A. R. Peaker, V. V. Litvinov, V. V. Emtsev, and L. I. Murin, "Electronic properties of antimony-vacancy complex in Ge crystals," *Journal of Applied Physics*, vol. 95, no. 8, p. 4078, 2004.

[124] D. B. Cuttriss, "Relation Between Surface Concentration and Average Conductivity in Diffused Layers in Germanium," *Bell System Technical Journal*, vol. 40, no. 2, p. 509, 1961.

Acknowledgements

Teamwork and collaboration are great things, which I have had possibility to experience during the time of my doctoral study and research at Peter Grünberg Institute (PGI-9), Research Center Jülich. Here, I would like to acknowledge all people who gave me a hand, supported me, and helped to complete this thesis. Especially:

Prof. Dr. Detlev Grützmacher, without you this thesis would not have existed. You accepted me as a doctoral researcher and believed in me. I am really grateful for our discussions on experimental results and all the time you spent to share your knowledge with me. Thank you for supervising me over this challenging period of my life.

Dr. Hilde Hardtdegen, you introduced me to the world of MOVPE and PCMs. Thank you for your guidance at the beginning of my research and for all valuable discussions we had together.

Dr. Gregor Mussler, you were not my supervisor, but I always could count on your help. Thank you for delivering high-quality XRD data, help with their interpretation and understanding. I am also grateful for your comments on sections 4.1-4.4 of my thesis.

Dr. Martina von der Ahe, you never refused to give me a hand. I will always remember our scientific and non-scientific discussions. Thank you for the effort you put in XRD characterization of the samples. I am also grateful for comments on chapters 1 and 2.

Members of Ernst Ruska-Center, thanks to **Dr. Hongchu Du** for HAADF-STEM measurements and discussions on the results, **Prof. Dr. Rafal Dunin-Borowski** for help with interpretation of HAADF-STEM data, **Doris Meertens, Maximilian Kruth, and Lidia Kibkalo** for preparation of the HAADF-STEM lamellaes by focused ion beam.

Dr. Elmar Neumann and Stephany Bunte, thank you for the introductions and help with operation of SEMs. I am especially grateful for your assistance and time you spent with me to perform EDX analysis of the samples.

Benjamin Bennemann, thank you for the time you spent with me in the lab measuring the Hall effect and for maintaining the AFM setup. Except working, I really enjoyed sharing sport experience with you. Keep going and never give up!

Dr. Alexander Shkurmanov, thank you for delivering XRD data.

Dr. Jürgen Schubert, thank you for RBS characterization of the samples.

Members of ZEA-3, thanks to **Dr. Uwe Breuer** for delivering SIMS data, and **Dr. Ivan Povstugar** for APT analysis of the Ge:Te sample.

Prof. Dr. Thomas Schäpers, thank you for valuable discussions on the results of the Hall effect measurements and your comments on section 4.5.

Prof. Dr. Matthias Wuttig, thank you for discussion on the results of the Hall effect measurements and for your inspiring talks on the topic of PCMs.

Prof. Dr. Hans Lüth, Dr. Nataliya Demarina, and Dr. Christian Weyrich, also for discussions on the electrical characterization of the samples, thank you.

Prof. Dr. Beata Kardynał, you were always ready to discuss with me scientific and non-scientific topics. Thank you for your friendly attitude, advices and support.

Martin Schuck, Thorsten Wierzkowski, and Kristof Keller, you guys introduced me to PGI-9 and showed me how to deal with MOVPE. Thank you for being a team and time we spent on discussions.

Konrad Wirtz, without you, I would not have grown a single sample. Thank you for your assistance and quick solving of all technical problems in the lab.

All cleanroom staff, special thanks to **Janine Worbs** for kind introductions to cleanroom facilities and metallization of the samples, and **Georg Mathey** for his introductions, kindness, and always being ready to help.

Michael Schleenvoigt, thank you for your help in cleanroom, in the final stage of my research.

Silke Piper, Christine Servo, and other office staff of PGI-9, I really appreciate your kindness and support with paper work. Thank you very much.

Johanna Janßen and Abdur Rehman Jalil, it was nice to share the office with you and have possibility to discuss science and other topics. Office mates are always first contact team, as you have been. Thanks for that.

All my friends, who showed interest in my life and kept contact with me, although we were hundreds of kilometers away from each other. Just to name a few: **Mateusz Chmielewski, Emil Dulęba, Andrzej Gawlik, and Michał Waniczek**. Thanks guys!

My sister Alicja and brother Adam, thank you for your support and enjoyable time we had together, which helped me to relax and go through my doctoral study.
Alicjo i Adamie, dzieki za Wasze wsparcie oraz wspólne gry i zabawy, które dostarczły mi chwil relaksu i pomogły przebrnać przez doktorat.

My mom Emilia and dad Adam, a tree needs strong roots to grow. You are my roots and you always support me to grow bigger. Thank you for that.
Mamo i Tato, drzewo, żeby rosnać, potrzebuje silnych korzeni. Moimi korzeniami, które wspierają mój rozwój, jesteście Wy. Dziękuję Wam za to.

My fiancee Sanja Novak, you are the last but not the least, and I hope you know it. You shared with me all my ups and downs over the time of my doctoral research, never turning your back on me. Thank you for being next to me, all your help and support.

List of Publications

- A. Ratajczak, M. v.d. Ahe, H. Du, G. Mussler, D. Grützmacher, *Metal organic vapor phase epitaxy of $Ge_1Sb_2Te_4$ thin films on Si(111) substrate*, Applied Physics A 125 (2019), 163
- A. Ratajczak, *Laser azotowy*, Foton 103 (2008), 52

List of Presentations

- *Coalesced $Ge_1Sb_2Te_4$ thin films grown by MOVPE*, SFB Retreat 2016, 02-03.03.2018, Spa, Belgium – poster presentation
- *Twin domains suppression in MOVPE grown $Ge_1Sb_2Te_4$ thin films*, DGKK-Workshop 2017, 06-07.12.2017, Freiburg, Germany – oral presentation
- *Characteristics of epitaxial trigonal $Ge_1Sb_2Te_4$ (0001)*, E\PCOS 2017 - European Phase Change and Ovonics Symposium 2017, 04-05.09-2017, Aachen, Germany – poster presentation
- *Investigation of MOVPE grown $Ge_1Sb_2Te_4$ thin films*, EW-MOVPE 17 – The 17th European Workshop on Metal-Organic Vapour Phase Epitaxy, 18-21.06.2017, Grenoble, France – poster presentation, *Best Poster Award*
- *Growth evolution of Ge-Sb-Te thin films in metal organic vapor phase epitaxy*, DGKK-Workshop 2016, 08-09.12.2016, Düsseldorf, Germany – oral presentation
- *MOVPE of $Ge_1Sb_2Te_4$: a model material for energy-saving non-volatile memories*, JARA-FIT Science Days 2016, 11-12.11.2016, Schleiden, Germany – poster presentation
- *MOVPE growth process and characterization of coalesced Ge-Sb-Te thin films*, SFB 917 Retreat 2016, 27-28.10.2016, Spa, Belgium – poster presentation
- *Optimization of molecular beam epitaxy growth conditions for InSb based mid-wavelength infrared detectors*, PHOTONICA 2015 – V International School and Conference on Photonics, 24-28.08.2015, Belgrade, Serbia – poster presentation
- *Optimization of MBE growth of InSb on semi-insulating GaAs substrate for mid-wavelength infrared detectors*, SMMO2015 – International Conference on Semiconductor Mid-IR Materials and Optics, 08-11.04.2014, Prague, Czech Republic – poster presentation
- *Etching techniques for site-controlled InP/GaInP quantum dots grown on patterned substrates*, 12^{th} Students' Science Conference, 18-21.09.2014, Boguszów-Gorce, Poland – oral presentation, *Best Presentation Award*